# Ultrafast population transfer and ionization mechanisms in intense laser fields

Olofsson, Edvin

2024

*Document Version:*
Publisher's PDF, also known as Version of record

# Ultrafast population transfer and ionization mechanisms in intense laser fields

EDVIN OLOFSSON
DEPARTMENT OF PHYSICS | FACULTY OF ENGINEERING | LUND UNIVERSITY

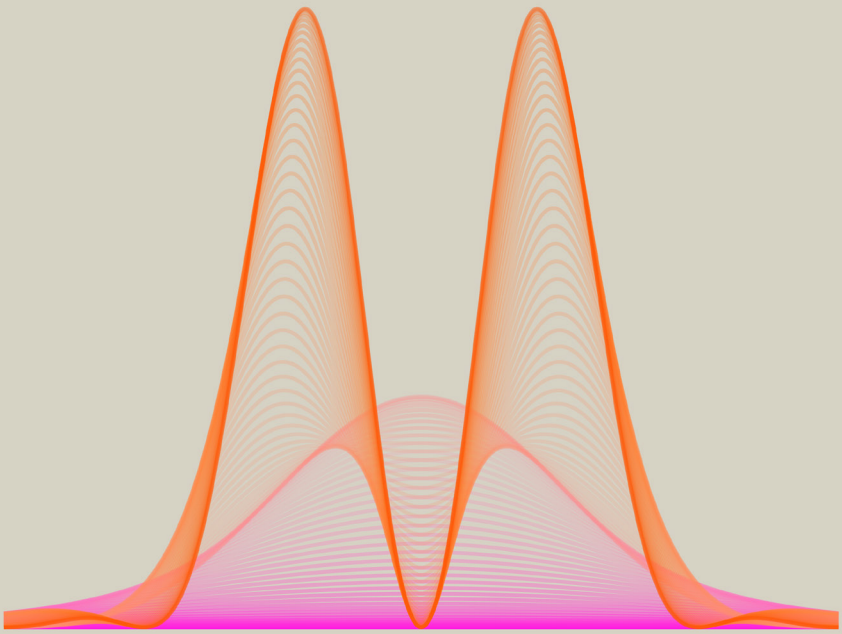

# Ultrafast population transfer and ionization mechanisms in intense laser fields

# Ultrafast population transfer and ionization mechanisms in intense laser fields

by Edvin Olofsson


LUND
UNIVERSITY

Thesis for the degree of Doctor of Philosophy in Physics
Thesis advisors: Assoc. Prof. Jan Marcus Dahlström,
Assoc. Prof. Claudio Verdozzi, Prof. Peter Samuelsson
Faculty opponent: Prof. Uwe Thumm

To be presented, with the permission of the Faculty of Engineering of Lund University, for public criticism in the Rydberg lecture hall (Rydbergsalen) at the Department of Physics on Wednesday, the 12th of June 2024 at 09:15.

Organization
**LUND UNIVERSITY**

Department of Physics
Box 118
SE–221 00 LUND
Sweden

Document name
**DOCTORAL DISSERTATION**

Date of disputation
2024-06-12

Sponsoring organization

Author(s)
Edvin Olofsson

Title and subtitle
Ultrafast population transfer and ionization mechanisms in intense laser fields

Abstract
This thesis adresses different aspects of atoms interacting with strong laser fields. The focus is on population and ionization dynamics occurring on ultrafast timescales, when atoms are subjected to intense extreme ultraviolet or infrared laser light. Different ways of modeling these interactions are considered. Comparisons to experimental results are performed in certain cases, and in other cases predictions are made for future experiments.

This thesis comprises five papers.

In paper I, we investigate resonant photoionization of helium atoms through an experiment performed using a free-electron laser, and through numerical simulations and a model based on Rabi oscillations.

In paper II, we consider another photoionization experiment performed using a free-electron laser, where the photon energy is resonant with a transition in the ion. The entanglement between the ion and photoelectron is studied with a model and with numerical simulations.

In paper III, resonant ionization is studied using the effective Hamiltonian formalism, and a prediction is made about stabilization of dressed states.

In paper IV, the RABBIT technique applied to an atom undergoing Rabi oscillations is studied theoretically, through numerical simulations and perturbative calculations.

In paper V, a model for frustrated tunneling ionization, based on the strong-field approximation is studied in detail, and compared with results from numerically solving the time-dependent Schrödinger equation.

Key words
Resonant photoionization, Rabi oscillations, free-electron laser, stabilization, ultrafast dynamics, strong field approximation, frustrated tunneling ionization

Classification system and/or index terms (if any)

Supplementary bibliographical information

Language
English

ISSN and key title

ISBN
978-91-8104-058-6 (print)
978-91-8104-059-3 (pdf)

Recipient's notes

Number of pages
225

Price

Security classification

# Ultrafast population transfer and ionization mechanisms in intense laser fields

by Edvin Olofsson


LUND
UNIVERSITY

A doctoral thesis at a university in Sweden takes either the form of a single, cohesive research study (monograph) or a summary of research papers (compilation thesis), which the doctoral student has written alone or together with one or several other author(s).

In the latter case the thesis consists of two parts. An introductory text puts the research work into context and summarizes the main points of the papers. Then, the research publications themselves are reproduced, together with a description of the individual contributions of the authors. The research papers may either have been already published or are manuscripts at various stages (in press, submitted, or in draft).

**Cover illustration front:** Formation of an Autler-Townes doublet as the pulse duration increases from 0 to 2 Rabi periods.

**Cover illustration back:** Sunset over Larsmosjön.

**Funding information:** The thesis work was financially supported by the Olle Engkvist Foundation, Grant No. 194-0734.



Faculty of Engineering, Department of Physics

ISBN: 978-91-8104-058-6 (print)
ISBN: 978-91-8104-059-3 (pdf)

Printed in Sweden by Media-Tryck, Lund University, Lund 2024

Media-Tryck is a Nordic Swan Ecolabel certified provider of printed material. Read more about our environmental work at www.mediatryck.lu.se

MADE IN SWEDEN

*Dedicated to my family*

# Contents

## List of publications

This thesis is based on the following publications, referred to by their Roman numerals:

I **Observation of Rabi dynamics with a short-wavelength free-electron laser**

S. Nandi, **E. Olofsson**, M. Bertolino, S. Carlström, F. Zapata, D. Busto, C. Callegari, M. Di Fraia, P. Eng-Johnsson, R. Feifel, G. Gallician, M. Gisselbrecht, S. Maclot, L. Neoričić, J. Peschel, O. Plekan, K. C. Prince, R. J. Squibb, S. Zhong, P. V. Demekhin, M. Meyer, C. Miron, L. Badano, M. B. Danailov, L. Giannessi, M. Manfredda, F. Sottocorona, M. Zangrando, J. M. Dahlström
Nature **608**, pp. 488–493 (2022)

II **Generation of entanglement using a short-wavelength seeded free-electron laser**

S. Nandi, A. Stenquist, A. Papoulia, **E. Olofsson**, L. Badano, M. Bertolino, D. Busto, C. Callegari, S. Carlström, M. B. Danailov, P. V. Demekhin, M. Di Fraia, P. Eng-Johnsson, R. Feifel, G. Gallician, L. Giannessi, M. Gisselbrecht, M. Manfredda, M. Meyer, C. Miron, J. Peschel, O. Plekan, K. C. Prince, R. J. Squibb, M. Zangrando, F. Zapata, S. Zhong, J. M. Dahlström
Sci. Adv. **10**, pp. eado0668 (2024)

III **Photoelectron signature of dressed atom stabilization in an intense XUV-field**

**E. Olofsson**, J. M. Dahlström
Phys. Rev. Res. **5**, pp. 043017 (2023)

IV **Circularly polarized RABBIT applied to a Rabi-cycling atom**

Y. Liao, **E. Olofsson**, J. M. Dahlström, L.-W. Pi., Y. Zhao, P. Lu
Phys. Rev. A **109**, pp. 043104 (2024)

V **Frustrated tunneling dynamics in ultra-short laser pulses**

**E. Olofsson**, S. Carlström, J. M. Dahlström
J. Phys. B: At. Mol. Opt. Phys. **54**, pp. 154002 (2021)

# Acknowledgements

I would first like to thank my supervisor Marcus for your great support during my years as a PhD student. When I started this journey I knew very little about atoms interacting with lasers, but with your guidance I have learned so much during these years. Your enthusiasm for physics is truly remarkable, and I have enjoyed the many discussions we have had in our meetings. I will always be grateful for the kindness and understanding that you showed me, and for helping me get back on track when I was in a very bad spot. I also want to thank my co-supervisors Claudio and Peter for their support and encouragement.

A huge thank you to everyone who has been part of the Theoretical Light–Matter Dynamics group: Mattias, Felipe, Stefanos, Asimina, Rezvan, Axel, Yijie, Jimmy and Jakob. It has been so nice to get to know each of you during these years. I will never forget all the good times we have shared together at the office and on conferences. I also appreciate all the physics discussions we have had in group meetings, in Sadelpunktsklubben, and on Discourse.

I want to thank everyone who was involved in the experiments at FERMI and in the resulting papers. I am especially grateful to Saikat for introducing us to these topics, for all your hard work on interpreting the data, and for your role in the writing process. These projects completely changed the trajectory of my PhD, and I am so happy it turned out this way.

A big thank you to thank all of my office mates during my years at Mathematical Physics: Zhen, Gunnar, Erik, Saulo, Armin, Nicola, and Carles. Thank you all for providing some much needed humor and light-hearted moments during the working day. I also want to thank everyone else at Mathematical Physics for creating such a nice environment, and for all the lunch breaks and Friday fikas. A special thank you to Cecilia for your interesting stories, and for your thoughtful questions about how things are going.

I want to thank Erik, Viktor, and Ismail for your friendship during my time in Lund. I also want to thank Klas for fysikprogrammet, which brought me to Lund in the first place, and Ulla for providing me with a place to live during my high school years. I am grateful for all the people in Lunds Schackklubb and Team Nordic Trail Lund for providing meaningful distractions from work, and for always making me feel welcome. I am also grateful for the help I received with my mental health from the team at Vårdcentralen Linero.

I will end this section with some words in Swedish for my family. Till mina föräldrar Bodil och Bo, och mina systrar Elin och Therése: Tack för all er kärlek och det stöd som ni har gett mig. Till mina systerdöttrar Ebba, Saga, och Svea: Det är så spännande att få se er växa upp, och jag uppskattar varenda stund som jag får spendera med er. Till mina far- och morföräldrar: Ni har betytt så mycket för mig, och jag är så ledsen att jag inte får dela den här dagen med er. Till hela min finlandssvenska släkt: Tack för alla fina minnen från

somrarna i Österbotten.

## Popular summary

Most of us have come into contact with laser light at some point in our lives. Perhaps you have used a laser pointer during a presentation, seen laser weapons in a sci-fi movie, or maybe you have had laser eye surgery. But you are probably less familiar with the type of intense lasers and light-sources that are used at the forefront of research on light–matter interaction, and the effects that can be studied with them.

In quantum mechanics, light can be seen both as consisting of a kind particle and as electromagnetic waves. What determines how light and matter interact is on the one hand its *intensity*, and on the other hand its *frequency*. In the wave picture, intensity is related to the size of the oscillations in the electromagnetic field, and the frequency determines how fast the oscillations are. In the particle picture, the intensity roughly corresponds to how many particles of light, *photons*, are within certain volume, while the frequency determines how much energy an individual photon has.

In the particle picture, atoms interact with light by absorbing or emitting photons, while simultaneously transitioning between energy levels. If the light has a high intensity, then there will be many photons in the vicinity of the atom, and the probability for the atom to absorb a photon is increased. In some cases there are so many photons near the atom that it can absorb more than one photon, it performs a multiphoton transition. The atom can then be found in energy levels that are not accessible through the absorption of only one photon.

**Rabi oscillations with extreme UV light**

When the photon energy of a laser matches the energy difference between two energy levels in an atom, the atom can absorb one photon to reach the upper level. Since the absorption happens randomly, there will be a certain probability of finding the atom in the upper level. This probability increases as time goes on, until the atom is in the upper level with close to 100 % probability. When the atom is in the upper level, it can return a photon to the laser light through a process called *stimulated emission*. This will cause the probability of finding the atom in the excited state to decrease, until the atom is most likely to be found in the ground state again. If the atom is still illuminated by the laser, this process can be repeated many times. The oscillations in the probability of finding the atom in the lower or upper level are known as *Rabi oscillations*.

If the light that is driving the Rabi oscillations is very intense, the frequency of the oscillations will increase. It also becomes more likely that the atom will absorb an extra photon. For helium atoms, this would mean that one of its electrons gets enough energy to break free from the nucleus, leaving an ion behind. If one measures the energy of the freed electron, one would typically expect to see a peak at *one* specific energy, that is determined by

the photon energy and the ionization energy of the atom (how much energy is required to remove the electron). However, if the atom is undergoing Rabi oscillations one sees *two* peaks, one on either side of the expected position. This phenomenon is often referred to as an Autler-Townes doublet, after the scientists that discovered this kind of doublet in a related process.

Generating Rabi oscillations in a helium atom requires high intensity and high frequency. The frequencies involved lie in the part of the electromagnetic spectrum that is referred to as extreme ultraviolet (XUV), which means that the frequency is higher than typical UV light. It is difficult to achieve both high intensity and high frequency in a lab, but it can be done with a *free-electron laser* (FEL). In an FEL, electrons are accelerated by a particle accelerator to close to the speed of light. They then pass through a magnetic field where the direction of north and south is alternating, causing them to wiggle. The relativistic wiggling motion leads to emission of high frequency light in the direction of propagation.

**Electrons tunneling to freedom?**

In an atom the electrons are bound to the nucleus through the Coulomb force, which creates a potential well that traps the electrons. If the atom interacts with very intense laser light that has a low frequency, the potential well becomes so distorted by the lights electric field that the electrons can escape the well through *quantum tunneling*. If an electron has tunneled, there are several possibilities for what can happen next.

Some electrons will return to the atom when the electric field starts to point in the opposite direction. They can then ”jump” back into the potential well, by emitting a photon. Since the electrons can have a very high energy when they return, some of the emitted photons will have a much higher frequency than that of the laser light that drives the process. This process, which was discovered in 1987, is called *high harmonic generation*, and was one of the discoveries that was behind the 2023 Nobel prize in physics.

Other electrons will simply continue to travel away from the atom, never to return. This process is called *tunneling ionization*, since the electrons have tunneled their way free from the atom. In 2008, an experiment by Nubbemeyer et al. shed light on another possibility. After the electron has tunneled it can end up in an orbit further away from the nucleus, instead of leaving completely. The atom would then be in an excited state. This process is sometimes referred to as *frustrated* tunneling ionization, since some electrons that tunnel remain in the atom. The electrons that undergo this process are heavily influenced by both the laser light and the Coulomb force, and it is therefore very difficult to describe their motion using analytical calculations.

Within the scope of this thesis, I have modeled both present and possible future experiments where Rabi oscillations and Autler-Townes doublets are present, and studied what the doublet can say about the processes that occur in the atom. I have also studied a pro-

posed model for frustrated tunneling ionization, and explored its validity.

# Populärvetenskaplig sammanfattning

De flesta av oss har kommit i kontakt med laserljus någon gång i livet. Kanske har du använt en laserpekare under en presentation, sett laservapen i en sci-fi-film, eller så har du kanske fått ögonen opererade med hjälp av laserljus. Men antagligen så har du lite mindre koll på den typ av starka lasrar och ljuskällor som används i framkanten av dagens forskning på hur ljus och materia samverkar, och vilka effekter som kan studeras med hjälp av dem.

Inom kvantmekaniken så kan ljus ses både som partiklar och som elektromagnetiska vågor. Det som bestämmer hur ljus och materia växelverkar är dels ljusets *intensitet*, men också dess *frekvens*. I vågbilden så är intensiteten relaterad till storleken på svängningarna på det elektromagnetiska fältet, och frekvensen bestämmer hur snabbt fältet svänger. I partikelbilden så bestämmer intensiteten hur många ljuspartiklar, *fotoner*, som kan finnas inom en viss volym, medan frekvensen bestämmer hur mycket energi en enskild foton har.

I partikelbilden växelverkar atomer med ljus genom att absorbera eller sända ut fotoner, samtidigt som atomen gör övergångar mellan energinivåer. Om ljuset har hög intensitet betyder det att det finns väldigt många fotoner i närheten av atomen som den kan absorbera, och sannolikheten för att den ska göra just det ökar. I vissa fall finns det så många fotoner att atomen kan absorbera fler än en foton, vilket brukar benämnas som en *multifotonövergång*. Atomen kan då hittas i energitillstånd som inte är tillgängliga med absorption av endast en foton.

**Rabi-oscillationer med extremt UV-ljus**

När energin hos fotonerna stämmer överens med skillnaden mellan två energitillstånd i en atom, så kan atomen absorbera en foton och göra en övergång mellan energitillstånden. Eftersom detta sker slumpmässigt, så kommer det finnas en viss sannolikhet för att hitta atomen i det övre tillståndet. Då atomen utsätts för laserljus kommer sannolikheten att öka med tiden, fram tills det att atomen hittas i det övre tillståndet med nästan 100 % sannolikhet. När atomen är i det övre tillståndet så kan den ge tillbaka en foton till laserljuset i en process som kallas *stimulerad emission*. Detta gör att sannolikheten att atomen ska hittas i det övre tillståndet börjar minska, tills atomen med stor sannolikhet hittas i det lägre tillståndet igen. Denna process kan upprepas många gånger, och svängningarna i sannolikheten kallas för *Rabi-oscillationer*.

Om ljuset som driver de här Rabi-oscillationerna är väldigt starkt så kan atomen oscillera fort, men atomen kan också absorbera två fotoner, istället för endast en. För heliumatomer innebär detta att en av dess elektroner får tillräckligt med energi för att bryta sig loss från kärnan, vilket innebär att atomen har joniserats. Det är sedan möjligt att mäta energin på den nu fria elektronen. Om atomen inte Rabi-oscillerar förväntar man sig att hitta elektroner vid *en* specifik energi, som bestäms av fotonenergin och elektronens bindningsenergi

(hur mycket energi det krävs för att jonisera atomen). Men istället ser man *två* toppar, en på varsin sida om den förväntade energin. Detta fenomen kallas ofta för en Autler-Townes dubblett, efter de forskare som upptäckte denna typ av dublett i ett lite annat, men relaterat, sammanhang.

För att det ska uppstå Rabi-oscillationer i en heliumatom så krävs det både hög intensitet och hög frekvens. De frekvenser som krävs ligger i det spann som kallas för *extremt ultraviolett ljus*. Detta är inte lätt att åstadkomma i ett labb, men det kan göras med hjälp av en *frielektronlaser*. I en frielektronlaser så accelereras elektroner i en partikelaccelerator till nära ljusets hastighet. Dessa elektroner får sedan svänga från sida till sida i ett magnetfält, vilket leder till att de sänder ut ljus med hög frekvens.

**Elektroner tunnlar till frihet?**

I en atom så hålls elektronerna bundna till atomkärnan på grund av Coulombkraften, som skapar en potentialbrunn som elektronerna sitter fast i. Om atomen växelverkar med ljus som har mycket hög intensitet men låg frekvens, så påverkas den här potentialbrunnen så starkt av ljusets elektriska fält att den blir förvrängd, och elektronerna kan läcka ut ur brunnen på grund av *tunneleffekten*. Det finns flera möjligheter för vad som kan hända med de frisläppta elektronerna.

En del elektroner kommer tillbaka till atomen när ljusets elektriska fält börjar peka åt motsatt håll i sin svängning. De kan då hoppa ner i potenialbrunnen igen, genom att sända ut en foton. Elektronen kan ha väldigt hög energi när den kommer tillbaka, så en del av de fotoner som sänds ut kommer ha mycket högre energi än de ursprungliga fotonerna från lasern. Denna process, som upptäcktes år 1987, kallas för *övertonsgenerering*, och var en av upptäckterna som låg bakom 2023 års Nobelpris i fysik.

Andra elektroner kommer istället att fortsätta bort från atomen utan att någonsin komma tillbaka. Detta fall kallas för *tunneljonisation*, eftersom att elektronerna har tunnlat sig fria från atomen. År 2008 så uppmärksammade ett experiment från Nubbemeyer et al. en annan möjlighet. Efter att elektronen har tunnlat så kan den hamna i en bana en bit iväg från atomkärnan, istället för att försvinna bort helt från atomen eller hoppa hela vägen ner i brunnen. Det här innebär att atomen är i ett exciterat tillstånd. Denna process brukar kallas för *frustrerad* tunneljonisation, eftersom en del av de elektroner som tunnlat inte lämnar atomen helt. Dessa elektroner påverkas mycket starkt av både laserljuset och Coulombkraften från kärnan, och det är därför inte så enkelt att beskriva hur deras banor ser ut med analytiska beräkningar.

Inom ramen för den här avhandlingen så har jag modellerat experiment som har utförts, eller möjligtvis kan utföras, där man kan se en Autler-Townes dubblett, och studerat vad den kan säga om processerna som pågår i atomen. Jag har även studerat en modell som lagts fram för frustrerad tunneljonisation, och undersökt dess giltighet.

# List of abbreviations

| | |
|---|---|
| **AT** | Autler-Townes |
| **ATI** | Above-threshold ionization |
| **ATP** | Attosecond pulse train |
| **CAP** | Complex absorbing potential |
| **CEP** | Carrier–envelope phase |
| **CIS** | Configuration interaction singles |
| **ECS** | Exterior complex scaling |
| **FEL** | Free-electron laser |
| **FERMI** | Free-Electron laser Radiation for Multidisciplinary Investigations |
| **FTI** | Frustrated tunneling ionization |
| **FWHM** | Full width at half maximum |
| **GE** | Grobe-Eberly |
| **GMRES** | Generalized minimal residual method |
| **HF** | Hartree-Fock |
| **HHG** | High-order harmonic generation |
| **IR** | Infrared |
| **RABBIT** | Reconstruction of Attosecond Beating By Interference of Two-photon transitions |
| **RWA** | Rotating wave approximation |
| **SFA** | Strong-field approximation |
| **TDCIS** | Time-dependent configuration interaction singles |
| **TDSE** | Time-dependent Schrödinger equation |
| **XUV** | Extreme ultraviolet |

# Introduction

## 1 Introduction

This thesis concerns the dynamics of atoms interacting with light, and some processes that can occur when this interaction is strong. Specifically the focus will be on processes where the bound states of the atom play an important role, such as resonant photoionization and core-resonant photoionization, and excited state population dynamics. The dynamics that are studied take place on an ultrafast timescale, on the order of a few to tens of fs.

### 1.1 Free-electron lasers in the extreme ultraviolet and X-ray regimes

The works included in the thesis are partly motivated by the capabilities of extreme ultraviolet (XUV) and X-ray free-electron laser (FEL) technology, which have seen major breakthroughs in the last decades [1–5]. The combination of high intensity and high photon energies that are made available by XUV and X-ray FELs open up previously unexplored regions of parameter space to experiments. Examples include XUV-driven Rabi dynamics in He atoms, which are explored in papers I and II. Recently it has become possible to produce attosecond pulse trains [6, 7] and isolated attosecond pulses [8, 9] with FELs, enabling FEL experiments with intense attosecond pulses. At the FEL FERMI [2], control of the spectral phase of the FEL pulses has also been demonstrated [10], which opens up additional possibilities for quantum control with intense XUV pulses.

In the case of strongly driven resonant photoionization, much of the theoretical foundations were laid already several decades ago [11–14], however the opportunity to study it in the XUV regime has become possible only through the use of FELs, see paper I and Ref. [10], which might explain why the topic has received renewed attention in recent years [15–18]. In Ref. [11], Beers and Armstrong suggested a mechanism for stabilization of dressed states in resonant photoionization that was studied in paper III, where a prediction was made that the effect could be studied at a seeded FEL, such as FERMI, in the realistic case of helium atoms.

## 1.2 Strong low-frequency fields and attosecond physics

In addition to the intensity, another quantity that can be used to characterize the strength of the light–matter interaction is the ponderomotive energy

$$U_p = \frac{e^2 E_0^2}{4 m_e \omega^2}, \tag{1}$$

where $\omega$ is the frequency of light,$E_0$ is the electric field amplitude, $m_e$ is the electron mass, and $e$ the elementary charge. $U_p$ represents the kinetic energy of a free electron interacting with the light, averaged over one oscillation period of the field. Since $\omega$ appears in the denominator, it is easier to achieve large values of $U_p$ with infrared (IR) light sources, rather than XUV or X-ray sources. In particular, in experiments with IR sources $U_p$ is often comparable or larger than the photon energy of the IR field.

Strong IR fields were used in the discovery of high-order harmonic generation (HHG) [19], which laid the foundation of the field of attosecond science that was awarded the 2023 Nobel Prize in physics [20]. The location of the cutoff frequency in the high-harmonic spectrum depends on $U_p$ [21]. For this regime of light–matter interaction an often employed approach is the strong-field approximation (SFA). It provides an intuitive picture for both above-threshold ionization (ATI) [22–24] and HHG [25, 26], based on field induced tunneling followed by subsequent propagation in the electric field. Paper v studies a SFA based model proposed by Popruzhenko [27] for frustrated tunneling ionization (FTI), which is another phenomenon that occurs in experiments with intense low-frequency fields [28].

One of the methods that was used to show the existence of attosecond pulses (specifically attosecond pulse trains) is the reconstruction of attosecond beating by interference of two-photon transitions (RABBIT) technique [29–31]. In addition to being used as tool to measure attosecond pulse trains, RABBIT can also be used to study dynamical aspects of the photoionization process [32]. This was explored in paper iv, where the protocol was employed to study a Rabi-cycling atom.

## 1.3 Structure of this work

The outline of this thesis is as follows. In the next part, *Background*, a review of the topics that were considered in the thesis is provided. Section 2 provides a brief overview of the description of light–matter interactions. This is followed by a description of the specific techniques that were used in the publications. Section 3 shows how resonant ionization of atoms can be treated with perturbation theory on top of Rabi oscillations, which is relevant for papers i, ii and iv. The effective Hamiltonian method, which is utilized in paper iii, is introduced in Sec. 4. The last section of this part introduces the SFA, and a model for FTI that is based on it, in Sec. 5. This SFA-FTI model was studied in paper v.

The following part, *Summary of results and applications*, provides a summary of the results that were obtained in the publications included in the thesis, as well as indicating some further results that were not covered in the publications, and some possible future directions of inquiry. Section 6.1 presents the results of papers I and II, that both deal with resonant photoionization experiments performed at the FERMI FEL. The next section, Sec. 6.2, presents a prediction of stabilization of dressed states in resonant photoionization, based on the effective Hamiltonian model introduced in paper III. The framework of perturbation theory on top of Rabi oscillations is applied to a RABBIT scheme in paper IV, and this is discussed in Sec. 7. The results of paper V, that studies a model for FTI, are summarized in Sec. 8. This is followed by a summary of the thesis together with some future perspectives in *Summary and outlook*. Papers I-V are then reprinted in their entirety, preceded by a summary of the author's contributions, in the final part of the thesis, *Scientific publications*.

# Background

## 2 Describing light–matter interaction

This section will cover the basics of light–matter interaction that will be required in the later sections. Atomic units

$$\hbar = m_{\mathrm{e}} = 4\pi\epsilon_0 = e = 1, \tag{2}$$

will be used in the remainder of the thesis, unless otherwise noted, where $\hbar$ is the reduced Planck constant, $m_{\mathrm{e}}$ is the electron mass, $\epsilon_0$ is the vacuum permittivity, and $e$ the elementary charge.

### 2.1 TDSE in the dipole approximation

The time-dependent Schrödinger equation (TDSE), is used to describe the time-evolution of a quantum state $|\psi(t)\rangle$

$$i\frac{\mathrm{d}}{\mathrm{d}t}|\psi(t)\rangle = H(t)|\psi(t)\rangle\,, \tag{3}$$

where $H(t)$ is the Hamiltonian operator that generates the dynamics of the system. It can also be formulated in terms of the time-evolution operator

$$i\frac{\mathrm{d}}{\mathrm{d}t}U(t,t_0) = H(t)U(t,t_0), \tag{4}$$

where $U(t,t_0)$ is the operator that propagates the state forward in time

$$U(t,t_0)|\psi(t_0)\rangle = |\psi(t)\rangle\,, \tag{5}$$

and $t > t_0$.

The minimal coupling Hamiltonian for an atomic electron interacting with an external electromagnetic field is given by [33]

$$H(t) = \frac{[\mathbf{p} + \mathbf{A}(\mathbf{r},t)]^2}{2} + V(r), \tag{6}$$

where $\mathbf{p}$ is the momentum operator, $\mathbf{A}(\mathbf{r},t)$ is the vector potential in the Coulomb gauge $\nabla \cdot \mathbf{A}(\mathbf{r},t) = 0$, and $V(r)$ represents the interaction with the atomic nucleus (possibly screened by other electrons).

**Dipole approximation and gauge transformations**

For a plane-wave electromagnetic field the vector potential can be written as

$$\mathbf{A}(\mathbf{r},t) = \mathbf{A}_0 \sin(\omega t - \mathbf{k}\cdot\mathbf{r} + \varphi) = \frac{\mathbf{A_0}}{2}\left[e^{i(\omega t - \mathbf{k}\cdot\mathbf{r}+\varphi)} - e^{-i(\omega t - \mathbf{k}\cdot\mathbf{r}+\varphi)}\right]. \quad (7)$$

If the field is slowly varying on the length-scales we are interested in ($r \ll \lambda = 2\pi/|\mathbf{k}|$), then we can make the dipole approximation [33]

$$e^{i\mathbf{k}\cdot\mathbf{r}} = 1 + i\mathbf{k}\cdot\mathbf{r} + \ldots \approx 1, \quad (8)$$

neglecting the spatial dependence of the vector potential. This amounts to neglecting the magnetic component of the EM field, and any spatial variations of the electric component. In the dipole approximation, the relation between the vector potential and the electric field is

$$\mathbf{E}(t) = -\frac{\mathrm{d}\mathbf{A}(t)}{\mathrm{d}t}. \quad (9)$$

The resulting Hamiltonian then has the following form,

$$H(t) = \frac{[\mathbf{p} + \mathbf{A}(t)]^2}{2} + V(r), \quad (10)$$

which is called the velocity gauge form of the Hamiltonian. The $\mathbf{A}(t)^2$ term in the above Hamiltonian can be removed by a gauge transformation

$$T = e^{i\int^t \mathrm{d}t' \mathbf{A}(t')^2}, \quad (11)$$

which gives the reduced velocity gauge Hamiltonian,

$$H(t) = \frac{\mathbf{p}^2}{2} + \mathbf{p}\cdot\mathbf{A}(t) + V(r). \quad (12)$$

The length gauge form of the interaction Hamiltonian can be arrived at by applying the gauge transformation

$$T = e^{i\mathbf{A}(t)\cdot\mathbf{r}}, \quad (13)$$

to the Hamiltonian in Eq. (10). The resulting Hamiltonian is

$$H(t) = \frac{\mathbf{p}^2}{2} + V(r) + \mathbf{E}(t)\cdot\mathbf{r}. \quad (14)$$

The velocity and length forms are the ones typically used in calculations. In principle physical quantities should be gauge invariant, but in practice gauge invariance is often broken when employing certain approximation schemes, for instance truncating the Hilbert space [34–36]. State populations and the expectation value of the Hamiltonian are quantities that are not invariant when the fields are non-zero, but the result at the end of a pulse should agree between gauges (assuming convergence in the size of the considered Hilbert space etc).

### Field envelopes

Interaction with pulsed lasers can be simulated by introducing an envelope $f(t)$ to the amplitude of the vector potential

$$\mathbf{A}(t) = \mathbf{A}_0 f(t) \sin(\omega t + \varphi). \tag{15}$$

The electric field is then given by

$$\mathbf{E}(t) = -\omega \mathbf{A}_0 f(t) \cos(\omega t + \varphi) - \mathbf{A}_0 \frac{\mathrm{d}f}{\mathrm{d}t} \sin(\omega t + \varphi). \tag{16}$$

In the slowly varying envelope approximation the second term is neglected, which is valid when envelope is changing slowly between laser cycles ($\omega \gg \frac{\mathrm{d}f}{\mathrm{d}t}$). Then one also has the following relation between the amplitude of the vector potential and the amplitude $E_0$ of the electric field

$$A_0 \approx -\frac{E_0}{\omega}. \tag{17}$$

A very useful relation, is the conversion between electric field strength in atomic units and intensity in W/cm$^2$. Atomic units is convenient for calculations, while intensity is often reported in W/cm$^2$. The conversion is given by

$$I \text{ [W/cm}^2\text{]} = 3.51 \times 10^{16} \times E_0^2 \text{ [a.u.]} . \tag{18}$$

### Polarization and the Wigner-Eckart theorem

In this thesis two kinds of polarization of light will be considered, linear and circular. In order to simplify calculations of matrix elements, calculations with linear polarization will be performed with the polarization along the $z$-axis, while for calculations with circular polarization, the plane of polarization will be taken to be the $x$-$y$-plane. This means that in the length gauge, with a monochromatic electric field, the interaction term will be

$$\mathbf{E}(t) \cdot \mathbf{r} = E_0 \cos(\omega t) z = \frac{E_0 z}{2} \left( e^{i\omega t} + e^{-i\omega t} \right), \tag{19}$$

for linearly polarized light. In the case of circular polarization we will instead have

$$\frac{E_0}{\sqrt{2}}\left[\mathbf{e}_x\cos(\omega t)+\mathbf{e}_y\sin(\omega t)\right]\cdot\mathbf{r}=\frac{E_0}{\sqrt{2}}\left[x\cos(\omega t)+y\sin(\omega t)\right], \tag{20}$$

which can be rewritten as

$$\frac{E_0}{2}\left(e^{i\omega t}\frac{x-iy}{\sqrt{2}}+e^{-i\omega t}\frac{x+iy}{\sqrt{2}}\right). \tag{21}$$

This form of the interaction is useful when making the rotating wave approximation (RWA), as the first (second) term corresponds to emission (absorption) of a photon.

The operators $z$, $\frac{x-iy}{\sqrt{2}}$, and $-\frac{x+iy}{\sqrt{2}}$ form the components of a spherical tensor operator $T^k$ of rank $k=1$, which means that the Wigner-Eckart theorem can be used to relate their matrix elements in a basis of angular momentum eigenstates [33, 37]. The Wigner-Eckart theorem states that for the $q$-component of a rank $k$ spherical tensor operator, the matrix element between two angular-momentum eigenstates is given by

$$\langle\gamma,\ell,m|\,T^k_q\,|\gamma',\ell',m'\rangle=(-1)^{\ell-m}\begin{pmatrix}\ell & k & \ell'\\ -m & q & m'\end{pmatrix}\langle\gamma,\ell||T^k||\gamma',\ell'\rangle, \tag{22}$$

where

$$\begin{pmatrix}\ell & k & \ell'\\ -m & q & m'\end{pmatrix} \tag{23}$$

is a Wigner 3-$j$ symbol [37], and $\langle\gamma,\ell||T^k||\gamma',\ell'\rangle$ is the reduced matrix element for the spherical tensor operator. Here $\ell,\ell'\geq 0$, $-\ell\leq m\leq\ell$ are the angular momentum quantum numbers, and $\gamma$, $\gamma'$ represents any additional quantum numbers needed to characterize the state. The Wigner 3-$j$ symbol is only nonzero if $\ell$, $k$, and $\ell'$ satisfy the triangle relation

$$\ell=|\ell'-k|,|\ell'-k|+1,\ldots,\ell'+k, \tag{24}$$

and if

$$m=q+m'. \tag{25}$$

The dipole-selection rules for linearly and circularly polarized light are an immediate consequence of applying the theorem for $k=1$, and $q=0$ (linear polarization) or $q=\pm1$ (circular polarization). For linear polarization the selection rules are

$$\begin{aligned}\Delta\ell&=\pm1,\\ \Delta m&=0,\end{aligned} \tag{26}$$

while for circular polarization they are

$$\begin{aligned}\Delta\ell&=\pm1,\\ \Delta m&=\pm1,\end{aligned} \tag{27}$$

where for $\Delta m$ the $+$-sign applies for absorption and the $-$-sign for emission.

## 2.2 Configuration interaction singles

In papers I and III the configuration interaction singles (CIS) method was used to compute the model parameters for He. For this reason, a brief overview of the method is provided. The starting point for applying CIS to closed-shell atoms is the restricted Hartree-Fock (HF) method, where the mean-field potential is assumed to be spherically symmetric. The spatial part of the one-particle orbitals can then be separated into a radial part times a spherical harmonic

$$\phi_i(\mathbf{r}) = \frac{P_i(r)}{r} Y^{\ell}_{m_\ell}(\theta, \varphi). \tag{28}$$

The radial orbital satisfies the restricted Hartree-Fock equations [37]

$$\left[ -\frac{1}{2}\frac{\mathrm{d}^2}{\mathrm{d}r^2} + \frac{\ell_i(\ell_i+1)}{2r^2} - \frac{Z}{r} + u_{\mathrm{HF}} \right] P_i(r) = \epsilon_i P_i(r), \tag{29}$$

where $u_{\mathrm{HF}}$ is the non-local Hartree-Fock potential, whose matrix elements are given by

$$\langle i | \, u_{\mathrm{HF}} \, | j \rangle = \sum_{a}^{\mathrm{occ}} (\langle ia | \, r_{12}^{-1} \, | ja \rangle - \langle ai | \, r_{12}^{-1} \, | ja \rangle). \tag{30}$$

The first term in the sum represents the direct interaction between electrons, and the second represents the exchange interaction. The HF groundstate wavefunction in second quantization can be written [38, 39]

$$|\Phi_0\rangle = \prod_{a}^{\mathrm{occ}} c^\dagger_{a+} c^\dagger_{a-} \, |0\rangle \tag{31}$$

where $c^\dagger_{a\pm}$ ($c_{a\pm}$) creates (annihilates) a particle in the spin-orbital $a\pm$, and $|0\rangle$ is the vacuum state of the Fock-space, $c_{a\pm} \, |0\rangle = 0$.

CIS allows for linear combinations of Slater determinants where one occupied orbital, $a$, of the ground state has been replaced by an unoccipied one, $p$. In the language of second quantization, and in the spin singlet approximation we have [38, 39]

$$|\Phi^p_a\rangle = \frac{1}{\sqrt{2}} (c^\dagger_{p+} c_{a+} + c^\dagger_{p-} c_{a-}) \, |\Phi_0\rangle \, . \tag{32}$$

Within CIS the total state of the system is then approximated by

$$|\Psi\rangle = \alpha_0 \, |\Phi_0\rangle + \sum_{a,p} \alpha^p_a \, |\Phi^p_a\rangle \, , \tag{33}$$

where the $a$ ($p$) index runs over occupied (unoccupied) orbitals. An approximate energy spectrum for the atom can be found by diagonalizing the full many-body Hamiltonian

$$H = \sum_i \frac{p_i^2}{2} - \frac{Z}{r_i} + \sum_{i<j} \frac{1}{r_{ij}} - E_{HF}, \tag{34}$$

within the singles subspace. Due to Brillioun's theorem, CIS does not provide any corrections to the ground state [37], but it does give rise to a spectrum of excited states. For convenience the HF energy of the ground state has been subtracted from $H$, so that $|\Phi_0\rangle$ is at zero energy.

A time dependent version of the theory, time-dependent configuration interaction singles (TDCIS), can be introduced by inserting the CIS ansatz into the TDSE [38–41]. The motivation for using CIS to compute atomic parameters was partly due to being able to compare model calculations with TDCIS calculations, as was done in paper I. In the length gauge the TDCIS equations of motion for the state coefficients are

$$\begin{aligned} i\frac{\mathrm{d}\alpha_0}{\mathrm{d}t} &= \sqrt{2}\mathbf{E}(t)\cdot\sum_{a,p}\alpha_a^p(t)\,\langle p|\,\mathbf{r}\,|a\rangle \\ i\frac{\mathrm{d}\alpha_a^p}{\mathrm{d}t} &= (\epsilon_p-\epsilon_a)\alpha_a^p(t) + \sum_{b,q}\alpha_b^q(t)(2\,\langle aq|\,r_{12}^{-1}\,|pb\rangle - \langle aq|\,r_{12}^{-1}\,|bp\rangle) \\ &+\mathbf{E}(t)\cdot\Big[\sqrt{2}\alpha_0(t)\,\langle a|\,\mathbf{r}\,|p\rangle - \sum_b \alpha_b^p(t)\,\langle b|\,\mathbf{r}\,|a\rangle + \sum_q \alpha_a^q(t)\,\langle q|\,\mathbf{r}\,|p\rangle\Big]. \end{aligned} \tag{35}$$

The factor $\sqrt{2}$ in front of the matrix elements involving the ground state is due to many electron (singlet) dynamics.

Due to the truncation of the full $N$-electron Hilbert space to the singles subspace, TDCIS calculations are not gauge invariant [36, 38]. Problems involving large ponderomotive energies are best described in the length gauge as recently showed by a comparison with velocity gauge [36].

## 2.3 Dressed states and quasienergies

### Floquet theory

If the Hamiltonian governing the dynamics of a system is periodic $H(t) = H(t+T)$, one can apply the Floquet theorem to write the solution of the TDSE on the form

$$|\psi(t)\rangle = \sum_n c_n e^{-i\lambda_n t}\,|\chi_n(t)\rangle\,, \tag{36}$$

where $|\chi_n(t)\rangle$ are $T$-periodic functions, the dressed states, and $\lambda_n$ are the corresponding quasienergies [42, 43]. Since the states $|\chi_n(t)\rangle$ are periodic, they can be thought of as vectors in an extended Hilbert space $\mathcal{H} \otimes L_2([0,T])$ [43]. The basis for the periodic part can be taken as the Fourier components $e^{im\omega t}$, and we can label the basis for the extended Hilbert space by $|\phi_n, m\rangle$, where $|\phi_n\rangle$ form a basis for the atomic part $\mathcal{H}$, while $m \in \mathbb{N}$ are the discrete Fourier indices. For a monochromatic field, the light–matter interaction term in the dipole approximation can be written on the form

$$\langle\phi_a| V(t) |\phi_b\rangle = V_{ab}^* e^{i\omega t} + V_{ab} e^{-i\omega t}. \tag{37}$$

The corresponding eigenstates for the monochromatic case are called semiclassical dressed states and satisfy the equation

$$\left(H(t) - i\frac{\mathrm{d}}{\mathrm{d}t}\right) |\chi_n(t)\rangle = \lambda_n |\chi_n(t)\rangle . \tag{38}$$

This is equivalent to a time independent eigenvalue problem [43]

$$H_F |\chi_n\rangle = \lambda_n |\chi_n\rangle \tag{39}$$

where $H_F$ is the infinite Floquet matrix, with matrix elements

$$\langle\phi_a, n| H_F |\phi_b, m\rangle = (\langle\phi_a| H_0 |\phi_b\rangle + m\omega\delta_{ab})\delta_{nm} + \delta_{nm+1} V_{ab}^* + \delta_{nm-1} V_{ab}. \tag{40}$$

The operator $e^{-iH_F t}$ represents a propagator on the extended Hilbert space [42, 43]. With outgoing boundary conditions, to be discussed further in Sec. 4.3, the quasienergies will have an imaginary part which can be interpreted as the ionization rate of the atom

$$\mathrm{Im}\,\lambda_n = -\frac{\gamma}{2}, \tag{41}$$

if the atom is initially prepared in the corresponding dressed state, $|\chi_n\rangle$.

**Quantum optics**

We will also consider the interaction between matter and a quantized single mode field. The basis states of the combined atom-photon system can be taken with the photon part in the Fock-basis $|\phi_a, N\rangle$, with the associated creation and annihilation operators acting according to [44, 45]

$$\begin{aligned} a |\phi_a, N\rangle &= \sqrt{N} |\phi_a, N-1\rangle , \\ a^\dagger |\phi_a, N\rangle &= \sqrt{N+1} |\phi_a, N+1\rangle . \end{aligned} \tag{42}$$

In the Coulomb gauge and within the dipole approximation we can write the interaction part of the Hamiltonian

$$H_I = \mathbf{r} \cdot \sigma \sqrt{\frac{2\pi\omega}{V}}(a + a^\dagger), \tag{43}$$

where $\sigma$ denotes the polarization vector and $V$ the quantization volume [45]. The eigenstates of the full Hamiltonian including the interaction are called dressed states [45]. In the limit of large photon numbers (high intensity) we can approximate $\sqrt{N+1} \approx \sqrt{N}$, and the matrix element of the interaction becomes [42, 44]

$$\langle \phi_i, N | H_I | \phi_j, N' \rangle = \frac{E_0}{2} \langle \phi_i | \mathbf{r} \cdot \sigma | \phi_j \rangle (\delta_{N+1N'} + \delta_{N-1N'}), \tag{44}$$

where $E_0 = 2\sqrt{\frac{2\pi\omega N}{V}}$. We thus see that in this limit the Floquet and quantum optics approaches are equivalent [42, 44]. In this thesis, we are concerned with intense fields, where the semiclassical approximation is valid. Thus, we expect the Floquet picture to be adequate. However, the quantum optics perspective brings much clarity to the physics, as shown in paper III.

# 3 Photoionization from a Rabi oscillating atom

Following the general background that was introduced in the previous section, the focus will now shift to describing the specific systems and physical processes that are the subject of the thesis. Alongside this will also follow a description of the techniques employed to construct the models for these systems. The first process that will be considered is resonant ionization of atoms with XUV fields, illustrated in Fig. 1. Specifically, the focus will be on what happens when the laser is intense enough to drive Rabi oscillations between the resonant states, which is the case for FELs such as FERMI, see Refs. [2, 10] and papers I and II.

Nonlinear, resonant photoionization of atoms and molecules have been studied by many authors. Some examples include Beers and Armstrong, Knight and Holt, Raymer and Reinhardt [11–13], who employed the resolvent operator and effective Hamiltonians, which will be explored further in Sec. 4. LaGattuta and Girju et al. studied the process by numerically solving the TDSE for hydrogen atoms [46, 47], and Sun and Lu, and also Palacios, Bachau and Martín have performed time dependent simulations for molecules [48, 49]. Some insight has also come through the study of the quasienergies of the time-independent Floquet Hamiltonian [13, 42, 47] and in the rotating frame of a circularly polarized field [50], which give information about ac Stark shifts and ionization rates.

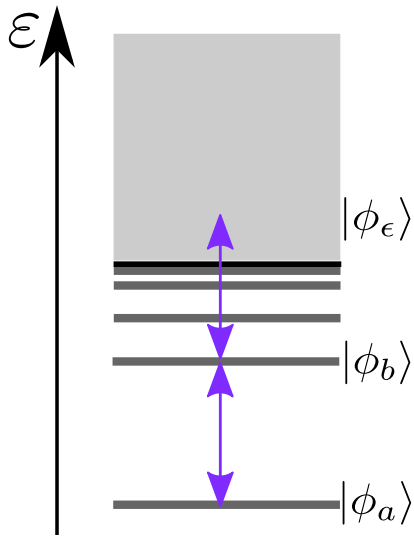


**Figure 1:** Schematic energy diagram of resonant two-photon ionization. The photon energy of the driving field is nearly resonant with the transition from $|\phi_a\rangle$ to $|\phi_b\rangle$, as indicated by the purple arrows. Absorption of two photons from $|\phi_a\rangle$ reaches the continuum state $|\phi_\epsilon\rangle$.

This section will outline how time-dependent perturbation theory can be used to describe photoionization from an atom undergoing Rabi oscillations. The theory was used in the analytic model of paper I, and related models were employed in papers II and IV.

### 3.1 Resonantly driven two-level systems and Rabi oscillations

Consider a system, as in Fig. 2 (a), consisting of two states $|\phi_a\rangle$ and $|\phi_b\rangle$, with energies $\epsilon_a$ and $\epsilon_b$, and energy difference $\omega_{ba} = \epsilon_b - \epsilon_a$. They are coupled via an interaction with a laser with frequency $\omega \approx \omega_{ba}$, such that the detuning $\Delta\omega = \omega - \omega_{ba}$ is small. Coupling to other states is assumed to be negligible. In the length gauge with the laser linearly polarized along the $z$-axis, the interaction between the two states is

$$V_{ba}(t) = E_0 z_{ba} \cos(\omega t) = \frac{\Omega}{2}\left(e^{i\omega t} + e^{-i\omega t}\right), \tag{45}$$

where $\Omega = E_0 z_{ba}$ is the Rabi frequency and $z_{ba}$ is the dipole matrix element connecting $|\phi_a\rangle$ and $|\phi_b\rangle$. For simplicity, the field has been assumed to be monochromatic.

The time dependent state of the two-level system can be written as

$$|\psi(t)\rangle = a(t)e^{-i\epsilon_a t}|\phi_a\rangle + b(t)e^{-i\epsilon_b t}|\phi_b\rangle, \tag{46}$$

where $a(t)$ and $b(t)$ are the interaction picture amplitudes of $|\phi_a\rangle$ and $|\phi_b\rangle$. In the RWA,

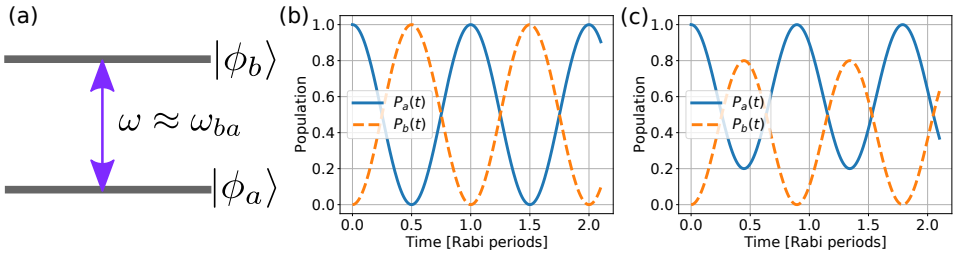


**Figure 2:** (a) Resonant driving of the two-level system consisting of $|\phi_a\rangle$ and $|\phi_b\rangle$. (b) The populations $P_a(t)$ (blue, solid) and $P_b(t)$ (orange, dashed), when $\Delta\omega = 0$. (c) same as (b), but with a detuning of $\Delta\omega = 0.5\Omega$.

together with the initial condition $a(0) = 1$, $a(t)$ and $b(t)$ are given by [51–53]

$$a(t) = [\cos(Wt/2) - i(\Delta\omega/W)\sin(Wt/2)]\, e^{i\Delta\omega t/2}, \tag{47a}$$

$$b(t) = -i\frac{\Omega}{W}\sin(Wt/2)e^{-i\Delta\omega t/2}. \tag{47b}$$

Here the generalized Rabi frequency $W = \sqrt{\Omega^2 + \Delta\omega^2}$ has been introduced. The populations, $P_a(t)$ and $P_b(t)$, have the form

$$P_a(t) = \cos^2(Wt/2) + \frac{\Delta\omega^2}{W^2}\sin^2(Wt/2) \tag{48a}$$

$$P_b(t) = \frac{\Omega^2}{W^2}\sin^2(Wt/2), \tag{48b}$$

and they oscillate at the generalized Rabi frequency $W$. In the special case $\Delta\omega = 0$, the population can be completely transferred from $|\phi_a\rangle$ to $|\phi_b\rangle$, and then back to $|\phi_a\rangle$, see Fig. 2 (b). The duration of one such cycle, is given by the Rabi period $T_R = 2\pi/\Omega$. When $\Delta\omega \neq 0$, the amplitude of the oscillations are reduced, such that $|\phi_a\rangle$ is never completely depopulated, see Fig. 2 (c). For the FEL experiments that we are interested in describing, the field is in the weak field strength and resonant regimes as classified by Autler and Townes, $\Omega \ll \omega_{ba}$ and $\omega \approx \omega_{ba}$ respectively, where the RWA is expected to be a good approximation [52].

If the detuning is zero, then the amplitudes and populations can also be found when an envelope $f(t)$ is introduced to the electric field. In this case the populations follow the area theorem [54]

$$P_a(t) = \cos^2(\theta(t)/2), \tag{49a}$$

$$P_b(t) = \sin^2(\theta(t)/2), \tag{49b}$$

where $\theta(t)$ is the pulse area

$$\theta(t) = \int_{t_0}^{t} \mathrm{d}t' \Omega f(t'). \tag{50}$$

Here $t_0$ represents the start of the pulse, and the population is assumed to initially be in the ground state, $a(t_0) = 1$.

The idea behind the model used in paper I, is to assume that Eq. (46) serves as a good zeroth order approximation for the full state of the system, and then employ time-dependent perturbation theory with Eq. (46) as the starting point. For this to be a good idea, the coupling to states outside of the two-level system can not be too strong, i.e. other bound states should have negligible population during the interaction, and the probability of ionization should be small at the end of the pulse.

### 3.2 Hilbert space partitioning: $P + Q = 1$

We are interested in describing the dynamics in two subspaces, which we will call $\mathcal{P}$ and $\mathcal{Q}$. In general $\mathcal{P}$ can be spanned by any number of states, but for the purposes of this thesis, we will focus on the case where it is spanned by two eigenstates of the interaction-free Hamiltonian $H_0$ that are resonantly coupled. The subspace $\mathcal{Q}$ is then taken as the orthogonal complement of $\mathcal{P}$, i.e. $\mathcal{Q} = \mathcal{P}^\perp$. We will also require the orthogonal projection operators $P$ and $Q$ that project onto the respective subspaces. In terms of the field-free eigenstates the projection operators can be written

$$P = |\phi_a\rangle\langle\phi_a| + |\phi_b\rangle\langle\phi_b| \tag{51a}$$

$$Q = 1 - P = \sum_{n\neq a,b} |\phi_n\rangle\langle\phi_n| \,. \tag{51b}$$

They satisfy the usual properties of orthogonal projection operators

$$P + Q = 1, \tag{52a}$$

$$P^2 = P, Q^2 = Q \tag{52b}$$

$$PQ = QP = 0 \tag{52c}$$

$$P^\dagger = P, Q^\dagger = Q. \tag{52d}$$

Additionally, since they are diagonal in the eigenbasis of $H_0$, both of the projection operators commute with $H_0$,

$$[H_0, P] = [H_0, Q] = 0. \tag{53}$$

The partitioning described above is illustrated in Fig. 3, with the two subspaces $\mathcal{P}$ and $\mathcal{Q}$ indicated. In this chapter the projection operators will be used to construct a time-dependent perturbation theory where Rabi oscillations are the zeroth order solution. Projection techniques will also be used in Chap. 4 to separate out a resonant subspace, and to construct an effective Hamiltonian for $\mathcal{P}$.

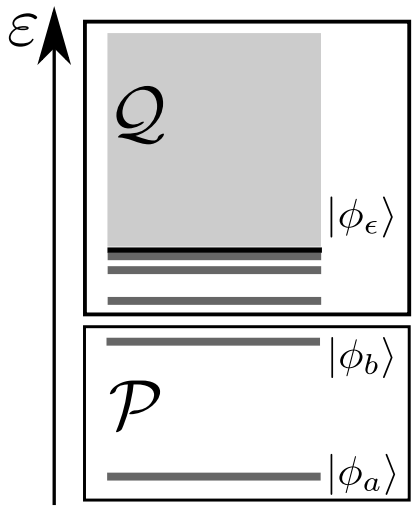


Figure 3: The partitioning of the atomic levels into a resonant subspace $\mathcal{P}$ (consisting of $|\phi_a\rangle$ and $|\phi_b\rangle$, and its complement $\mathcal{Q}$, where the final state in two-photon ionization $|\phi_\epsilon\rangle$ resides.

### 3.3 Perturbative transitions to states outside the two-level system

In the following we will use perturbation theory to compute transitions to states outside the Rabi oscillating two-level system $\mathcal{P}$. The interaction term $V(t)$ is split into one part that generates the Rabi dynamics, and a remainder, that will serve as the perturbation. The amplitudes will be derived in a slightly different way than what was done in the SI of paper I, where an iteration of the Dyson equation was used. For this problem the two approaches give equivalent results. The Dyson equation was also used to construct the models of papers II, IV and V, and will be discussed further in Sec. 5.1.

#### Interaction picture with respect to the Rabi Hamiltonian

Consider the time-dependent Hamiltonian

$$H(t) = \widetilde{H}_0(t) + \widetilde{V}(t) \tag{54}$$

with time-dependent zeroth order Hamiltonian $\widetilde{H}_0(t) = H_0 + V_{\mathrm{Rabi}}(t)$ and perturbation $\widetilde{V}(t) = V(t) - V_{\mathrm{Rabi}}(t)$, where $V_{\mathrm{Rabi}}(t)$ is the interaction between $|\phi_a\rangle$ and $|\phi_b\rangle$ in the RWA. The interaction $\widetilde{V}(t)$ allows for transitions between $\mathcal{P}$ and $\mathcal{Q}$, and within $\mathcal{Q}$, but not within $\mathcal{P}$ if the RWA is made. Counter-rotating terms can be included in the perturbative expansion, as was done for some processes considered in paper IV.

The time-evolution operator $U(t,t_0)$ for $H(t)$ satisfies the Schrödinger equation

$$i\frac{\mathrm{d}U(t,t_0)}{\mathrm{d}t} = H(t)U(t,t_0), \tag{55}$$

with initial condition $U(t_0,t_0)=1$. Similarly, for the zeroth order time-evolution operator we have,

$$i\frac{\mathrm{d}\widetilde{U}_0(t,t_0)}{\mathrm{d}t} = \widetilde{H}_0(t)\widetilde{U}_0(t,t_0), \tag{56a}$$

$$-i\frac{\mathrm{d}\widetilde{U}_0^\dagger(t,t_0)}{\mathrm{d}t} = \widetilde{U}_0^\dagger(t,t_0)\widetilde{H}_0(t). \tag{56b}$$

The zeroth order time-evolution operator acts in the following way

$$\widetilde{U}_0(t,0)\left|\phi_a\right\rangle = a(t)e^{-i\epsilon_a t}\left|\phi_a\right\rangle + b(t)e^{-i\epsilon_b t}\left|\phi_b\right\rangle, \tag{57a}$$

$$\widetilde{U}_0(t,0)\left|\phi_c\right\rangle = e^{-i\epsilon_c t}\left|\phi_c\right\rangle, \left|\phi_c\right\rangle \in \mathcal{Q}. \tag{57b}$$

We can now define an interaction picture time-evolution operator

$$U_I(t,t_0) = \widetilde{U}_0^\dagger(t,0)U(t,t_0)\widetilde{U}_0(t_0,0), \tag{58}$$

in analogy with the usual definition of $U_I(t,t_0)$ when $H_0$ is not time-dependent

$$U_I(t,t_0) = e^{iH_0t}U(t,t_0)e^{-iH_0t_0}. \tag{59}$$

Using Eqs. (55) and (56b), it is possible to find an evolution equation for $U_I(t,t_0)$

$$i\frac{\mathrm{d}U_I(t,t_0)}{\mathrm{d}t} = \widetilde{V}_I(t)U_I(t,t_0), \tag{60}$$

where the interaction picture operator

$$\widetilde{V}_I(t) = \widetilde{U}_0^\dagger(t,0)\widetilde{V}(t)\widetilde{U}_0(t,0), \tag{61}$$

has been introduced.

Equation (60) has a formal solution in terms of a time-ordered exponential,

$$U_I(t,t_0) = \mathcal{T}\exp\left[-i\int_{t_0}^{t}\mathrm{d}t'\widetilde{V}_I(t')\right], \tag{62}$$

or equivalently in terms of a Dyson series,

$$U_I(t,t_0) = 1 - i\int_{t_0}^{t}\mathrm{d}t'\widetilde{V}_I(t') + (-i)^2\int_{t_0}^{t}\mathrm{d}t'\int_{t_0}^{t'}\mathrm{d}t''\widetilde{V}_I(t')\widetilde{V}_I(t'') + \ldots \tag{63}$$

In the following we will have $t_0 = 0$, so that the relationship between the time-evolution operators in the two pictures is,

$$U_I(t,0) = \widetilde{U}_0^\dagger(t,0)U(t,0). \tag{64}$$

**First and second order transition amplitudes**

To compute the transition probability of starting in $|\phi_a\rangle$ and ending up in $|\phi_\epsilon\rangle$, we can compute the amplitude [33]

$$\alpha_\epsilon(t) = \langle\phi_\epsilon|\psi_I(t)\rangle = \langle\phi_\epsilon| U_I(t,0) |a\rangle = \langle\phi_\epsilon| \widetilde{U}_0^\dagger(t,0) U(t,0) |\phi_a\rangle . \tag{65}$$

Since $\widetilde{U}_0(t,0)$ corresponds to the field-free time-evolution for the states in $\mathcal{Q}$, the interaction picture amplitude $\alpha_\epsilon(t)$ will differ from the transition amplitude in the Schrödinger picture $\langle\phi_\epsilon| U(t,0) |\phi_a\rangle$ by a time-dependent phase factor $e^{i\epsilon t}$, and the two expressions will therefore correspond to the same transition probability [33].

Inserting the Dyson series Eq. (63) into Eq. (65), and keeping terms up to second order yields

$$\alpha_\epsilon(t) \approx -i \int_0^t \mathrm{d}t' \, \langle\phi_\epsilon| \widetilde{V}_I(t') |\phi_a\rangle + (-i)^2 \int_0^t \mathrm{d}t' \int_0^{t'} \mathrm{d}t'' \, \langle\phi_\epsilon| \widetilde{V}_I(t') \widetilde{V}_I(t'') |\phi_a\rangle . \tag{66}$$

We can now split $\alpha_\epsilon(t)$ into a first and second order amplitude

$$\alpha_\epsilon^{(1)}(t) = -i \int_0^t \mathrm{d}t' \, \langle\phi_\epsilon| \widetilde{V}_I(t') |\phi_a\rangle , \tag{67a}$$

$$\alpha_\epsilon^{(2)}(t) = (-i)^2 \int_0^t \mathrm{d}t' \int_0^{t'} \mathrm{d}t'' \, \langle\phi_\epsilon| \widetilde{V}_I(t') \widetilde{V}_I(t'') |\phi_a\rangle . \tag{67b}$$

These expressions can in principle be used when the interaction strength is controlled by an envelope, however the analytical calculations simplify greatly when a flat-top envelope is used, since then the amplitudes $a(t)$ and $b(t)$ are known analytically, see Sec. 3.1. It should be noted that there exists some envelopes where an analytical solution can be found [14].

Using the definition of $\widetilde{V}_I(t)$ in Eq. (61), the first order amplitude can be written as

$$\alpha_\epsilon^{(1)}(t) = -i \int_0^t \mathrm{d}t' \, \langle\phi_\epsilon| \widetilde{U}_0^\dagger(t',0) \widetilde{V}(t') \widetilde{U}_0(t',0) |\phi_a\rangle . \tag{68}$$

For the application to resonant two-photon ionization by an FEL pulse, $|\phi_\epsilon\rangle$ can not be reached energetically from $|\phi_a\rangle$ by absorbing a single photon (one $\widetilde{V}$ interaction). Therefore, $\widetilde{U}_0(t',0) |\phi_a\rangle$ can be reduced to $b(t')e^{-i\epsilon_b t'} |\phi_b\rangle$. This means that

$$\alpha_\epsilon^{(1)}(t) = -i \int_0^t \mathrm{d}t' e^{i(\epsilon-\epsilon_b)t'} b(t') z_{\epsilon b} E_0 \frac{e^{i\omega t'} + e^{-i\omega t'}}{2}, \tag{69}$$

where the dipole matrix element $z_{\epsilon b}$ between $|\phi_b\rangle$ and $|\phi_\epsilon\rangle$ has been introduced. The term containing $e^{i\omega t'}$ does not lead to energy conservation in the long-time limit, and is therefore

neglected (RWA). Since we have the form of $b(t)$ from Eq. (47b), the integral in Eq. (69) can be performed analytically

$$\alpha_\epsilon^{(1)}(t) = i\frac{z_{\epsilon b}E_0\Omega}{2W}\left[e^{\frac{it\Delta\epsilon_-}{2}}\frac{\sin\left(\frac{t\Delta\epsilon_-}{2}\right)}{\Delta\epsilon_-} - e^{\frac{it\Delta\epsilon_+}{2}}\frac{\sin\left(\frac{t\Delta\epsilon_+}{2}\right)}{\Delta\epsilon_+}\right], \tag{70}$$

where

$$\Delta\epsilon_\pm = \epsilon - \epsilon_a - 2\omega + \frac{\Delta\omega}{2} \mp \frac{W}{2}. \tag{71}$$

This amplitude corresponds to a photoelectron spectrum with two main peaks spaced symmetrically around $E_{\text{kin}} = 2\omega - I_p$, with the spacing given by the generalized Rabi frequency $W$. Such a splitting in the spectrum is typically called an Autler-Townes (AT) doublet [52], although in the context of resonant photoionization a Knight doublet would also be a suitable name [12]. Why the doublet arises can be deduced from the amplitude $b(t)$. The Rabi oscillations introduce two frequency components

$$b(t) \propto e^{iWt/2} - e^{-iWt/2}, \tag{72}$$

that are split by the generalized Rabi frequency, which are then imprinted on the amplitude of the ionized electrons.

For the second order amplitude, only $|\phi_a\rangle$ generates energetically allowed terms if we consider $E_{\text{kin}} \approx 2\omega - I_p$, and we can therefore write

$$\begin{aligned}\alpha_\epsilon^{(2)}(t) = (-i)^2 \sum_{c\in\mathcal{Q}} \int_0^t dt' \int_0^{t'} dt'' \, \langle\phi_\epsilon|\, \widetilde{V}(t')\,|c\rangle\langle c|\, \widetilde{V}(t'')\,|\phi_a\rangle \\ \times e^{i(\epsilon-\epsilon_c)t'} e^{i(\epsilon_c-\epsilon_a)t''} a(t'').\end{aligned} \tag{73}$$

As before we neglect counter-rotating terms in the interaction, which yields

$$\begin{aligned}\alpha_\epsilon^{(2)}(t) = (-i)^2 \sum_{c\in\mathcal{Q}} \frac{z_{\epsilon c}z_{ca}E_0^2}{8} \int_0^t dt' \int_0^{t'} dt'' \exp\left[-i(\epsilon_c + \omega - \epsilon)t'\right] \\ \times \exp\left[-i(\epsilon_a + \omega - \Delta\omega/2 - \epsilon_c)t''\right] a(t'').\end{aligned} \tag{74}$$

Since we again have a rather simple expression for the Rabi amplitude $a(t'')$ from Eq. (47a),

the double integrals can be performed analytically, resulting in

$$\begin{aligned}\alpha_\epsilon^{(2)}(t) = -i\sum_{c\in\mathcal{Q}} \frac{z_{\epsilon c} z_{ca} E_0^2}{4} \Bigg\{ & \frac{(1-\Delta\omega/W)\exp\left(\frac{it\Delta\epsilon_-}{2}\right)\sin\left(\frac{t\Delta\epsilon_-}{2}\right)}{\tilde{\omega}_c^-\Delta\epsilon_-} \\ & + \frac{(1+\Delta\omega/W)\exp\left(\frac{it\Delta\epsilon_+}{2}\right)\sin\left(\frac{t\Delta\epsilon_+}{2}\right)}{\tilde{\omega}_c^+\Delta\epsilon_+} \\ & - \frac{(1-\Delta\omega/W)\tilde{\omega}_c^+ + (1+\Delta\omega/W)\tilde{\omega}_c^-}{\tilde{\omega}_c^-\tilde{\omega}_c^+(\epsilon-\epsilon_c-\omega)} \exp\left[i(\epsilon-\epsilon_c-\omega)\frac{t}{2}\right] \\ & \times \sin\left[(\epsilon-\epsilon_c-\omega)\frac{t}{2}\right] \Bigg\}.\end{aligned} \tag{75}$$

Here a one-photon detuning, $\tilde{\omega}_c^\pm = \epsilon_a + \omega - \epsilon_c - \Delta\omega/2 \pm W/2$, relative to the states in $\mathcal{Q}$ has been introduced.

The first two terms in Eq. (75) are analogous to the ones that appear in Eq. (70), i.e. they will give rise to two peaks in the photoelectron spectrum, that are separated by $W$. Note however that due to the form of $a(t)$,

$$a(t) \propto (1-\Delta\omega/W)e^{iWt/2} + (1+\Delta\omega/W)e^{-iWt/2}, \tag{76}$$

the two frequency components no longer have the same strength if $\Delta\omega \neq 0$, and they also have a different phase relation compared to what was found in $\alpha_\epsilon^{(1)}(t)$. The last term in Eq. (75) will give rise to peaks at energies one-photon above each state in $\mathcal{Q}$, which means that it can be neglected if we are only interested in the spectrum in the vicinity of $E_{\text{kin}} = 2\omega - I_p$. Such peaks can be seen in Fig. 6 of Ref. [47].

The difference between the processes that are represented by $\alpha_\epsilon^{(1)}(t)$ and $\alpha_\epsilon^{(2)}(t)$ is illustrated in Fig. 4. The Rabi oscillations allow $\alpha_\epsilon^{(1)}(t)$ to be of first order in $E_0$, since once the electron has reached the excited state it only requires one extra photon to ionize. Since $\alpha_\epsilon^{(2)}(t)$ represents perturbative two-photon ionization from $|\phi_a\rangle$ via the states in $\mathcal{Q}$, it has the $E_0^2$ scaling that is expected in non-resonant two-photon ionization.

### 3.4 Perturbed wavefunctions

When evaluating the second order amplitude $\alpha_\epsilon^{(2)}(t)$, it is necessary to sum up the contributions from all the states in $\mathcal{Q}$. This can be done by constructing the perturbed wavefunctions

$$|\rho_{\neq b}^\pm\rangle = \sum_{c\in\mathcal{Q}} \frac{z_{ca}|c\rangle}{\epsilon_a + \omega - \frac{\Delta\omega}{2} \pm \frac{W}{2} - \epsilon_c}, \tag{77}$$

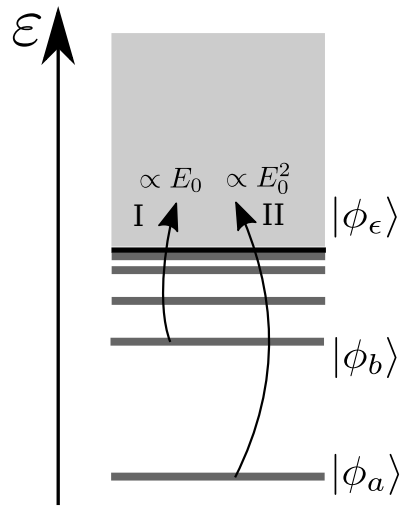


**Figure 4:** Illustration of the processes involved in the first (I) and second (II) order ionization amplitudes, $\alpha_\epsilon^{(1)}(t)$ and $\alpha_\epsilon^{(2)}(t)$, and their scaling with the electric field strength $E_0$.

where the label $\neq b$ indicates that the state $|\phi_b\rangle$ should not be included in the sum, as the coupling between $|\phi_a\rangle$ and $|\phi_b\rangle$ is already included in the zeroth order wavefunction. The second order ionization amplitude can now be written in terms of the perturbed wavefunctions as

$$\begin{aligned}\alpha_\epsilon^{(2)}(t) = -i\frac{E_0^2}{4}\Bigg[&\frac{(1-\Delta\omega/W)\exp\left(\frac{it\Delta\epsilon_-}{2}\right)\sin\left(\frac{t\Delta\epsilon_-}{2}\right)}{\Delta\epsilon_-}\langle\phi_\epsilon|\, z|\rho_{\neq b}^-\rangle \\ &+\frac{(1+\Delta\omega/W)\exp\left(\frac{it\Delta\epsilon_+}{2}\right)\sin\left(\frac{t\Delta\epsilon_+}{2}\right)}{\Delta\epsilon_+}\langle\phi_\epsilon|\, z|\rho_{\neq b}^+\rangle\Bigg].\end{aligned} \tag{78}$$

If the states in $\mathcal{Q}$ lie sufficiently far away from $|\phi_b\rangle$, then we can neglect the variation of $|\rho_{\neq b}^\pm\rangle$ with $\omega$ and $W$, and use a single perturbed wavefunction

$$|\rho_{\neq b}\rangle = \sum_{c\in\mathcal{Q}}\frac{z_{ca}\,|c\rangle}{\epsilon_a+\omega_{ba}-\epsilon_c}. \tag{79}$$

Then $\alpha_\epsilon^{(2)}(t)$ can be further simplified

$$\begin{aligned}\alpha_\epsilon^{(2)}(t) = -i\frac{E_0^2 z_{\epsilon\rho\neq b}}{4}\Bigg[&\frac{(1-\Delta\omega/W)\exp\left(\frac{it\Delta\epsilon_-}{2}\right)\sin\left(\frac{t\Delta\epsilon_-}{2}\right)}{\Delta\epsilon_-} \\ &+\frac{(1+\Delta\omega/W)\exp\left(\frac{it\Delta\epsilon_+}{2}\right)\sin\left(\frac{t\Delta\epsilon_+}{2}\right)}{\Delta\epsilon_+}\Bigg],\end{aligned} \tag{80}$$

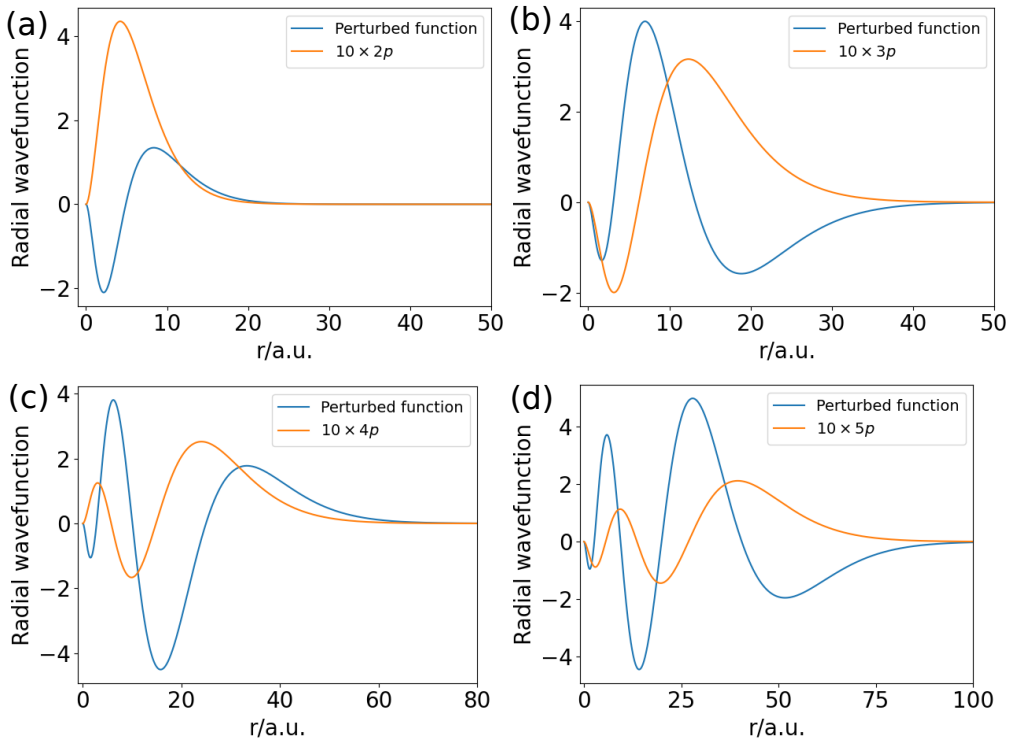


**Figure 5:** Helium CIS orbitals of excited states $|\phi_b\rangle$ (orange) and the corresponding perturbed wavefunctions $|\rho_{\neq b}\rangle$ (blue) for (a) $1s2p$, (b) $1s3p$, (c) $1s4p$ and (d) $1s5p$. In each case the excited state orbital has been multiplied by 10 to be of the same scale as the perturbed orbital.

where the dipole matrix element $z_{\epsilon\rho\neq b} = \langle\phi_\epsilon|\, z|\rho_{\neq b}\rangle$ has been introduced.

Figure 5 compares the excited state CIS orbitals to that of the corresponding $|\rho_{\neq b}\rangle$ for the first few states in the $1snp$ series of He. The figures show that the perturbed orbital has a very similar character to that of the following excited orbital, as they have the same number of nodes for instance. This is reasonable, since that is the state with the smallest energy denominator in Eq. (77), and hence it should give a relatively large contribution.

In order to compare the strength of process I and II, one can consider the following quantity

$$R = \left| \frac{E_0 z_{\epsilon\rho\neq b}}{2 z_{\epsilon b}} \right|, \tag{81}$$

which is the ratio of the prefactors appearing in $\alpha_\epsilon^{(1,2)}(t)$ ($R < 1$ implies that process I is stronger). This is given for a few excited states of He in Tab. 1, together with the dipole matrix elements required for its calculation. Both $s$ and $d$ partial waves are considered for the final state. An electric field strength of $E_0 = 0.02388$ a.u., corresponding to $I = 2 \times 10^{13}$ W/cm$^2$, was used for the calculations of $R$.

**Table 1:** Energies (CIS) and ionization dipole matrix elements for a few excited states helium. The supersprict indicates the partial wave of the final state. $E_0 = 0.02388$ was used to compute $R$.

| $\phi_b$ | $\epsilon_b$ | $z^s_{\epsilon b}$ | $z^d_{\epsilon b}$ | $z^s_{\epsilon\rho\neq b}$ | $z^d_{\epsilon\rho\neq b}$ | $R^s$ | $R^d$ |
|---|---|---|---|---|---|---|---|
| $1s2p$ | 0.797208 | 0.02330524 | 0.04426126 | 0.22070142 | −1.80455228 | 0.113 | 0.487 |
| $1s3p$ | 0.863682 | 0.0143939 | 0.02074873 | 0.12234853 | −1.41010052 | 0.101 | 0.811 |
| $1s4p$ | 0.887248 | 0.00931097 | 0.01298371 | 0.10563507 | −1.30034468 | 0.135 | 1.20 |
| $1s5p$ | 0.898233 | 0.00671581 | 0.00884202 | 0.10291827 | −1.21846422 | 0.183 | 1.65 |
| $1s6p$ | 0.904228 | 0.00514567 | 0.00666799 | 0.10313639 | −1.19142248 | 0.239 | 2.13 |
| $1s7p$ | 0.907853 | 0.00404325 | 0.00535528 | 0.10237491 | −1.19054604 | 0.302 | 2.65 |
| $1s8p$ | 0.910211 | 0.00336541 | 0.00429486 | 0.10480058 | −1.16349997 | 0.372 | 3.23 |

From Tab. 1 we can see that the first order process is stronger for $s$-waves for all the states considered, while for $d$-waves the second order process is stronger for $1s4p$ and above. For process I, the two partial waves have quite similar dipole moments, while for process II there is a difference of about one order of magnitude at the considered field strength.

### 3.5 Ionization rate for the two-level system

With our expressions for $\alpha^{(1)}_\epsilon(t)$ and $\alpha^{(2)}_\epsilon(t)$, we can now look at $|\alpha_\epsilon(t)|^2$

$$\begin{aligned}|\alpha_\epsilon(t)|^2 \approx \frac{\sin^2[\Delta\epsilon_- t/2]}{\Delta\epsilon_-^2}\left|\frac{z_{\epsilon b}E_0\Omega}{2W} - (1-\Delta\omega/W)\frac{z_{\epsilon\rho\neq b}E_0^2}{4}\right|^2 \\ + \frac{\sin^2[\Delta\epsilon_+ t/2]}{\Delta\epsilon_+^2}\left|\frac{z_{\epsilon b}E_0\Omega}{2W} + (1+\Delta\omega/W)\frac{z_{\epsilon\rho\neq b}E_0^2}{4}\right|^2,\end{aligned} \tag{82}$$

where a cross term between the $\Delta\epsilon_\pm$ components has been dropped. In the limit of large $t$ we have $\sin^2[\Delta\epsilon t/2]/\eta^2 \to \pi\delta(\Delta\epsilon)t/2$ [33], and integrating over $\epsilon$ gives an ionization rate of

$$\gamma = \frac{\pi}{2}\left[\left|\frac{z_{\epsilon b}E_0\Omega}{2W} - \left(1-\frac{\Delta\omega}{W}\right)\frac{z_{\epsilon\rho\neq b}E_0^2}{4}\right|^2 + \left|\frac{z_{\epsilon b}E_0\Omega}{2W} + \left(1+\frac{\Delta\omega}{W}\right)\frac{z_{\epsilon\rho\neq b}E_0^2}{4}\right|^2\right]. \tag{83}$$

In the case when the detuning is zero, $\gamma$ simplifies to

$$\gamma = \pi\left(\frac{z_{\epsilon b}E_0^2}{2^2} + \frac{z_{\epsilon\rho\neq b}E_0^4}{2^4}\right) = \frac{\gamma_b+\gamma_a}{2}, \tag{84}$$

where the ionization rates for the one-photon process from $|\phi_b\rangle$, and the two-photon pro-

cess from $|\phi_a\rangle$ have been introduced

$$\gamma_b = 2\pi \frac{z_{\epsilon b} E_0^2}{2^2}, \tag{85a}$$

$$\gamma_a = 2\pi \frac{z_{\epsilon \rho \neq b} E_0^4}{2^4}. \tag{85b}$$

Equation (84) reflects the fact that when $\Delta\omega = 0$, the atom spends on average 50% of the time in both the ground and excited states, and therefore the rates of the two ionization processes are reduced by one half compared to the rate from Fermi's Golden rule. $\gamma$ represents a kind of Rabi-period averaged rate, and the instantaneous rate will depend on the relative strength of the different processes, and also on the instantaneous populations. In general, it is not possible to define an ionization rate that holds for all time scales, and accounting for depletion of the two-level system can lead to quite different rates on short and long time scales [11, 13].

### 3.6 Dynamical spectral features

That an AT doublet should appear in the photoelectron spectrum for resonant photoionization was first suggested by Knight [12]. When the first order ionization amplitude is dominant, the ionization process is similar to probing a resonantly driven two-level system by a weak transition to a third level $|\phi_c\rangle$, cf. Fig. 6 (a) and (b), which is the kind of process considered by Autler and Townes [52]. Fig. 6 (d) shows the population in $|\phi_c\rangle$ as a function of the detuning $\Delta\omega_{cb}$ of the probe field. Due to the dressing of the two-level system by the driving field, the expected peak at zero detuning is split into two peaks separated by $\Omega$ in the resonant case, or $W$ if there is a detuning of the strongly driven transition.

Figure 6 (e) shows an AT doublet in the photoelectron spectrum for resonant ionization via $1s4p$ in He, calculated using $\alpha_\epsilon^{(1)}(t)$, and a pulse duration of $1.5T_R$. The simple doublet structure is modified when $\alpha_\epsilon^{(1)}(t)$ and $\alpha_\epsilon^{(2)}(t)$ are considered together, since it is now possible to have interference effects between the two ionization processes, which will affect the symmetry of the doublet. This was explored in papers I and III. The AT doublet is also present when the dynamics is probed by an attosecond pulse train in a RABBIT-like setup [55], which was explored in paper IV. The AT doublet in resonant photoionization has also been extensively studied in time-dependent numerical simulations [46–49].

A related doublet structure was suggested by Grobe and Eberly to be present when a laser field that can drive one-photon ionization is resonant with a transition in the ion core [56], see Fig. 6 (c). The resulting spectrum, calculated with the analytical model of paper II, is illustrated in Fig. 6 (f), which displays the photoelectron spectrum as a function of $E_{\text{kin}}$ relative to the expected photoelectron peak at $\omega - I_p$. The solid line represents the total signal,

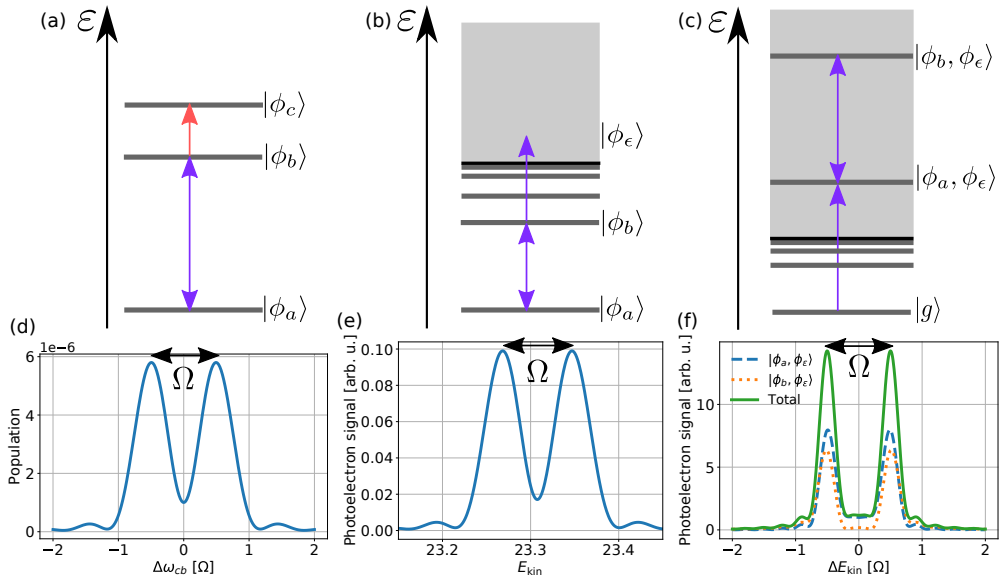


**Figure 6:** Illustration of different situation where a doublet appears. (a) Resonant driving of two-level system, with a weak probe field coupling to a third level $|\phi_c\rangle$. (b) Resonant two-photon ionization. (c) One-photon ionization, where the photon energy is resonant with a transition in the ion. (d) Population in the $|\phi_c\rangle$ as a function of the detuning $\Delta\omega_{cb}$. (e)Photoelectron signal from the lowest order amplitude, $\alpha_\epsilon^{(1)}(t)$. (f) Photoelectron signal as a function of the kinetic energy relative to the expected one-photon peak, $\Delta E_{\text{kin}} = E_{\text{kin}} - (\omega - I_p)$. The green, solid line, corresponds to the total signal, and the dashed ($|\phi_a\rangle$) and dotted ($|\phi_b\rangle$) lines show the spectrum resolved on the two ionic states.

and the dashed and dotted lines are the contributions from the two ionic channels $|\phi_a\rangle$ and $|\phi_b\rangle$, respectively. The dressing of the ion splits the photoelectron peak into a doublet, that again is separated by $\Omega$. The Grobe-Eberly (GE) doublet has been experimentally observed at optical [57] and at XUV wavelengths in paper II. Its relation to entanglement between the ion and the photoelectron was studied in paper II.

The doublet is only present for pulses that are sufficiently long, see paper I and Ref. [58], i.e. it can not be spectrally resolved by short pulses (compared to the Rabi period). A complementary view is that the photoelectrons emitted during different Rabi periods can interfere, since the Rabi amplitudes $a(t)$ and $b(t)$ change sign once per Rabi period. This can explain why a doublet forms already after one period for $\alpha_\epsilon^{(2)}(t)$, while a spectrum calculated using only $\alpha_\epsilon^{(1)}(t)$ would still show a single peak at this stage, as discussed in paper I. Because $a(t)$ and $b(t)$ oscillate out of phase, $a(t)$ has changed sign once during the first Rabi period, while $b(t)$ has the same sign during the same interval.

This effect is illustrated in Fig. 7 (a) and (b), which shows the contribution from process I and II, respectively, when the pulse duration is equal to $T_R$ in the case of the $1s^2 \rightarrow 1s2p$ resonant transition in He. Since $W$ increases with the detuning, the effective Rabi period becomes shorter, which explains why the doublet is visible for large detunings in Fig. 7 (a).

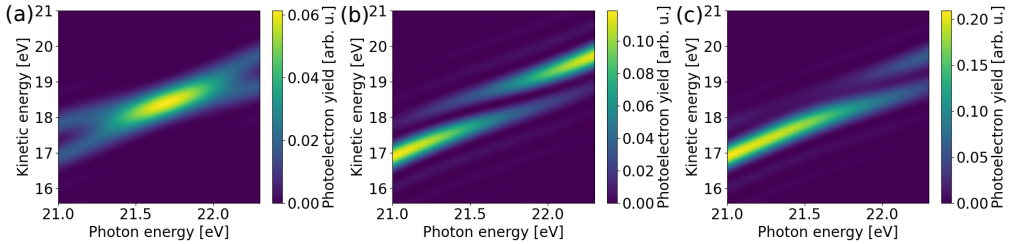


**Figure 7:** Contribution from $\alpha_\epsilon^{(1)}(t)$ (a) and $\alpha_\epsilon^{(2)}(t)$ (b) to ionizataion via $1s2p$ in He, when the pulse duration is $T_R$. The total photoelectron spectrum is shown in (c).

Figure 7 (c) shows the effect of the interference of the two ionization pathways, with a suppression of the upper component of the doublet near the resonance frequency. The intensity used in Fig. 7 is $1.1 \times 10^{14}$ W/cm$^2$, which is where the ionization rates for the two processes are nearly equal.

Wollenhaupt et al. showed how the doublet can be modified by using a pump-probe scheme where the atom first interacts with a pulse that has an area of $\pi/2 + N\pi$, and then with a second pulse that has a variable time delay relative to the first [59]. Depending on the delay, the upper, lower, or both components of the AT doublet will display interference fringes, as illustrated in Fig. 8 for the case of two pulses, each with an area of $7.5\pi$.

# 4 Hilbert space partitioning, resolvent operators and effective Hamiltonians for resonant photoionization

This section explains how the partitioning of the Hilbert space together with the use of resolvent operators leads to a description of the dynamics in a subspace in terms of an effective-Hamiltonian for uncoupled atom-field states. The idea behind the approach is to accurately describe a strongly interacting subspace of the full system, while the coupling to the remaining part of the system is assumed to be sufficiently weak, so that it can be treated perturbatively. The methods described here were applied in paper III, where it was used to study a stabilization mechanism in resonant two-photon ionization that was first suggested by Beers and Armstrong [11]. Cohen-Tannoudji, Dupont-Roc and Grynberg present a general introduction to the resolvent method in Ref. [60], and it's application to resonant photoionization has been studied by e.g. Beers and Armstrong [11] and Holt, Raymer and Reinhardt [13]. Here we are interested in applying this framework to experiments performed at modern (seeded) FEL facilities that operate at high intensities with XUV radiation [2]. Recently, control of ionization using chirped pulses has been proposed by Saalmann et al. [15], which can be related to the work of Beers and Armstrong in the adiabatic limit.

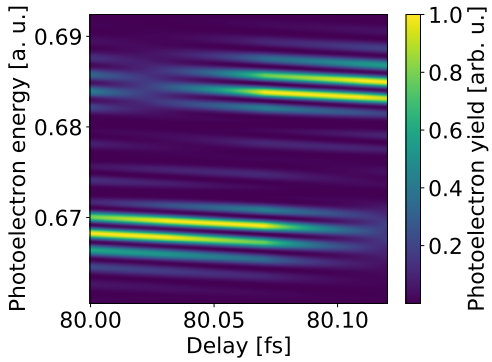


**Figure 8:** Photoelectron spectrum as a function of the delay between two $7.5\pi$ pulses, computed using the first order amplitude $\alpha_\epsilon^{(1)}(t)$. The photoelectron spectrum has been normalized for each delay.

Examples of other contexts where effective Hamiltonians are used includes the description of auto-ionizing resonances [61, 62] and Rayleigh-Schrödinger perturbation theory for (nearly) degenerate states [37]. However, in this thesis we will focus on resonant photoionization and use the resolvent operator method to systematically explore interference effects that originate from coupling out from the subspace, due to different physical processes.

## 4.1 $P + Q = 1$: part two

Like in Sec. 3, we want to separate out the strongly interacting or resonant states of the system, and treat the rest perturbatively. In the application to resonant two-photon ionization, a natural partitioning is to include the two resonant bound states $|a\rangle = |\phi_a, N\rangle$ and $|b\rangle = |\phi_b, N-1\rangle$ in $\mathcal{P}$. Beers and Armstrong also includes in $\mathcal{P}$ the set of continuum states $|\phi_\epsilon, N-2\rangle$ that can be reached from the ground state by absorbing two photons [11]. However, since they also make the pole approximation (to be discussed in the next section) when computing the amplitudes of the bound states, the result is equivalent to what one gets from including only the two resonant bound states in $\mathcal{P}$, see App. 1.

## 4.2 Effective Hamiltonians

In order to describe the time evolution of a system with a time independent Hamiltonian, we will make use of the resolvent operator $G(z)$. The resolvent of $H = H_0 + V$ satisfies the equation

$$(z - H)G(z) = 1, \tag{86}$$

whenever $z$ is in the resolvent set of $H$, i.e. $z$ is not in the spectrum of $H$. The resolvent is related to the Fourier and Laplace transforms of the time evolution operator [60, 63].

For $t > 0$, the matrix elements of the resolvent can be used to compute time-dependent transition amplitudes via the formula [60]

$$U_{fi}(t) = \lim_{\eta \to 0^+} -\frac{1}{2\pi i} \int_{-\infty}^{\infty} \mathrm{d}E e^{-i(E+i\eta)t} G_{fi}(E + i\eta), \tag{87}$$

where $U_{fi}(t)$ is the probability amplitude to transition from state $|i\rangle$ to state $|f\rangle$.

By acting on both sides of Eq. (86) with $P$ from the right and with $P$ and $Q$ from the left, and additionally inserting $P + Q = 1$ we get

$$P(z - H)PG(z)P + P(z - H)QG(z)P = P \tag{88a}$$
$$Q(z - H)PG(z)P + Q(z - H)QG(z)P = 0. \tag{88b}$$

Using the fact that $P$ and $Q$ commute with $H_0$, and that $PH_0Q = QH_0P = 0$, this can be rewritten as

$$P(z - H)PG(z)P - PVQG(z)P = P \tag{89a}$$
$$-QVPG(z)P + Q(z - H)QG(z)P = 0. \tag{89b}$$

Formally we can use the second equation to eliminate $QG(z)P$ from the first, to get.

$$P(z - H)PG(z)P - PVQ\frac{1}{Q(z - H)Q}QVPG(z)P = P \tag{90a}$$
$$QG(z)P = \frac{1}{Q(z - H)Q}QVPG(z)P. \tag{90b}$$

The first equation can now be written in terms of $H_0$ and $V$,

$$P(z - H_0)PG(z)P - P\left(V + VQ\frac{1}{Q(z - H_0 - V)Q}QV\right)PG(z)P = P, \tag{91}$$

and we can introduce the level-shift operator

$$R(z) = V + VQ\frac{1}{Q(z - H_0 - V)Q}QV. \tag{92}$$

We can now write the equation for $PG(z)P$ in terms of the level-shift operator

$$(z - H_0)PG(z)P - PR(z)PPG(z)P = P. \tag{93}$$

We see now that this can be written

$$(z - H_{\text{eff}}(z))PG(z)P = P, \tag{94}$$

where the effective Hamiltonian

$$H_{\text{eff}}(z) = PH_0P + PR(z)P, \tag{95}$$

has been introduced.

In order to get expressions that are more manageable, two approximations to the level-shift operator will be made. The first one is to expand $PR(z)P$ in powers of the interaction $V$ and truncating the resulting power series at a finite order. This limits the kinds of processes that are included in our description of the dynamics, but those that are included are in a sense included to infinite order.

The expansion looks like

$$\begin{aligned} PR(z)P &= PVP + PVQ\frac{1}{Q(z-H_0-V)Q}QVP \\ &= PVP + PVQ\frac{1}{Q(z-H_0)Q}QVP \\ &+ PVQ\frac{1}{Q(z-H_0)Q}QVQ\frac{1}{Q(z-H_0)Q}QVP + \dots \end{aligned} \tag{96}$$

and should be carried out to the order that will generate the kinds of processes that you want to include in the effective description of the system. For the case of resonant photoionization that was studied in paper III, an expansion up to fourth order in $V$ is required to include the effect of the non-resonant ionization pathway on the time-dependent amplitudes of the states in $\mathcal{P}$ [13].

The second approximation we will make is the so-called *pole-approximation* (or Wigner-Weisskopf approximation), where the $z$ dependence of $R(z)$ is neglected and its matrix elements are evaluated at $z = E_{\text{res}} + i\eta$, with $\eta \to 0^+$. $E_{\text{res}}$ is taken as the average energy of the two states in $\mathcal{P}$ [64]. This approximation amounts to neglecting the contribution of singularities of $G(z)$ that comes from states in $\mathcal{Q}$, i.e. other bound state or resonance poles and the branch-cut related to the continuum. Including the contribution of the branch-cut typically leads to corrections to exponential decay at short and long times [60, 65], while contributions from other poles would lead to more oscillating terms in the amplitudes and corrections to the locations of the already included poles [64]. For this approximation to be valid, the matrix elements of $R(z)$ should be slowly varying functions of $z$ near $E_{\text{res}}$, which holds true sufficiently close to the resonance and for sufficiently small coupling strengths.

With these approximations the effective Hamiltonian takes the form

$$H_{\text{eff}} = \begin{bmatrix} h_{aa} & h_{ab} \\ h_{ba} & h_{bb} \end{bmatrix}, \tag{97}$$

where the matrix elements are in general complex. The off-diagonal elements satisfy $h_{ab} = h_{ba}$, so that $H_{\text{eff}}$ is complex symmetric $H_{\text{eff}}^T = H_{\text{eff}}$ [13]. As was done by Holt et al. [13], it is useful to write the diagonal elements in terms of bare energies $E_i$, Stark shifts $\delta_i$ and ionization rates $\gamma_i$, and the off-diagonal in terms of a Rabi frequency $\Omega$ with a contribution from an imaginary part $\beta$. $H_{\text{eff}}$ will then be

$$H_{\text{eff}} = \begin{bmatrix} E_a + \delta_a - i\frac{\gamma_a}{2} & \frac{\Omega+i\beta}{2} \\ \frac{\Omega+i\beta}{2} & E_b + \delta_b - i\frac{\gamma_b}{2} \end{bmatrix}. \tag{98}$$

Examples of leading order processes that contribute to the different parameters for $|a\rangle$ is given in Fig. 9. $\gamma_a$ appears from a fourth order process, since two photons have to be absorbed from $|a\rangle$ to ionize. $\gamma_b$ would get a contribution from a process similar to that of $\delta_a$, since only one photon has to be absorbed to reach the continuum from $|b\rangle$. The third order diagram, which gives a contribution to $\beta$, represents a process where the electron reaches the continuum by absorption of two photons from $|a\rangle$, and then emits one photon to reach $|b\rangle$ [13] (or equivalently absorbing one photon from $|b\rangle$ and then emitting two to reach $|a\rangle$). This represents the interference between the resonant and non-resonant ionization processes that were introduced in Sec. 3.3, and it plays an important role for the stabilization of dressed atoms explored in paper III.

#### Intensity scaling factors

Since the different orders of the perturbative expansion of $H_{\text{eff}}$, depend on a different power of the electric field strength, it is useful to separate out the field dependence from the factor that comes from the atomic structure. In particular, we can write the matrix elements of $R$ in the following form

$$R_{ij} = \sum_{n=1}^{\infty} \frac{E_0^n}{2^n} \rho_{ij}^{(n)}, \tag{99}$$

where the scaling factors $\rho_{ij}^{(n)}$ depend on only on the atomic structure. These quantities were calculated up to order $n = 4$ in paper III for hydrogen and helium (CIS), and are given in Tab. 2.

### 4.3 Matrix elements involving the continuum

In the computation of the matrix elements of $H_{\text{eff}}$ it is necessary to evaluate matrix elements involving continuum states, when the matrix elements involve poles at energies that lie above the ionization threshold. This requires the enforcement of the correct boundary conditions on the intermediate perturbed wavefunctions, which can be done with methods such as complex scaling, complex absorbing potentials, and extrapolation, described below.

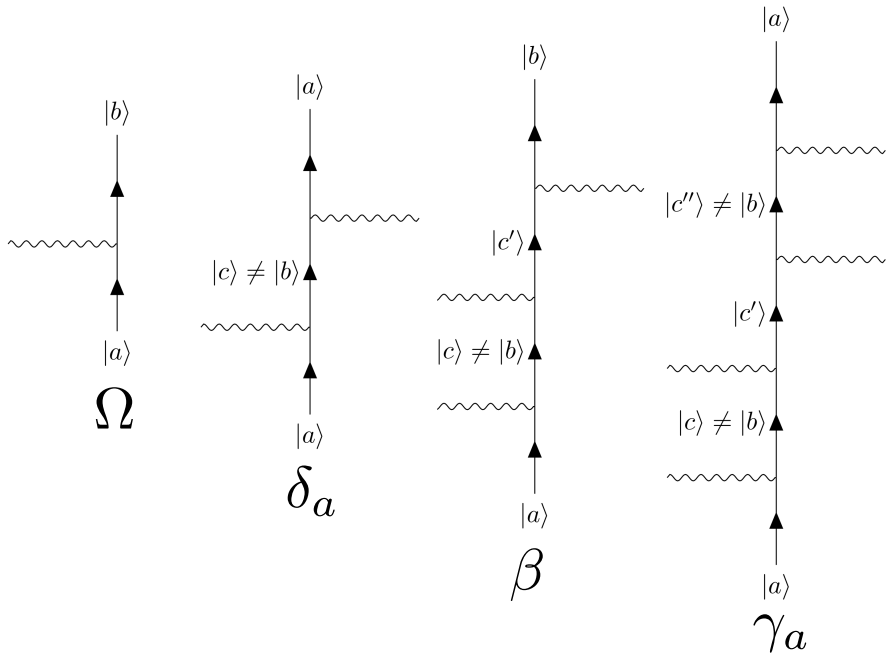


**Figure 9:** Perturbative processes that are part of the leading order contributions to $\Omega$, $\delta_a$, $\beta$, $\gamma_a$. Absorption/emission of a photon is indicated by a wavy line on the left/right side of the diagrams. $|c\rangle$, $|c'\rangle$ and $|c''\rangle$ represents a sum over intermediate states, and stages where the other resonant state $|b\rangle$ has to be excluded are indicated by $\neq |b\rangle$. The figure is adapted from Fig. 1 (b) of paper [III] under a CC BY 4.0 license.

**Table 2:** The level-shift scaling factors for hydrogen: $1s - 2p$, and helium: $1s^2 - 1s2p$, with linear polarization (L) and circular polarization (C). The number in parentheses indicate the power of ten, and atomic units are used for all quantities.

| $\rho_{ij}^{(n)}$ | Atom/Pol. | $n=1$ | $n=2$ | $n=3$ | $n=4$ |
|---|---|---|---|---|---|
| $aa$ | H/L | 0 | $-4.299$ | 0 | $1452 - 233.1i$ |
| $ab$ | H/L | 0.7449 | 0 | $54.26 + 9.322i$ | 0 |
| $ba$ | H/L | 0.7449 | 0 | $54.26 + 9.322i$ | 0 |
| $bb$ | H/L | 0 | $11.70 - 0.5223i$ | 0 | $2888 - 95.57i$ |
| $aa$ | H/C | 0 | $-4.299$ | 0 | $1180 - 337.4i$ |
| $ab$ | H/C | $-0.7449$ | 0 | $-26.93 - 15.12i$ | 0 |
| $ba$ | H/C | $-0.7449$ | 0 | $-26.93 - 15.12i$ | 0 |
| $bb$ | H/C | 0 | $12.42 - 0.6776i$ | 0 | $2378 - 47.25i$ |
| $aa$ | He/L | 0 | $-2.853$ | 0 | $155.6 - 10.32i$ |
| $ab$ | He/L | 0.4040 | 0 | $8.533 + 0.2326i$ | 0 |
| $ba$ | He/L | 0.4040 | 0 | $8.533 + 0.2326i$ | 0 |
| $bb$ | He/L | 0 | $2.010 - 7.871i(-3)$ | 0 | $120.0 - 0.2154i$ |
| $aa$ | He/C | 0 | $-2.853$ | 0 | $126.6 - 15.25i$ |
| $ab$ | He/C | $-0.4040$ | 0 | $-5.149 - 0.3737i$ | 0 |
| $ba$ | He/C | $-0.4040$ | 0 | $-5.149 - 0.3737i$ | 0 |
| $bb$ | He/C | 0 | $1.971 - 9.159i(-3)$ | 0 | $85.35 - 1.831i(-3)$ |

### Complex scaling

Complex scaling of the radial coordinate was originally developed to study resonances [66, 67], since it can transform a resonance wavefunction that diverges in the radial coordinate into a square integrable function [67]. It can also be used in the computation of ionization rates using Floquet theory [42, 68]. In time-dependent simulations complex scaling can be used to absorb outgoing particles [69, 70], but the method can not be applied in time-dependent problems if the length gauge form of the interaction Hamiltonian is used [69, 70].

Complex scaling was originally introduced by scaling the radial coordinate over the whole space, i.e. the transformation has the following form

$$R(r) = re^{i\theta}. \tag{100}$$

The radial derivative now takes the form

$$\frac{\partial}{\partial R} = e^{-i\theta}\frac{\partial}{\partial r}. \tag{101}$$

The complex scaled radial Hamiltonian

$$H_r(\theta) = \frac{1}{2}e^{-2i\theta}\frac{\mathrm{d}^2}{\mathrm{d}r^2} + V(e^{i\theta}r), \tag{102}$$

will no longer be Hermitian, but is instead complex symmetric. The non-Hermitian nature of $H_r(\theta)$ means that its eigenfunctions are no longer orthogonal in the standard inner product

$$\langle\phi_a|\phi_b\rangle \neq \delta_{ab}, \tag{103}$$

but one instead has the relation [67]

$$\langle\phi_a^*|\phi_b\rangle = (\phi_a|\phi_b) = \delta_{ab}. \tag{104}$$

An alternative to scaling the radial coordinate over the whole space is exterior complex scaling (ECS), where only the part outside of some radius $R_0$ is transformed:

$$R(r) = \begin{cases} r & 0 \leq r \leq R_0 \\ R_0 + (r - R_0)e^{i\theta} & r > R_0. \end{cases} \tag{105}$$

This is useful in cases where the Hamiltonian is not everywhere well-behaved under the scaling transformation [66], or one wishes to use it to absorb outgoing particles but not affect the wavefunction inside a certain region [70].

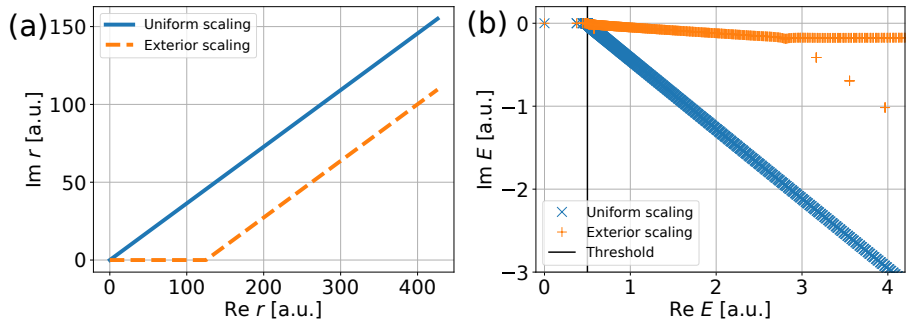


**Figure 10:** (a) Complex scaled radial coordinate for uniform (solid blue line) and exterior scaling (dashed orange line). The exterior region starts at $r = 125$ a.u., and the scaling angle is $\theta = 20°$. (b) Energies of hydrogen atom using the complex scalings from (a). The solid vertical line at $\mathrm{Re}\, E = 0.5$ a.u. indicates the ionization threshold.

With these methods the eigenvalues of the bound part of the spectrum is unaffected, while continuum states have their energies rotated into the complex plane by the angle $-2\theta$, except for resonances which above certain threshold angles have the energies $E(\theta) = E_{res} - i\Gamma/2$, where $\Gamma$ is the decay rate of the resonance. An example of uniform and exterior scaling of the radial coordinate is shown in Fig. 10 (a), with the exterior region starting at $R_0 = 125$ a.u. and $\theta = 20°$. The energies of a hydrogen atom evaluated on a B-spline grid with the corresponding scaling is presented in Fig. 10 (b). In the case of uniform scaling, the continuum states are all rotated into the complex plane by $-2\theta$. For the case of exterior scaling most of the states are not rotated by the full $-2\theta$ and there is a bifurcation, as is typical for numerical implementations of ECS [71].

### Complex absorbing potentials

A closely related technique to ECS are complex absorbing potentials (CAPs), which are often used in time dependent simulations to reduce reflections of photoelectrons due to a finite simulation box [72], but can also be used in time independent calculations to enforce outgoing boundary conditions [73–75]. As the name suggests, a complex valued potential is introduced at large distances to absorb outgoing particles before they hit the boundary of the simulation box. Similar to complex scaling, the Hamiltonian will be complex symmetric rather than Hermitian if a CAP is used.

An example of a CAP is the following [73]

$$V_{\mathrm{CAP}}(r) = -i\xi\theta(r - R_0)(r - R_0)^2, \tag{106}$$

where $\xi$ is a parameter that controls the strength of the CAP, and $\theta(x)$ is the Heaviside function, which ensures that the CAP only has an effect outside the radius $R_0$.

**Extrapolation method for continuum transitions**

The extrapolation method of Cormier and Lambropoulos can be used to calculate matrix elements involving continuum transitions [76]. The the two-photon dipole-matrix element involved in the calculation of the above-threshold ionization amplitude to reach the final state $|f\rangle$ starting from some initial state $|i\rangle$, with an intermediate energy that lies in the continuum is formally

$$M_{fi} = \lim_{\eta \to 0^+} \sum\!\!\!\!\!\!\int_n \frac{\langle f| z |n\rangle\langle n| z |i\rangle}{E_i + \omega + i\eta - E_n}. \tag{107}$$

When $E_i + \omega$ lies above the ionization threshold of the atom, then the Sokhotski–Plemelj theorem can be used to write the matrix element as

$$M_{fi} = \text{p. v.} \sum\!\!\!\!\!\!\int_n \frac{\langle f| z |n\rangle\langle n| z |i\rangle}{E_i + \omega - E_n} - i\pi \sum_\ell \langle f| z |\ell\rangle\langle \ell| z |i\rangle\,, \tag{108}$$

where p. v. denotes the Cauchy-principal value and $|\ell\rangle$ are all the continuum states with the resonant energy $E_i + \omega$.

When using a discrete representation of the problem, the sum-integral is approximated with a sum over the bound-states and the pseudo-continuum states

$$M_{fi}(\eta) = \sum_n \frac{\langle f| z |n\rangle\langle n| z |i\rangle}{E_i + \omega + i\eta - E_n}. \tag{109}$$

For different discretizations, $M_{fi}(\eta)$ will typically not converge to the same value in the limit $\eta \to 0^+$, and it will start to diverge as the energy spacing in the pseudo-continuum becomes smaller since the distance between $E_i + \omega$ and the nearest pseudo-continuum state shrinks. However, it was shown by Cormier and Lambropoulos in Ref. [76] that $M_{fi}$ can be calculated by *extrapolation*. They suggest that $M_{fi}(\eta)$ is calculated for a few values of $\eta$ chosen such that they are all larger than approximately 3-4 times the spacing $\delta$ of pseudo-continuum states near the pole. A rational interpolating function $q(\eta)$ is then fitted to the values of $M_{fi}(\eta)$. The extrapolation step is performed by evaluating $q(\eta)$ at $\eta = 0$, i.e. $M_{fi}$ is approximated by $q(0)$.

The reason for choosing a rational interpolating function is that they can perform better than polynomial interpolants when used for extrapolation. This is especially true when the function that is to be approximated has singularities in the complex plane, since a rational function will in general have poles that can be used to approximate the location of the singularities of the function under consideration [77]. The theory of rational interpolation is closely related to Padé approximants [78], and an extrapolation using Padé approximants

can be used together with CAPs to compute the location of resonances [74], which is similar in spirit to the Cormier and Lambropoulus method.

A comparison between radial dipole matrix elements computed with the extrapolation method using quadratic and rational interpolating functions is made in Tab. 3 and Fig. 11 for the ATI transition in Path 1 of paper IV. In this case the rational interpolation was performed using Thiele interpolation [78]. As can be seen in Tab. 3, the values extracted from the rational interpolating function are less sensitive to the size of the radial grid $r_{\max}$ than those computed with quadratic interpolation.

**Table 3:** Comparison of radial dipole matrix elements computed with the extrapolation method using quadratic and rational interpolation for different radial grids.The transition is shown in Fig. 11 (a)

| Interpolation | $r_{\max}$ [a.u.] | Real part [a.u.] | Imaginary part [a.u.] |
|---|---|---|---|
| Quadratic | 300 | $-71.053$ | $-262.44$ |
| Rational | 300 | $-112.36$ | $-145.76$ |
| Quadratic | 600 | $-134.56$ | $-169.46$ |
| Rational | 600 | $-112.34$ | $-145.45$ |
| Quadratic | 900 | $-123.13$ | $-149.31$ |
| Rational | 900 | $-112.32$ | $-145.44$ |

### R-matrix

Another approach to enforcing boundary conditions, which has not been used in this thesis, is the use of the R-matrix procedure. Here the configuration space is divided up into an inner and outer region, and a Bloch operator is introduced to enforce consistency between the two regions. The outer region is typically chosen such that asymptotic forms of the wavefunctions are valid, which are then matched to solutions in the inner region. This approach has for example been employed to compute matrix elements for ATI transitions in many-electron atomic and molecular systems for the process of single electron ionization [79].

### Computing projected resolvents

In the intermediate steps of computing the matrix elements of $H_{\text{eff}}$ it is necessary to compute perturbed wavefunctions that have the following form

$$|\rho_{m+1}\rangle = \sum\!\!\!\!\!\!\int_{n\neq a,b} \frac{|n\rangle\langle n|\, z\, |\rho_m\rangle}{w - E_n}, \tag{110}$$

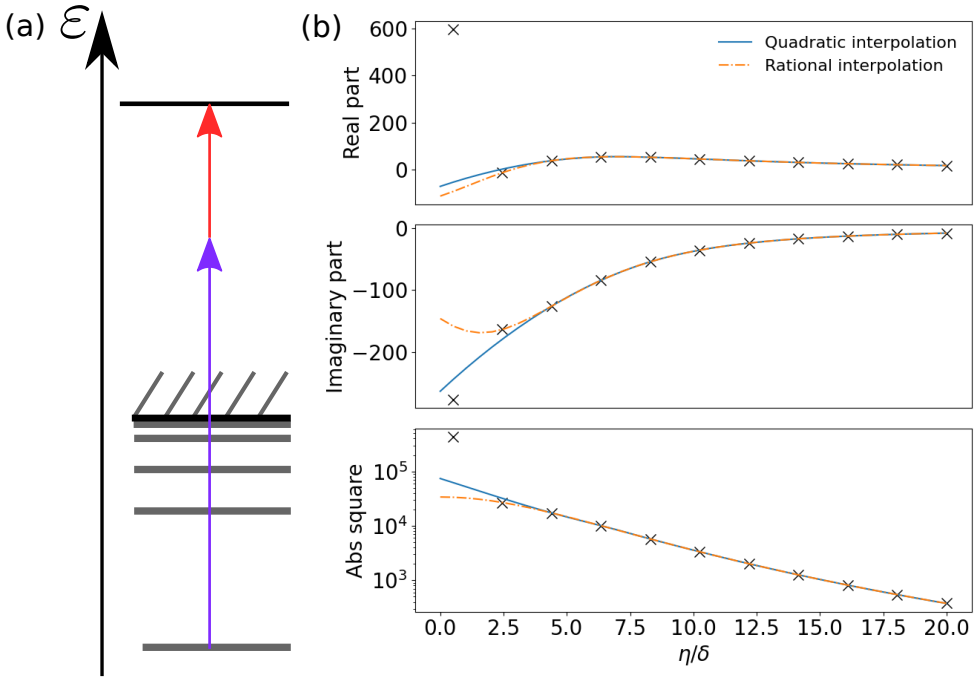


**Figure 11:** (a)The ATI path that is considered in Tab. 3 and in (b). (b) Comparison between extrapolation with rational and quadratic functions in the extrapolation method, $r_{\max} = 300$ a.u. The crosses mark the datapoints used to construct the interpolating functions. Points with $\eta/\delta < 4$ were not included in the interpolation procedure.

where $w = E_{a,b} + M\omega$, $M \in \mathbb{N}$. Instead of computing this by direct summation, it is possible to reformulate it as the solution of a linear system, i.e.

$$Q(w - H_0)Q\,|\rho_{m+1}\rangle = Qz\,|\rho_m\rangle\,, \tag{111}$$

or equivalently

$$(w - H_0)\,|\rho_{m+1}\rangle = Qz\,|\rho_m\rangle\,, \tag{112}$$

since $|\rho_{m+1}\rangle \in \mathcal{Q}$.

The resulting system matrix is in principle singular, but a minimum norm solution can be found using a preconditioned version of the generalized minimal residuals method (GMRES)[80], since the system is consistent [81] (the right-hand side is in the range of $Q(w - H_0)Q$). Using an iterative method such as GMRES means that it is not necessary to explicitly form the projected forms of the matrices, since only the effect of matrix vector products by the system matrix is needed. This also avoids the need to compute a minimum norm solution by explicitly forming a pseudoinverse [82].

### 4.4 Dressed states of $H_{\text{eff}}$

The eigenstates of the effective Hamiltonian are the dressed states $|+\rangle$ and $|-\rangle$. They have associated eigenvalues $\lambda_\pm$ that will be complex, since $H_{\text{eff}}$ is not Hermitian. The non-Hermitian nature of $H_{\text{eff}}$ also means that the dressed states are not orthogonal in the standard inner product, i.e. $\langle +|-\rangle \neq 0$ [13]. Since they are eigenstates of $H_{\text{eff}}$, the dressed states form a useful basis to describe the dynamics of the effective two-level system.

The eigenvalues $\lambda_\pm$ take the form

$$\lambda_\pm = \frac{h_{aa} + h_{bb}}{2} \pm \frac{1}{2}\sqrt{(h_{aa} - h_{bb})^2 + 4h_{ab}^2}, \tag{113}$$

or expressed in terms of the Holt parameters [13]

$$\lambda_\pm = \frac{E_a + \delta_a + E_b + \delta_b}{2} - i\frac{\gamma_a + \gamma_b}{4} \pm \frac{1}{2}\sqrt{\left(\Delta\widetilde{\omega} - i\frac{\gamma_a - \gamma_b}{2}\right)^2 + (\Omega + i\beta)^2}, \tag{114}$$

where $\Delta\widetilde{\omega} = E_a + \delta_a - E_b - \delta_b$ is the detuning when including the Stark-shifts $\delta_a$ and $\delta_b$. The eigenvalues are split by a complex Rabi frequency,

$$\widetilde{W} = \sqrt{(h_{aa} - h_{bb})^2 + 4h_{ab}^2} = \sqrt{\left(\Delta\widetilde{\omega} - i\frac{\gamma_a - \gamma_b}{2}\right)^2 + (\Omega + i\beta)^2}, \tag{115}$$

which in the limit where the effective parameters of $H_{\text{eff}}$ go to zero corresponds to the usual generalized Rabi frequency $W$. The imaginary part of $\lambda_\pm$ gives the ionization rates of the dressed states, $\gamma_\pm = -2\,\mathrm{Im}\,\lambda_\pm$. Since in general $\mathrm{Im}\,\widetilde{W} \neq 0$, one of the dressed states will have an enhanced ionization rate, while the ionization rate of the other one will be suppressed. Which of the dressed states that ionizes faster or slower will depend on the sign of $\mathrm{Im}\,\widetilde{W}$, for details see Appendix B of paper III. The real part of $\widetilde{W}$ will give the AT-splitting and the frequency of the damped Rabi oscillations.

In terms of the dressed states, the projection of the time-dependent wavefunction onto $\mathcal{P}$ is given by

$$P\,|\psi(t)\rangle = c_a(t)\,|a\rangle + c_b(t)\,|b\rangle = c_+ e^{-i\lambda_+ t}\,|+\rangle + c_- e^{-i\lambda_- t}\,|-\rangle\,, \tag{116}$$

where $c_+$ and $c_-$ are the expansion coefficients of $|a\rangle$ in the dressed state basis. The time-dependent population is given by

$$\begin{aligned} P(t) = |c_a(t)|^2 + |c_b(t)|^2 &= |c_+|^2 e^{-\gamma_+ t} + |c_-|^2 e^{-\gamma_- t} \\ &+ 2e^{-\frac{\gamma_+ + \gamma_-}{2}t}\mathrm{Re}[c_+ c_-^* e^{-i\,\mathrm{Re}\,\widetilde{W}t}\,\langle -|+\rangle]. \end{aligned} \tag{117}$$

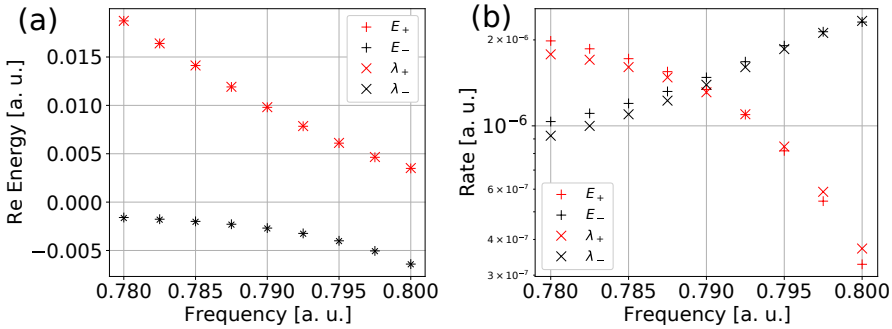


**Figure 12:** Comparison of eigenvalues of $H_{\text{eff}}$ ($\lambda_\pm$, marked by crosses) with Floquet quasi energies ($E_\pm$, marked by $+$ signs ) for different $\omega$ around the field free resonance $\omega_{ba}$ at a field strength of $E_0 = 0.024$ a.u. (a) contains the real part of the energies, and (b) the corresponding ioinzation rates.

In Figs. 12 and 13, a comparison is made between quasienergies calculated from Floquet theory and the fourth order $H_{\text{eff}}$ for He interacting with linearly polarized light. The chosen Floquet energies $E_\pm$, are those whose corresponding states that have large overlap with the $|\phi_a, 0\rangle$ and $|\phi_b, -1\rangle$ states in the extended Hilbert space. As is clear from the real part of the energies, the eigenvalues separate into two branches, with the upper one (corresponding to $\lambda_+$) plotted in red and the lower one (corresponding to $\lambda_-$) in black. The agreement between $E_\pm$ and $\lambda\pm$ is slightly better in Fig. 13. The reason for this is that the scaling factors in Fig. 12 were computed at the resonance frequency, and therefore the slight variation of the dipole matrix elements with frequency is not fully reflected in the energies from $H_{\text{eff}}$. We find that this mainly affects the ionization rates. The difference in ionization rates between the dressed states that was mentioned above is visible in Fig. 13 for both the Floquet energies and the energies from $H_{\text{eff}}$. This point will be further discussed in Sec. 6.2, and it is crucial to the prediction of stabilization of paper III.

## 4.5 Transitions to $\mathcal{Q}$

So far we have concerned ourselves with the effective dynamics in subspace $\mathcal{P}$, for which $H_{\text{eff}}$ was used. However, in paper III the observable of interest was the photoelectron spectrum, which necessitates a computation of the probability amplitudes of the photoelectron continuum states. However, these states lie in $\mathcal{Q}$, where it is not possible to use only $H_{\text{eff}}$ to describe the dynamics. Instead, we will make use of Eq. (90b) together with the fact that we have already calculated an approximation for $PG(z)P$ by using $H_{\text{eff}}$. Since Eq. (90b) still contains the full $H$ we will make a perturbative expansion of the projected resolvent $\frac{1}{Q(z-H)Q}$ in powers of $V$. This is consistent with our perturbative treatment of $V$ in the construction of $H_{\text{eff}}$.

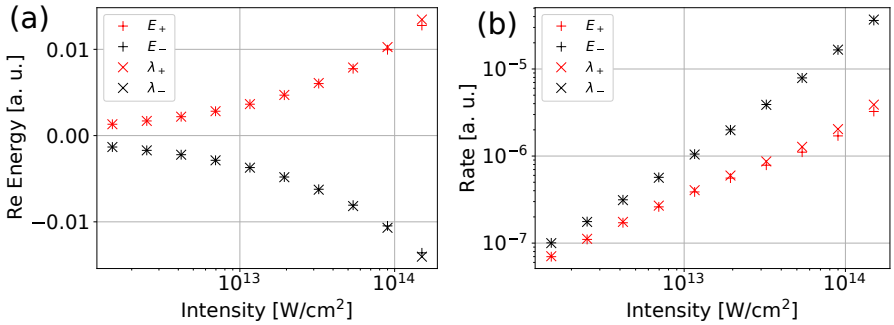


**Figure 13:** Comparison of eigenvalues of $H_{\text{eff}}$ ($\lambda_\pm$) with Floquet quasi energies ($E_\pm$) for different intensities, and fixed $\omega = \omega_{ba}$. (a) contains the real part of the energies, and (b) the corresponding ioinzation rates.

The perturbative expansion for $QG(z)P$ in powers of $V$ has the following form

$$QG(z)P = \frac{1}{Q(z-H_0-V)Q}QVPPG(z)P = \frac{1}{Q(z-H_0)Q}QVPPG(z)P + \frac{1}{Q(z-H_0)Q}QVQ\frac{1}{Q(z-H_0)Q}QVPPG(z)P + \dots \tag{118}$$

For paper III we kept terms up to second order in $V$. This can then be used to compute the matrix element $G_{\epsilon a}(z)$ between the initial state $|\phi_a, N\rangle$ and a continuum state $|\phi_\epsilon, N-2\rangle$, which through Eq. (87) can be used to calculate the ionization amplitude.

In terms of the energies of the dressed states, the first and second order contributions to the photoionization amplitudes are given by

$$U^{(1)}_{\epsilon a\pm}(t) = \mp iE_0 z_{\epsilon b}\frac{h_{ab}}{W}\exp[-i\frac{t}{2}(E_\epsilon+\lambda_\pm)]\frac{\sin[\frac{t}{2}(E_\epsilon-\lambda_\pm)]}{(E_\epsilon-\lambda_\pm)}, \tag{119a}$$

$$U^{(2)}_{\epsilon a\pm}(t) = \mp iE_0^2 z_{\epsilon\neq b}\frac{(\lambda_\pm-h_{bb})}{2W}\exp[-i\frac{t}{2}(E_\epsilon+\lambda_\pm)]\frac{\sin[\frac{t}{2}(E_\epsilon-\lambda_\pm)]}{(E_\epsilon-\lambda_\pm)}, \tag{119b}$$

where $\pm$ indicates from which dressed state the contribution is coming from. The total first and second order amplitudes are then given by

$$U^{(1)}_{\epsilon a}(t) = U^{(1)}_{\epsilon a+}(t) + U^{(1)}_{\epsilon a-}(t), \tag{120a}$$

$$U^{(2)}_{\epsilon a}(t) = U^{(2)}_{\epsilon a+}(t) + U^{(2)}_{\epsilon a-}(t), \tag{120b}$$

where the following notation for the atomic dipole contributions has been introduced

$$z_{\epsilon b} = \langle\psi_\epsilon|\, z\,|\psi_b\rangle\,, \tag{121a}$$

$$z_{\epsilon\neq b} = \sum_{c\neq b}\frac{\langle\psi_\epsilon|\, z\,|\psi_c\rangle\,\langle\psi_c|\, z\,|\psi_a\rangle}{E_a-E_c}. \tag{121b}$$

The amplitudes give rise to a spectrum that has two main peaks that are separated by $\mathrm{Re}\,\widetilde{W}$, i.e. the AT-Knight doublet [12]. As discussed in paper III, there will also be smaller peaks between the main peaks of the AT doublet that are related to the number of Rabi-cycles that the atom performs [18], and peaks outside the doublet that are related to the square nature of the pulse that has been assumed in the derivation of these results. Since $\lambda_\pm$ has a nonzero imaginary part, the photoelectron spectrum will in the long time limit (i.e. when the atom is close to fully depleted) look like two Lorentzian peaks with a slight difference in width due to $\mathrm{Im}\,\lambda_\pm$ being different for the two-dressed states in general. This difference in width of the two components of the AT doublet has been seen in TDSE calculations in hydrogen for intense fields and linear polarization [46, 47].

The values for $z_{\epsilon b}$ and $z_{\epsilon\neq b}$ for helium (CIS) used in paper III for linear and circular polarization are given in Tab. 4. When comparing the relative strength of the two matrix elements, $z_{\epsilon\neq b}$ should be multiplied by an extra power of $E_0/2$ since it stems from a higher order process than $z_{\epsilon b}$. The difference in relative strength between $z_{\epsilon b}$ and $z_{\epsilon\neq b}$ for $s$- and $d$-waves is responsible for the fact that the relative stabilization of one of the dressed states is not as pronounced in the case of linear polarization as for circular polarization. This is because the interference between resonant and non-resonant ionization is not maximal for both partial waves simultaneously. The situation is different for circular polarization since, when starting in the ground state of helium, only ionization to $d$-waves is allowed in two-photon ionization. In other words, there are two continua accessible in the linearly polarized case, but only one continuum for circular polarization.

**Table 4:** Dipole matrix elements needed to compute ionization amplitudes for resonant ionization in He ($1s^2$-$1s2p$).

| Polarization | Matrix element | $s$-wave | $d$-wave |
|---|---|---|---|
| Linear | $z_{\epsilon b}$ | 0.0233 | 0.04426 |
| Linear | $z_{\epsilon\neq b}$ | 0.2207 | −1.805 |
| Circular | $2^{-1/2}(x+iy)_{\epsilon b}$ | 0 | −0.05421 |
| Circular | $2^{-1/2}(x+iy)_{\epsilon\neq b}$ | 0 | −2.210 |

# 5 Frustrated tunneling ionization

Here we will make a departure from the world of few-photon resonant ionization with photon energies in the XUV range, and instead shift our focus to what happens when an atom interacts with a strong IR-field, where few photon ionization is no longer possible. This is the regime of HHG [19, 26], ATI [22, 23] and FTI [28]. The latter will be the focus of this section of the thesis. The physical processes that are important in this regime are tunneling ionization, and laser driven quasiclassical continuum dynamics, such as recollision and rescattering [83].

At the high intensities and long wavelengths that will be considered here the electric field of the laser can no longer be considered as a weak perturbation on top of the atomic potential, and it is in certain cases useful to treat the laser-atom interaction exactly, while neglecting or using some kind of perturbation theory for the atomic potential. Another important point is that typically the RWA breaks down for these kinds of laser-fields, and the instantaneous electric-field amplitude will be important, leading to quasiclassical dynamics that happen on timescale shorter than a laser cycle (sub-cycle dynamics).

## 5.1 Tunneling ionization and the strong-field approximation

Here follows a brief overview of the SFA and its application to tunneling ionization, which was adapted in Ref. [27] to study FTI. One of the useful aspects of the SFA comes from the possibility of performing the saddle point approximation on the resulting integral for the ionization amplitude. This naturally leads to the tunneling picture, when one is required to move into the complex time plane to solve the saddle point equations with quasiclassical physical interpretation.

The starting point for the SFA is the Dyson equation for the time-evolution operator corresponding to the full Hamiltonian $H(t) = H_0 + V(t)$, where $H_0$ is the field free atomic Hamiltonian, and $V(t)$ is the time-dependent laser-atom coupling. The time-domain Dyson equation is then given by

$$U(t, t_0) = U_0(t, t_0) - i \int_{t_0}^{t} \mathrm{d}t' U(t, t') V(t') U_0(t', t_0), \tag{122}$$

where $U_0$ is the time-evolution operator corresponding to $H_0$. It is worth to note that Eq. (122) is valid also for time-dependent zeroth-order Hamiltonians $H_0(t)$. In the SFA the full time-evolution operator inside the integral is typically approximated by the Volkov propagator, which is the solution to the Schrödinger equation where the electric field is fully accounted for, but the atomic potential is neglected. In the length gauge, with

$$H_{\mathcal{V}} = \frac{p^2}{2} + \mathbf{E}(t) \cdot \mathbf{r} = \frac{p^2}{2} + V_L(t), \tag{123}$$

the propagator takes the form

$$U_{\mathcal{V}}(t_2, t_1) = \int \mathrm{d}^3 k \, |\mathbf{k} + \mathbf{A}(t_2)\rangle \, \langle \mathbf{k} + \mathbf{A}(t_1)| \, e^{-iS_{\mathcal{V}}(t_2, t_1, \mathbf{k})}, \tag{124}$$

where $|\mathbf{p}\rangle$ represents a normalized plane-wave state, $\mathbf{k}$ is the conserved canonical momentum, and

$$S_{\mathcal{V}}(t_2, t_1, \mathbf{k}) = \frac{1}{2} \int_{t_1}^{t_2} \mathrm{d}\tau \, (\mathbf{k} + \mathbf{A}(\tau))^2 \tag{125}$$

is the Volkov-phase that corresponds to the classical action for an electron in an oscillating field. If we take the initial state to be the ground state of the atom $|\phi_0\rangle$, with ionization potential $I_p$, and the final state of to be a plane-wave of momentum $|\mathbf{p}\rangle$, then within the SFA the ionization amplitude is given by

$$M(\mathbf{p},t) = -i\int_{t_0}^{t} \mathrm{d}t' \left\langle \mathbf{p} - \mathbf{A}(t) + \mathbf{A}(t') \right| V_L(t') \left|\phi_0\right\rangle e^{-iS_{\mathcal{V}}(t,t',\mathbf{p}-\mathbf{A}(t))+iI_p(t'-t_0)}. \tag{126}$$

If the amplitude is evaluated at the end of the laser pulse, when $\mathbf{A}(T) = 0$, then it becomes

$$M(\mathbf{p}) = M(\mathbf{p},T) = -i\int_{t_0}^{T} \mathrm{d}t' \left\langle \mathbf{p} + \mathbf{A}(t') \right| V_L(t') \left|\phi_0\right\rangle e^{-iS_V(T,t',\mathbf{p})+iI_p(t'-t_0)}. \tag{127}$$

For intense, low-frequency pulses the Volkov-phase will be large due to a large value of the ponderomotive energy $U_p = A_0^2/4 = E_0^2/(4\omega^2)$. This will cause the phase factor in the ionization amplitude to oscillate rapidly, which means that the integral over $t'$ can be approximated with the saddle-point method [84]. The saddle point equation will in this case be

$$-\frac{\partial S_V}{\partial t'} + I_p = \frac{1}{2}(\mathbf{p} + \mathbf{A}(t'))^2 + I_p = 0. \tag{128}$$

For real $t'$ both terms of the equation are positive, so the solutions must be complex. This means that after choosing the appropriate saddle points, the amplitude will be exponentially suppressed, which is indicative of tunneling.

## 5.2 Previous works on frustrated tunneling ionization

Frustrated tunneling ionization was discovered experimentally in 2008 by Nubbemeyer et al. [28], who observed creation of neutral excited atoms for laser parameters in the tunneling regime. They performed simulations with a model based on tunneling with classical propagation of trajectories that and TDSE simulations that produced similar excited state distributions. Although the original experiment did not measure the excited state distribution, a later experiment confirmed the predictions of the FT model by measuring the excited state distribution using a technique based on field ionization [85]. The quasiclassical trajectory picture proposed in Ref. [28] is presented in Fig. 14.

### Classical simulations

Simulation of classical trajectories after tunneling has served as a useful tool for understanding different aspects of strong field physics [83], and also FTI has been studied with this

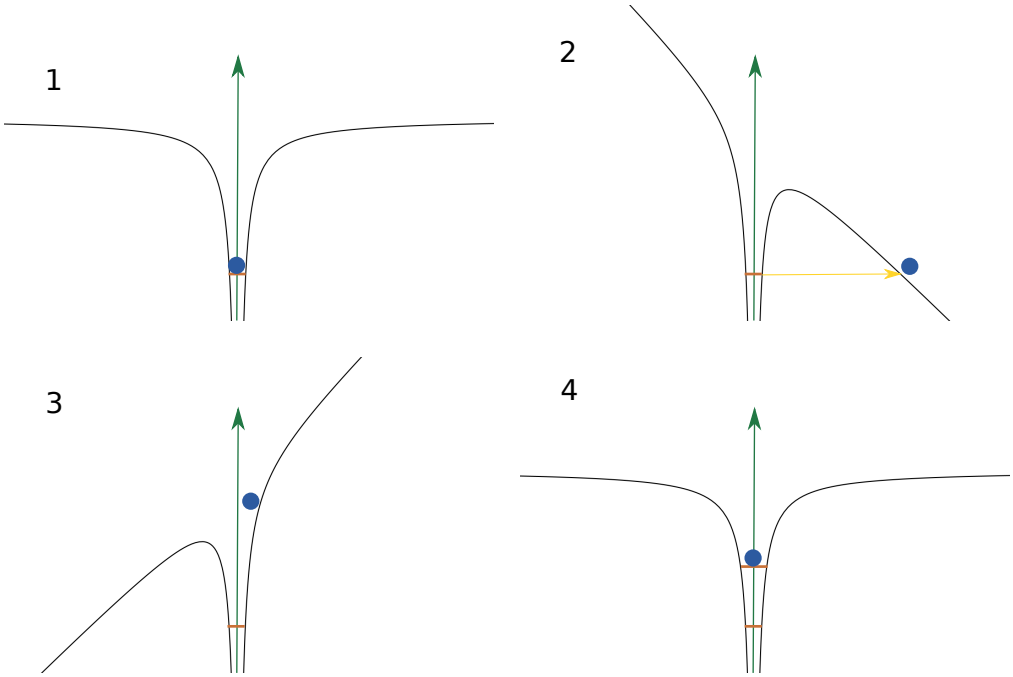


**Figure 14:** The picture of frustrated tunneling in the spirit of the three-step model for HHG. (1) The atom starts in the ground state, before the arrival of the laser pulse. (2) When the laser pulse has arrived, its electric field distorts the atomic potential, allowing the electron to tunnel. (3) The tunneled electron propagates in the combined potential of the Laser and the atomic core. (4) For certain tunneling conditions, the electron will be found in an excited state when the atom no longer interacts with the laser.

approach [28, 86–89]. Which trajectories that are bound at the end of the laser pulse in tunneling + classical simulations depend on the moment of birth (tunneling instant) and on the transverse momentum $p_\perp$ at the moment of birth. Whether a trajectory is bound or not also depends on the pulse duration. Longer pulse duration restricts the parameter space that leads to a bound orbit at the end of the laser pulse, see for instance Fig. 1 of Ref. [88], Fig. 1.1 of Ref. [89] and Fig. 3 of Ref. [87]. The parameter space that leads to a bound orbit is mostly located before a local maximum in the electric field. Such trajectories have the property that they don't return to the ionic core, and are therefore less likely to scatter strongly off the nucleus. However, certain initial conditions with tunneling after the peak of the electric field will still lead to a bound orbit through more complex dynamics driven by laser and Coulomb potential.

When the laser is turned on, there are classes of trajectories that follow Kepler like orbits, with oscillations due to the laser field superimposed [86, 88, 89]. Such trajectories can be studied with a guiding center model [90–92], and are essential for laser pulses that have a duration comparable to the Kepler orbit period.

## 5.3 Modeling frustrated tunneling ionization

Due to the success of SFA in providing useful insight into both HHG and ATI, one might ask if it can also be used to study FTI. In Ref. [27], Popruzhenko proposed an SFA-like model for FTI. It starts from regular SFA and the saddle-point expression for ionization, but adds conditions on the final energy and angular momentum that connects trajectories to specific excited states.

An obvious drawback of lowest-order SFA theory is that the resulting trajectories do not feel the Coulomb potential after tunneling. This could potentially be a problem, but it was not known if the model could provide new insights into possible interference effects. It is known from classical simulations that a delicate balance between the laser and the Coulomb potential on the trajectories is required for FTI [89]. The model was compared with TDSE calculations in paper v, showing that while multiple quasiclassical trajectories are predicted more work is required to fully understand the FTI process using SFA theory.

We now turn to the details of the SFA-FTI theory. The tunneling equation still reads

$$[\mathbf{p} + \mathbf{A}(t_s)]^2 = -2I_p, \tag{129}$$

and the extra constraints read

$$L^2(t_f) = [\mathbf{r}_s(\mathbf{p}, t_f) \times \mathbf{p}]^2 = p_\perp^2 \Delta G(t_f, t_s)^2 = \ell(\ell+1) \tag{130}$$

for angular momentum matching at the end of the pulse $t = t_f$, and

$$\frac{\mathbf{p}^2}{2} - \frac{Z}{\sqrt{\mathbf{r}_s(\mathbf{p}, t_f)^2}} = -\frac{Z^2}{2n^2}, \tag{131}$$

for energy matching to the principal quantum number, $n$, also at the end of the pulse. The amplitude for Rydberg state excitation is calculated by projecting the approximate solution onto the corresponding Rydberg state at the end of the laser pulse,

$$a_{n\ell m}(t_f) \approx \sum_{\mathbf{p}_s} \langle nlm|\mathbf{p}_s\rangle \, M(\mathbf{p}_s), \tag{132}$$

where $\mathbf{p}_s$ are the solutions to the above equations. One immediate question is how to define the end of the pulse for general envelopes of the field. In paper v we used a $\cos^2$ envelope with,

$$f(t) = \cos^2\left(\frac{\pi t}{\tau}\right), \tag{133}$$

which has a finite duration $\tau$.

**TDSE calculations and other model approaches**

I will end this section about FTI by a short overview of some TDSE calculations that have been performed by others, and also briefly mention some other quantum mechanical models that have been proposed for FTI.

In Ref. [93] Piraux et al. performed TDSE calculations of Rydberg state excitation for hydrogen with 800 nm and 1800 nm light. A comparison of the ionization probabilities with adiabatic limit was performed and gave good agreement for the simulations at 1800 nm. The excited state distributions were studied in $n$ and $\ell$, showing that longer pulses predominantly favors a specific parity. At 800 nm they observed out-of-phase oscillations between the ionization probability and excitation probability when the intensity is varied, with the later becoming enhanced after the closing of a multi-photon channel, which occurs due to the increase in the effective ionization potential $I_p + U_p$.

In Ref. [94] Zimmerman et al. performed TDSE calculations and experiments looking at channel closings as a function of intensity. Like in Ref. [93], they see that the closing of the m-photon channel due to an increase in the effective ionization potential is accompanied by an increase in the excitation yield. They propose an interpretation of the process in the frequency domain, where the closing of a multiphoton thresholds leads to resonance with the excited states just below the threshold.

An alternative model in the spirit of SFA was proposed by Hu et al. in Ref. [95]. It relies on the fact that in the expansion of the propagator, what is considered as a perturbation is allowed to change. Specifically they use one form of the exact propagator where the atom-field interaction is treated as a perturbation, and one where the binding potential is treated as a perturbation. Physically their model (at second order) consists of tunneling and subsequent Volkov propagation until the electron is captured by the binding potential and the subsequent propagation is approximated by a field-dressed Coulomb-Volkov state. There is also a first order SFA-like contribution that is neglected on physical grounds, based on the argument that in the long-time limit the SFA wave-packet will not contribute to bound state amplitudes due to quantum diffusion.

In Ref. [96], Piraux et al. used an approach that iterates in both the Coulomb and Laser interaction, where the lowest order corresponds to SFA, and the next order corresponds to Hu et al.'s model. For high-intensity IR fields the series did not converge to the TDSE results and there are large cancellations between different orders, and specifically between the first and second order. This shows that, at least for short pulses, the SFA contribution does not vanish. However, it should be noted that the calculations of Piruax and Hu were not performed in the same gauge, and SFA-like theories are known to not be gauge invariant in general [97].

Bengs et al. introduced a Kramers-Henneberger approach to strong field excitation in Ref. [98]. In the Kramers-Henneberger approach, a time-dependent unitary transformation is made, corresponding to a translation by the classical laser trajectory. This removes the time-dependent laser-atom interaction term from the Hamiltonian, at the cost of introducing a time-dependence in the atomic potential from the laser-driven trajectory. In the appropriate (high-frequency) limit the time dependent potential can be replaced by its cycle average [99], leading to a time-independent Hamiltonian with associated eigenstates known as Kramers-Henneberger states [100]. Setting the final state in the Dyson expression for the excitation amplitude as a Kramers-Henneberger state, and approximating the full propagator with the corresponding Kramers-Henneberger propagator leads to an expression that is similar to the ionization amplitude in SFA theory [100]. Applying the saddle point approximation leads to an equation for a tunneling time, which is again reminiscent to that of SFA theory [100]. The model is able to predict the period of Stückelberg oscillations in the populations of excited states [98]. The classical version of the Kramers-Henneberger approach is closely related to the guiding center models [91].

# Summary of results and applications

In this chapter the results of the papers included in the thesis are summarized, along with some additional applications and illustrations that were not covered in the papers.

## 6 Photoelectron signatures of non-perturbative XUV driven dynamics

Papers I-III all deal with dynamics driven by intense XUV fields. Papers I and II contain results from experiments performed at FERMI, together with our theoretical interpretations. Paper III concerns a prediction of stabilization of dressed states in resonant photoionization, which could potentially be studied at FEMRI, or another intense and coherent XUV source that supports circular polarization.

### 6.1 Rabi-dynamics in resonant FEL experiments

In paper I, we reported on an experimental observation of an Autler-Townes-like splitting in the photoelectron spectrum in a resonant photoionization experiment performed on helium atoms using the seeded FEL source FERMI. The photon energy was close to the $1s^2 \rightarrow 1s4p$ transition for helium, and the pulse duration and intensity estimates allow for the atom to complete at least one period of Rabi cycling during the pulse, see Fig. 15. The experimental data showed asymmetry in the AT doublet when the FEL pulse was detuned from the resonance, see Fig. 16 (a). We could not explain this feature by considering ionization only from the excited state as done by Knight. Thus, we wanted to better understand this phenomenon.

In order to reproduce the experimental results TDCIS simulations were performed. Photoelectron spectra were computed using the t-SURFF and i-SURF methods [101, 102]. The simulations show that the symmetry of the AT-dobulet depends on the detuning, with

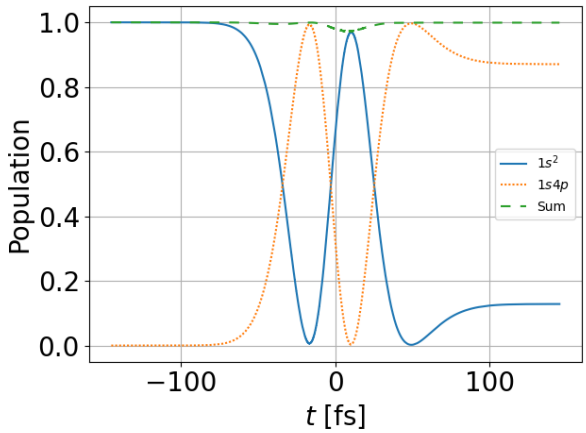


Figure 15: Populations of the ground state ($1s^2$) and excited state ($1s4p$) computed within velocity gauge TDCIS, with the laser parameters used in paper I. The interaction corresponds to a pulse area close to $3\pi$ (1.5 Rabi periods).

the most symmetric doublet being found at a slight blue detuning from the field-free resonance, which is also the case for the experiment, see Figs. 16 (a) and (b). The observed blue shift was larger than the estimated ac Stark shift, which implies that some other mechanism was at play.

To better understand the experimental photoelectron spectra and the TDCIS results, a model based on the theory described in Sec. 3 was constructed. With a flat-top envelope for the interaction it was found that the non-resonant pathway was needed to explain the asymmetry in the experimental spectrum, see Figs. 16 (c) and (d). The blue shift of the symmetric AT doublet was found to be larger with a flat-top envelope than for the TDCIS simulations with a Gaussian envelope, but simulations performed with a smooth flat-top produced blue shifts of similar size. At the intensity suggested by the splitting of the AT doublet in the experimental PES, it was found that the two ionization pathways are of similar strength, and so both are needed to interpret the results in terms of a quantum interference effect.

### Interference between resonant and non-resonant ionization

Since there is a substantial difference in the relative strength between the two ionization pathways for the $s$- and $d$-waves, see Tab. 1, one of them can be dominant in one channel, while the other is stronger in the other one. Figure 17 shows this effect when the duration is close to one Rabi period. In (a), only the contribution from $s$ states are included, and we see a single peak in the photoelectron spectrum when the detuning is small. In contrast, for (b) only the contribution from the $d$ partial wave was included, and we see an AT doublet

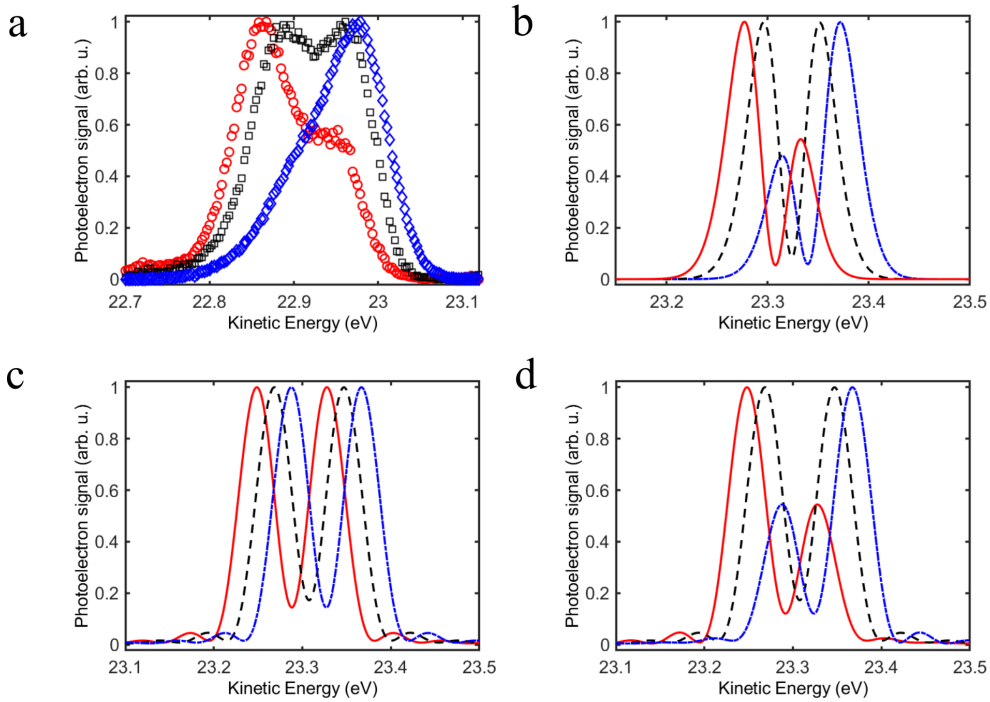


Figure 16: Experimental (a) and TDCIS (b) photoelectron spectra for three different photon energies, each separated by 13 meV. Model calculations for flat-top envelope, contribution from excited state Eq. (70) (c) and ground state Eq. (80) (d). The figure is reproduced, without modificaions, from Fig. 2 of paper I, under a CC BY 4.0 license.

in the spectrum. This also affects the angular distribution, see e.g. Fig. 31 of Ref. [103].

### Photoionization domains

With the ionization rates derived in Sec. 3.5, we can study which dynamics the simple model suggests should be relevant in different pulse intensity and duration regimes. This is done in Fig. 18 for the first few excited states in the $1snp$ Rydberg series of He, with the photon energy set to the field-free resonance energy for simplicity. The shaded area indicates regions where the model suggests that Rabi oscillations should be taking place. The lower limit is set by the Rabi period, and the upper limit by the radiative lifetime of the excited state and the lifetime associated with the two ionization processes included by the model. Figure 18 suggests that, for all the states included, there is quite a large parameter space where Rabi oscillations are possible. Specifically, at the estimated intensity and pulse duration for the $1s4p$ experiment of paper I, there is a difference of several orders of magnitude between the Rabi period and the time scale on which the atom is depleted due to ionization. This point is also illustrated in Fig. 15, where the total population in the

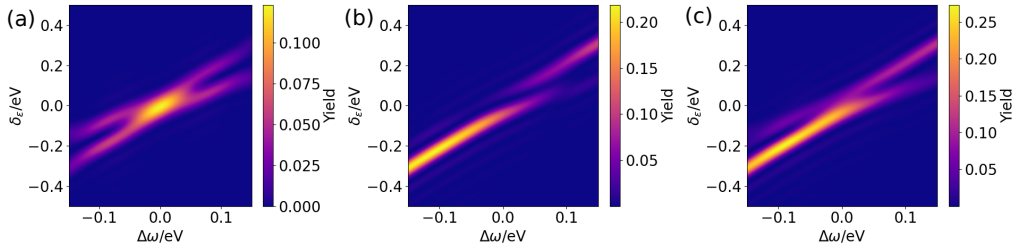


Figure 17: Photoelectron spectrum for resonant ionization of near the $1s4p$ transition, as a function of the detuning. The spectrum is plotted relative to the expected kinetic energy at the resonance. (a) Only $s$ photoelectrons, (b) only $d$ photoelectrons, (c) combined signal. The pulse duration is 56 fs, at an intensity of $2 \times 10^{13}$ W/cm$^2$.

two-level system is very close to 1 at the end of the pulse (dashed line).

As the intensity is increased, a point is reached where the rate for the non-resonant second order process overtakes the rate of the process that corresponds to one-photon ionization from the excited state. This is indicated in the figure by the crossing of the lifetime a and lifetime b lines, and the shaded area switching from salmon color (I) to blue (II). Here the combined rate transitions from linear to quadratic intensity scaling.

From Fig. 18 we can see that the transition between the two domains happens at lower intensities for the higher lying excited states, which was also seen in Tab. 1 in Sec. 3.4. This can be understood from the definition of $|\rho_{\neq b}\rangle$, Eq. (77). As we go up in the Rydberg series, the distance in energy to the closest state in $\mathcal{Q}$ decreases, meaning that the numerator in Eq. (77) becomes smaller, which implies larger contributions from the ground state via the non-resonant states. Therefore, the $1s^2 - 1s2p$ transition in helium is the one that mostly ionizes from the excited state at low intensities. Our work shows, however, that even in this case the contribution from the groundstate becomes important beyond $10^{14}$ W/cm$^2$, see Fig. 18 (a).

**Entanglement in core resonant photoionization**

In the experiment of paper II, photon energies in the range around 40.8 eV were used. This is above the first ionization threshold of He, but also close the $1s \rightarrow 2p$ transition in $He^+$ (40.814 eV). A sufficiently intense field should therefore be able to drive transitions between these two states in the ion. This means that we are in the situation described in Fig. 6 (c), and one might expect to see a GE doublet in the photoelectron spectrum [56]. The experiment was performed in a regime where the pulse duration was longer than the estimated Rabi period, and a doublet structure is indeed visible in the spectrum, when the FEL frequency was detuned slightly from the resonance.

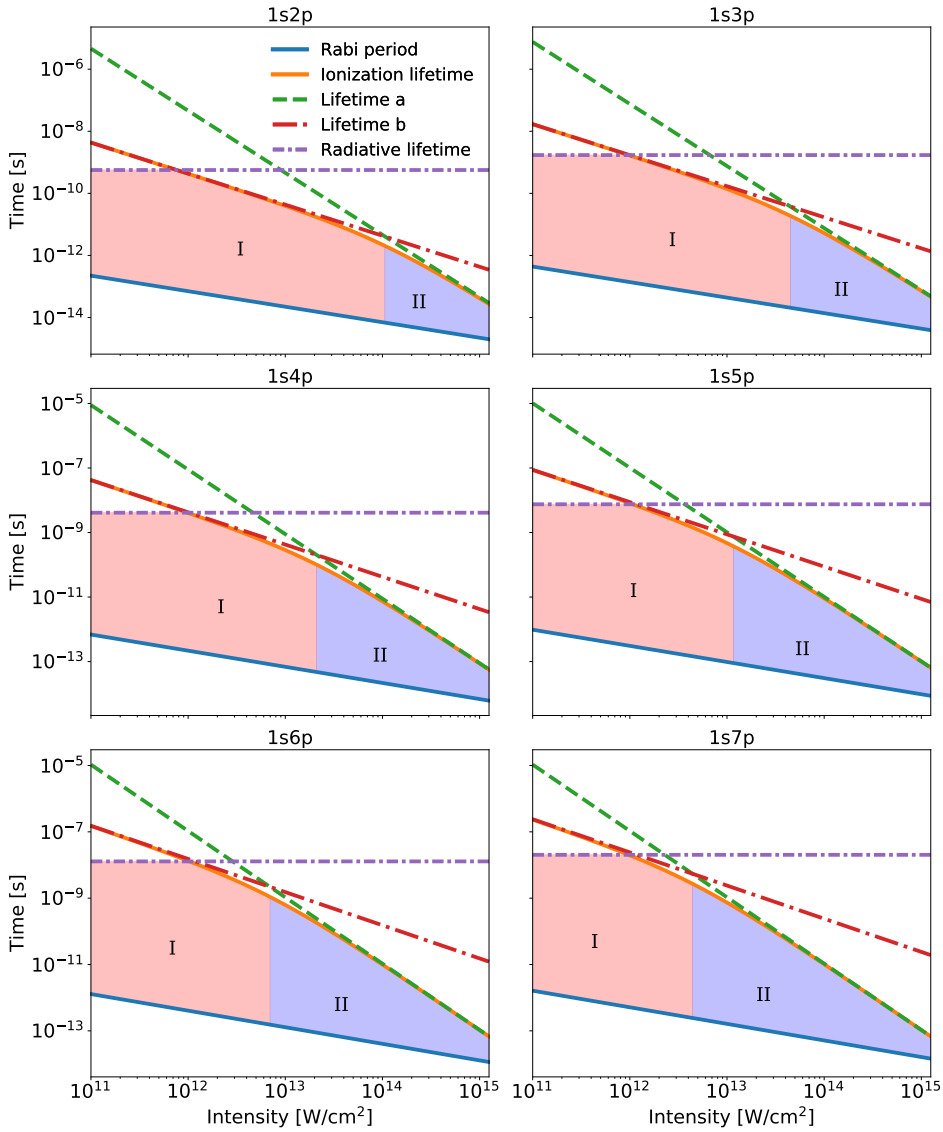


**Figure 18:** Photoionization domains for resonant two-photon ionization in the He Rydberg series, computed with the matrix elements of Tab. 1.

A model based on the Dyson equation was constructed, which includes the following states

$$
\begin{aligned}
&|g, N\rangle\,, \text{ Ground state of He and } N \text{ photons,}\\
&|\phi_a, E_{\text{kin}}, N-1\rangle\,, \text{ He}^+ \text{ ground state, photoelectron and } N-1 \text{ photons,}\\
&|\phi_b, E_{\text{kin}}, N-2\rangle\,, \text{ He}^+ \text{ excited state, photoelectron and } N-2 \text{ photons.}
\end{aligned}
\tag{134}
$$

According to our model, the final state of the system asymptotically approaches a quantum superposition on the form

$$\begin{aligned}|\Psi\rangle =& \frac{1}{2}\Big[(|\phi_a, N-1\rangle + i\,|\phi_b, N-2\rangle) \otimes \left|E^-_{\text{kin}}\right\rangle \\ &+ (|\phi_a, N-1\rangle - i\,|\phi_b, N-2\rangle) \otimes \left|E^+_{\text{kin}}\right\rangle\Big],\end{aligned} \tag{135}$$

which is an entangled state. This is because the ion-field superpositions associated to the higher, $E^+_{\text{kin}}$, and lower, $E^-_{\text{kin}}$, photoelectron energies of the GE doublet are the orthogonal dressed states $\frac{1}{\sqrt{2}}\left(|\phi_a, N-1\rangle \mp i\,|\phi_b, N-2\rangle\right)$. Thus the state cannot be factorized into the form $|\text{Ion, Photon}\rangle \otimes |\text{Photoelectron}\rangle$, and it corresponds to a fully entangled state.

## 6.2 Dressed-state stabilization in resonant ionization

Following the prediction by Beers and Armstrong [11] of stabilization of one of the dressed states due to interference between resonant and non-resonant ionization processes, we investigated the conditions for stabilization to occur in realistic systems. Since one of the conditions is roughly equal atomic ionization rates ($\gamma_b$ and $\gamma_a$), which we believe was achieved in paper I, we wanted to further investigate their prediction and assumptions. The critical assumption made in Ref. [11] that leads to complete stabilization, is that they only consider the case where the electron is coupled to a single ionization continuum. For complete stabilization, the conditions needs to be satisfied for every open ionization channel.

Holt et al. state that $\beta = \sqrt{\gamma_a \gamma_b}$ [13], however this does not hold in general when there is more than one ionization channel, as shown in Appendix B of paper III. It is rather of the form $\beta = \sum_\ell \sigma^\ell \sqrt{\gamma_a^\ell \gamma_b^\ell}$ where $\ell$ denotes the open ionization channels, and $\sigma^\ell$ generates the appropriate sign of each term. For linear polarization from an initial $S$-state there are two ionization channels, corresponding to $s$ and $d$ photoelectrons. For circular polarization, the dipole selection rules require $\Delta m = \pm 1$. This means that only $d$ photoelectrons are allowed in two-photon ionization. Clearly this condition can be met for the helium atom in its ground state. We thus predict that helium could be stabilized to a greater extent using circular polarization than what is possible with linear polarization. This is illustrated in Figs. 19 (a) and (b) which show the ionization rates of the dressed states for linear (a) and circular polarization (b) as a function of intensity, for resonant ionization via $1s2p$ in He.

As was mentioned in Sec. 4.4, while one of the dressed states has a suppressed ionization rate, the other rate is enhanced. This is enough to compensate for the stabilized state at short times, so that it is not possible to see the effect of stabilization in the total ionization probability. Stabilization can only be seen in the ionization probability once the state with

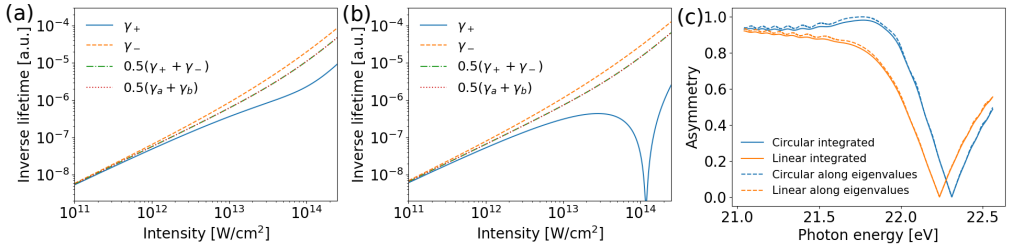


Figure 19: Dressed state ionization rates for (a) linear and (b) circular polarization, for the field free $1s2p$ resonance in helium predicted by CIS (21.69 eV). (c) Comparison of the asymmetry of AT doublet as a funciton of photon energy for linear and circular polarization. The intensity is $1.1 \times 10^{14}$ W/cm$^2$, and the pulse duration is 10 Rabi cycles. (a) and (b) are adapted from Fig. 5, and (c) from Fig. 6, of paper III under a CC BY 4.0 license.

enhanced ionization rate has been significantly depleted. In helium for the laser parameters where stabilization takes place, the lifetime of the bound states due to ionization is significantly longer than the Rabi period, see Fig. 18, so the total amount of ionization is rather low for realistic pulse durations. Thus, it may appear hopeless to detect the stabilization mechanism.

However, since the two main peaks of the AT doublet are populated by ionization from one of the dressed states $|+\rangle$ and $|-\rangle$, any difference in the ionization rates of the two states will affect the symmetry of the doublet. If one of the dressed states is stabilized, the corresponding component of the AT doublet should vanish, since no ionization takes place to the corresponding energy. Therefore, we suggest that stabilization could be inferred from the photoelectron spectrum by studying the asymmetry of the spectrum as a function of the laser parameters and looking for parameters where the spectrum is completely asymmetric. The asymmetry of the spectrum can be studied quantitatively, as was done by Zhang et al. in Ref. [16]. Figure 19 (c) shows the asymmetry parameter

$$A = \frac{|S_+ - S_-|}{S_+ + S_-}, \tag{136}$$

where $S_+$ ($S_-$) is the signal in the upper (lower) AT-component, as a function of the photon energy. Near the resonance the asymmetry for circular polarization has a maximum, $A \approx 1$, which is absent for linear polarization. The connection between stabilization, or population trapping, and the photoelectron spectrum has been noted also in previous works, see e.g. Ref. [104].

### Envelope effects

The effect on the AT doublet of including an envelope is illustrated in Fig. 20, where four different envelopes are compared using a version of the theory of Sec. 4 in which the parameters of $H_{\text{eff}}$ follow the intensity envelope. The super-Gaussian envelope sequence that

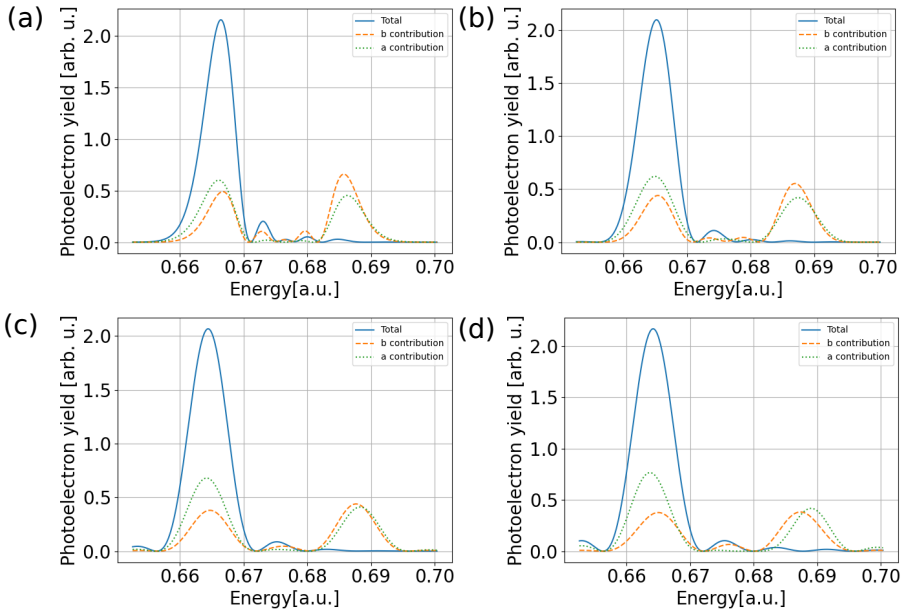


**Figure 20:** Photolectron spectra computed for four different envelopes with intensity FWHM 19.305 fs. The light is circularly polarized and the intensity is in the stabilization regime. The envelopes are (a) Gaussian, (b) super-Gaussian, (c) fourth order super-Gaussian, and (d) flat-top.

was used is defined as

$$f(t) = \exp\left[-\frac{\ln(2)}{2}\left(\frac{2t}{\tau}\right)^{2n}\right], \tag{137}$$

where $\tau$ is the full-width at half maximum (FWHM) of the intensity profile. This sequence interpolates between Gaussian ($n = 1$) and flat-top ($n \to \infty$) envelopes. Figure 20 (a), (b) and (c) corresponds to $n = 1$, $n = 2$ and $n = 4$, respectively, while a flat-top envelope was used in (d).

In addition to the total spectrum, also the individual spectra from the resonant and non-resonant processes are shown in Fig. 20. We note that the smooth envelopes introduce an asymmetry in the contribution of the excited state process. However, this asymmetry is both weaker and opposite to that stemming from the ground state amplitude, which shows that the asymmetry in paper I can not be attributed to envelope effects. Furthermore, the spectra show that even when envelopes are included, it is still possible for the interference between the two ionization processes to have a large influence on the final spectrum.

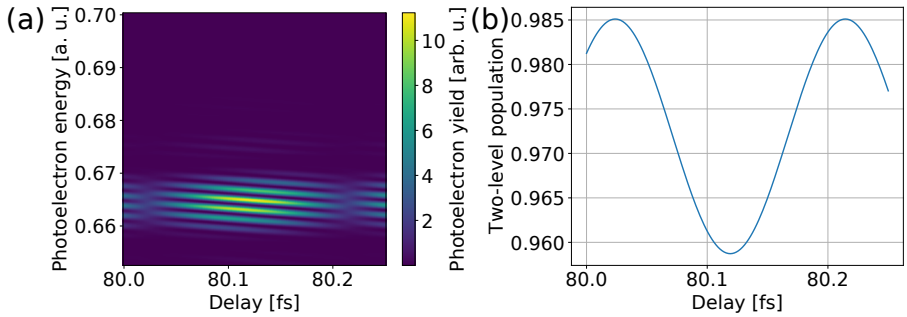


Figure 21: (a) Photoelectron spectrum as a function of delay between the two pulses. The intensity is in the stabilization regime for $1s2p$ resonant ionization of He. A fourth order super-Gaussian envelope was used, with the pulse area slightly below $6.5\pi$. (b) Population remaining in the two-level system as a function of the delay. The population after the first pulse is $0.9852$, and it places the atom in a superposition of ground and excited state.

### Control of ionization by preparation of dressed states

The pump-probe scheme of Wollenhaupt et al., Ref. [59], consists of a set of two time delayed pulses that both lead to resonant photoionization. Here, we predict that this kind of experiment would be strongly modified in the stabilization regime. Compared with Fig. 8, the spectrum of Fig. 21 (a) shows a strong suppression of the upper component of the AT doublet. The lower component still shows the same kind of interference fringes that were predicted in Ref. [59]. Figure 21 (b) shows the population left in the two-level system at the end of the second pulse. The oscillations in the two-level population follows the changes in the fringe structure of the lower AT component in (a). There is a minimum for the delay where the fringes are the strongest, and maxima where the fringes are not present. This is easily understood in the dressed-state picture. The first pulse leaves the two-level system in a nearly equal superposition of $|a\rangle$ and $|b\rangle$. The delay of the second pulse introduces a phase that controls the phase of the superposition. Depending on the relative phase, the atom can be in either of the two dressed states, or in a non-stationary state. This means that for certain delays, the superposition prepared by the first pulse will correspond to one of the dressed states [59], and ionization will only take place from this state. When only the $|-\rangle$ state is populated there is strong interference in the lower component, and the second pulse leads to more ionization. When instead the $|+\rangle$ state is populated, there are no fringes in the lower component and the second pulse leads to very little further ionization, consistent with the fact that $|+\rangle$ is stabilized.

A related mechanism for controlling the amount of ionization by selectively populating one of the dressed states was proposed by Saalmann, Giri and Rost in Ref. [15]. By introducing a chirp to the XUV pulses, the adiabatic picture suggests that most of the population will remain in either the $|+\rangle$ or the $|-\rangle$ state during the pulse, depending on the sign of the chirp. Their simulations for linear polarization show a reduction in total amount of ioniza-

tion when adiabatically following the $|+\rangle$ state (negative chirp), and that the asymmetry of the AT doublet can be controlled by the chirp. An experiment was recently performed at FERMI using this scheme, but with circularly polarized pulses, where a reduction in the ionization rate was observed for negative values of the chirp [10]. The results of paper III suggests that this effect should be more pronounced with circular than with linear polarization for experiments performed in the stabilization regime.

### Exceptional points in resonant photoionization

The exceptional points of $H_{\text{eff}}$ are points in parameter space where the complex eigenvalues $\lambda_\pm$ coalesce, and the dimension of the eigenspace is reduced to one [62, 105–107]. For the $H_{\text{eff}}$ studied in paper III and in this thesis, this requires the conditions

$$\Delta^2 + \Omega^2 = \frac{(\gamma_a - \gamma_b)^2}{4} + \beta^2, \tag{138a}$$

$$\Delta \frac{\gamma_a - \gamma_b}{2} = \Omega\beta, \tag{138b}$$

where $\Delta = E_a + \delta_a - E_b - \delta_b$. This can be reduced to the following conditions

$$\Omega = \pm\frac{\gamma_a - \gamma_b}{2}, \tag{139a}$$

$$\Delta = \pm\beta, \tag{139b}$$

which means that the Rabi frequency should be comparable to the difference in atomic ionization rates. However, for the case considered here, and where the model is valid, we can not expect to find any exceptional points since typically $\Omega \gg \gamma_a, \gamma_b$. There is one trivial solution $\Delta = \gamma_{a,b} = \Omega = \beta = 0$ (non-interacting case), but there one can still find two orthogonal eigenvectors. Instead, the exceptional points are expected to occur for complex values of the field strength $E_0$ [108].

This is indeed the case as is illustrated in Figs. 22 and 23. Figure 22 shows the difference between the eigenvalues of $H_{\text{eff}}$ as function of field strength and detuning, over a range where the model is expected to valid. One can see the trivial solution at $E_0 = \Delta = 0$, but there appears to be no other solutions. Figure 23 on the other hand, shows $\lambda_+ - \lambda_-$ as a function of complex field strength, in the spirit of Ref. [108]. The left column (a, c) shows $|\lambda_+ - \lambda_-|$, and the right one (b,d) shows the phase of $\lambda_+ - \lambda_-$. In the top row (a, b) the field free detuning is 0, while a 3 % detuning is introduced in the bottom row (c, d). (a) and (c) show that in this region of the complex plane there are four solutions to the above equations (the one at $E_0 = 0$ in (a) is a double root). From (b) and (d) one can see that the points where two eigenvalues are identical are associated with branch cuts, as they should be [105, 108].

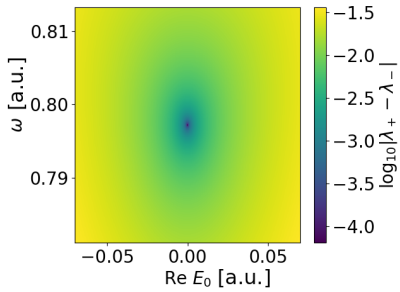


Figure 22: Absolute value of the difference $\lambda_+ - \lambda_-$ as function of field strength and detuning. The $H_{\text{eff}}$ used is the one for He interacting with circularly polarized light, studied in paper III.

In Refs. [62, 107], there is greater possibility to control the eigenvalues of $H_{\text{eff}}$ since there are more parameters to vary. In Ref. [62], the autoionization lifetime does not depend on the field strength, and can thus be seen as an independent parameter. The multicolor approach of Ref. [107], where different fields control ionization and Rabi oscillations, also has more parameters that can be tuned, and therefore the conditions for exceptional points can be satisfied.

# 7 Rabi oscillations in RABBIT

In the original RABBIT scheme the IR field is assumed to not be resonant with any bound states, so that the transitions that are induced by the IR-field take place once the electron is already in the continuum [29–31, 109], see Fig. 24 (a). If the IR is resonant with a bound state, this opens up additional pathways for interference in the sideband signal, since the atom can first absorb one IR photon to reach an excited state before it absorbs an XUV-photon from the APT and ejects an electron into the continuum [110], see Fig. 24 (b). If the IR can induce Rabi oscillations in the atom, both the main harmonic peaks and the sidebands split into AT doublets [55].

## 7.1 Circularly polarized RABBIT applied to a Rabi-cycling atom

In paper IV, the RABBIT scheme was used to study the dynamics of a Rabi cycling Li atom, where the IR is resonant with the $2s$ to $2p$ transition. Specifically the different contributions to the sideband phases are studied in great detail through numerical simulations and perturbative calculations in the spirit of paper I. A single active electron potential for Li was used [111].

Paper IV extends the work of Ref. [55] by including more pathways in the perturbative

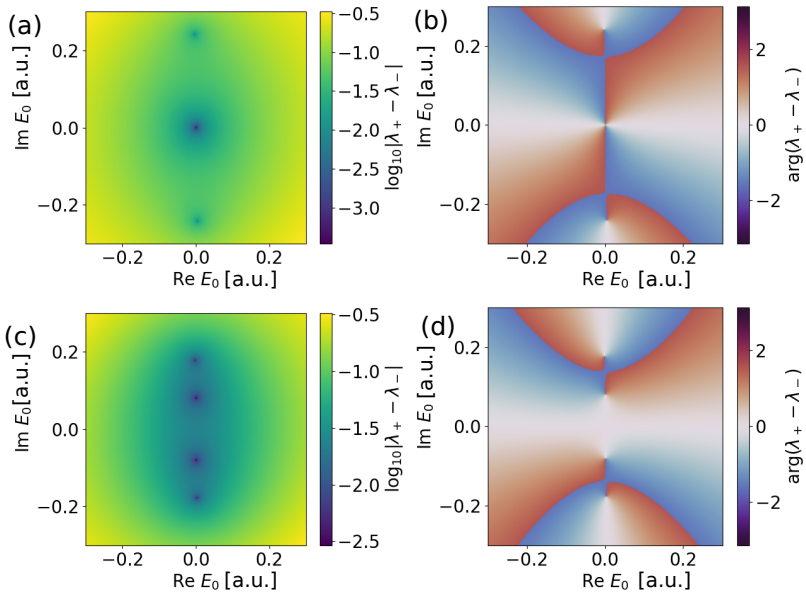


**Figure 23:** Exceptional points of $H_{\text{eff}}$ in the complex $E_0$ plane for resonant ionization of He interacting with circularly polarized light. Panels (a) and (c) show $|\lambda_+ - \lambda_-|$, while (b) and (d) show the associated phase. For (a) and (b) the detuning is 0, while for (c) and (d) it is 3 %.

calculations, and by considering the case of circular polarization instead of linear polarization. Circular polarization is used in order to minimize the transitions to bound states outside the two-level system, since the dipole selection rules for circularly polarized light excludes the $3s$ level, which would otherwise be the level closest to having a two-photon resonance with the ground state. It is found that in the case of co-rotating IR and XUV fields, some processes involving two IR transitions in the continuum are required to explain the behavior of the sideband phase, due to their interference with lower order processes. The pathways needed to explain the numerical results are illustrated in Fig. 25.

Table 5 contains the radial components of the ionization dipole matrix elements for the paths shown in Fig. 25. Paths (b) and (e) can also reach other partial waves than the one included in the table. A comparison is made between the complex rotation method of Gao and Starace, Ref. [112], and the extrapolation method of Cormier and Lambropoulos, Ref. [76], for dealing with ATI transitions. The extrapolation method was introduced in Sec. 4.3.

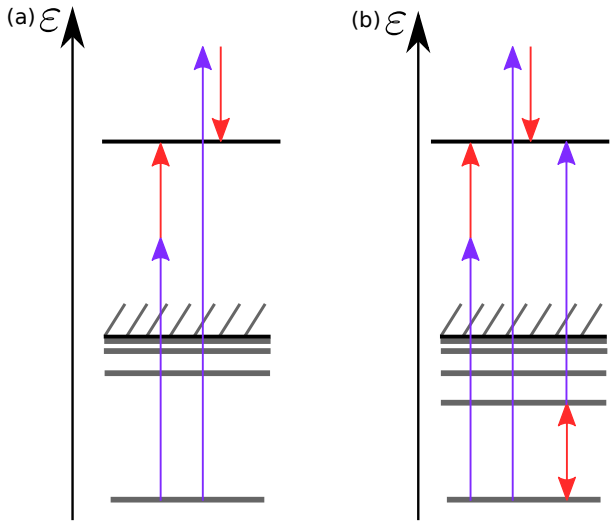


Figure 24: (a) The standard RABBIT scheme with sideband interference due to IR transitions in the continuum. (b) When the IR is resonant with a bound state there are additional paths that can cause interference in the sideband signal, which here is indicated by the path where the IR photon is absorbed before the XUV photon.

Table 5: Comparison of radial matrix elements, computed with complex rotation and the extrapolation method for a few selected paths that were used in paper IV. The different paths are illustrated in Fig. 25

| Path | Angular momenta | Complex rotation | Extrapolation |
|---|---|---|---|
| a | $(0, 1, 2)$ | $112.18 + 145.30i$ | $112.30 + 145.37i$ |
| b | $(0, 1, 0)$ | $40.385 + 134.14i$ | $40.544 + 134.46i$ |
| c | $(1, 2)$ | $0.33566$ | $0.33589$ |
| d | $(1, 2, 3, 4)$ | $16840 + 12576i$ | $17264 + 13725i$ |
| e | $(1, 2, 1, 0)$ | $-10202 - 4446.6i$ | $-10194 - 4624.1i$ |

# 8 Frustrated tunneling in ultrashort laser pulses

We compared the model of Ref. [27] with TDSE calculations for ultra-short pulses ($\cos^2$ envelope) in Hydrogen at 800 nm and intensities on the order of $10^{14}$ W/cm$^2$. We specifically studied the CEP dependence of the excited state distributions and compared with TDSE results. The conclusion was that the agreement is at most qualitative. In addition, the selection of physically relevant solutions (i.e. exponentially damped) is a non-trivial task.

## 8.1 Understanding the SFA-FTI model

The solutions to the modified saddle point equations fall into four classes of trajectories, which we labeled $\alpha$, $\beta$, $\gamma$, and $\delta$. As a function of the angular momentum of the final state

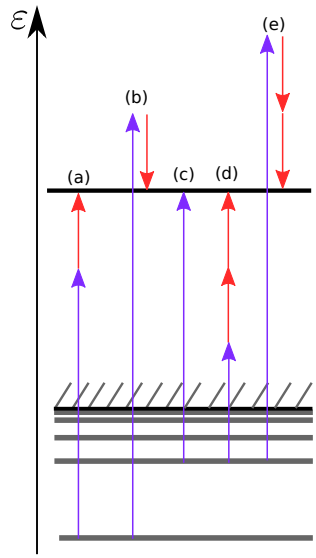


**Figure 25:** Dominant contributions to the sideband signal in the Rabi-RABBIT scheme for Li atoms interacting with circularly polarized light.

$\ell$ for a fixed principal quantum number $n$, the different classes trace out complex curves in the solution space, see Fig. 26 (a) for an example for $n = 8$. The $\alpha$ and $\beta$ trajectories differ mostly in the real part of the excitation time $t_s$ up until some cut-off $\ell$ where the solutions perform a kind of avoided collision with similar real part of $t_s$ and the imaginary part of $t_s$ going in different directions for the two trajectories, analogous to the cutoff behavior for saddle-point solutions that can be seen for HHG, see e.g. Ref. [113]. The $\gamma$ and $\delta$ trajectories have similar real part of $t_s$ but differ in the imaginary part. For low angular momenta the $\beta$ trajectories have a real part of $t_s$ that comes slightly before the peak of the electric field, while the $\alpha$ trajectories come slightly before, see Fig. 26.

Classical trajectory simulations have shown that electrons that tunnel before and after the peak of the field can be captured into Kepler orbits at the end of the pulse [87–89], but that only those with some initial transverse momentum can tunnel after peak of the field and still be bound at the end of the pulse [87–89]. As pulses get longer and more intense, the parameter space that lead to a bound orbit at the end of the pulse shrinks, and tunneling before the peak of the field becomes more favored, see Fig. 1.1. of Ref. [89].

After the avoided collisions in $\ell$, the imaginary part of the action associated to the $\beta$ solutions grows dramatically. We considered this as unphysical, and therefore a filter in time and momentum was introduced to remove such solutions.

Classical simulations clearly indicate that the Coulomb potential has a large influence on the trajectories, see e.g. Fig. 2 of Ref. [88], especially on time scales that are comparable to

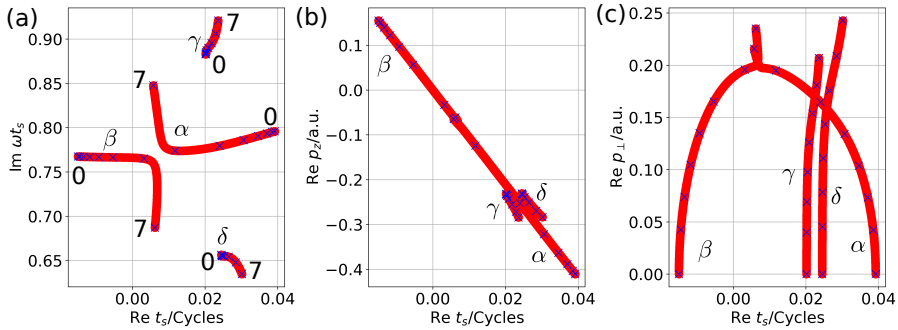


Figure 26: How the solutions of the modified tunneling equations change as a function of $\ell$ for $n = 8$. Blue crosses indicate the physical values of $\ell$. The $x$-axis indicates the real part of $t_s$ and the $y$-axis gives (a): imaginary part of $t_s$, (b): real part of $p_z$, and (c): real part of $p_\perp$. $\mathrm{Re}\, t_s = 0$ indicates the peak of the electric field. The solutions were generated with a pulse duration of two cycles for laser with frequency $\omega = 0.057$ a.u., at an intensity of $1.5 \times 10^{14}$ W/cm$^2$.

the periods of Kepler orbits. This suggests that the model that was considered in paper v should only be applicable for short laser pulses, such that the influence of the Coulomb potential on the trajectory is sufficiently small.

The result of not including the Coulomb interaction after the tunneling step is illustrated in Fig. 27. Like similar figures in Refs. [87–89, 114], it shows which trajectories lead to a bound orbit at the end of the laser pulse, when they tunnel close to the peak of the electric field. In the upper row, the Coulomb potential is included during the propagation of the classical trajectories, while for the bottom row it has been excluded. The non-Coulomb case shares some similarities with the $\alpha$ and $\beta$ trajectories in Fig. 26 (c), in that both tunneling times before and after the peak of the field leads to bound orbits. In contrast to this, including the Coulomb potential heavily favors tunneling before the peak of the field, which corresponds to $\beta$ trajectories of paper v.

The two cases show quite different behaviors as the pulse duration is increased (left to right). In the non-Coulomb case the maximum allowed $p_\perp$ decreases as the pulse duration is increased, while including the Coulomb potential instead leads to a slight increase. The Coulomb case also shows the formation of rather intricate structures, as previously shown in e.g. Ref. [88], that are absent when the Coulomb potential is excluded.

We thus expect the $\alpha$ trajectories to play a minor role in more accurate calculations, while the $\beta$ trajectories could potentially serve as a starting point for improved versions of the SFA-FTI model and the study of inter-cycle interference effects.

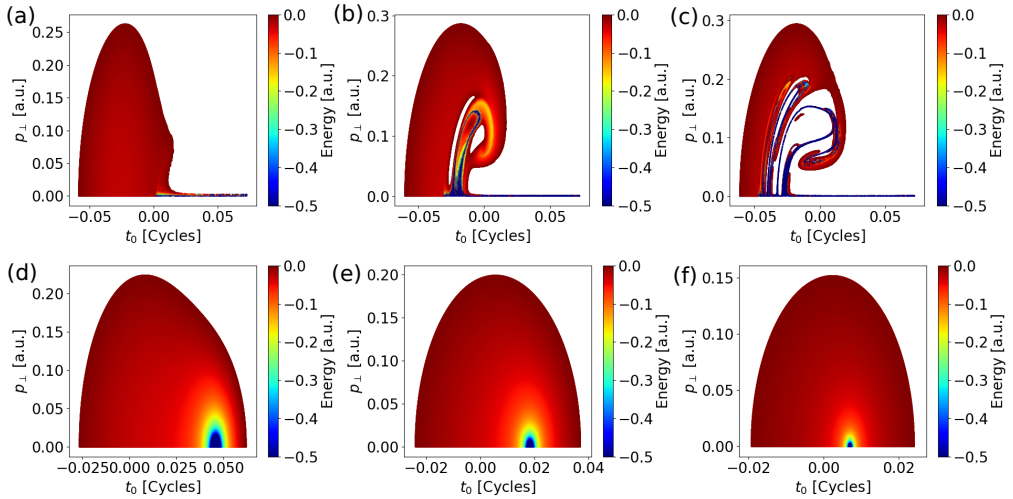


Figure 27: Map of tunneling time and initial transverse momentum that lead to bound orbits at the end of a $\cos^2$ laser pulse. The tunneling times are chosen close to the central peak of an electric field with cosine like CEP. The Coulomb potential is included during propagation in panels (a)-(c), and exlcuded in panels (d)-(f). The color indicates the energy of the trajectory at the end of the pulse, with energies below $-0.5$ a.u., mapped to $-0.5$ a.u. The pulse duration for the different panels are 2 cycles for (a) and (d), 4 cycles for (b) and (e), and 10 cycles for (c) and (f). The intenisty and freqeuncy of the laser was the same as in Fig. 26.

## 8.2 TDSE results

In accordance with earlier TDSE calculations [93], the excited state distributions are sensitive to the pulse duration, with longer pulses favoring a specific parity. The model was not able to reproduce the population of a specific parity for longer pulses, see Fig. 6 of paper v. Population of rather high angular momentum states is consistent with previous studies [93, 114], but the model was not able to reproduce this feature. A possible reason for this is that the model neglects the Coulomb interaction, and thus the allowed values of $p_\perp$ are reduced with increasing pulse duration. Classical simulations show a strong correlation between $p_\perp$ and the final angular momentum [114].

To study the influence of continuum states on the final excited state population, an imaginary component of $-0.5$ a.u. was added to continuum energies for some TDSE calculations, and it was found that indeed the population of excited states is influenced by the continuum states, see Fig. 28. The imaginary part leads to a decay of the population in the continuum.

In conclusion, we found that the model was not fit to understand FTI at a quantitative level, but it did bring forward a semiclassical picture that could be linked to classical trajectory models.

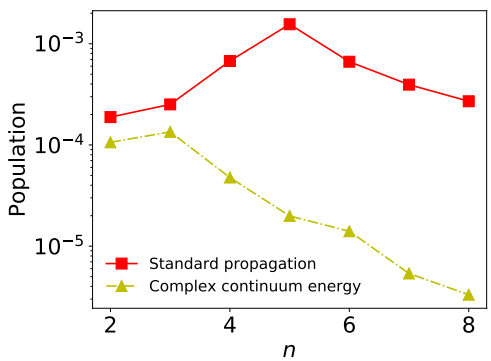


**Figure 28:** Principal quantum number distribution with and without complex continuum energies. The figure is adapted from Fig. 7 of paper v, under a CC BY 4.0 license.

# Summary and outlook

This thesis has studied the interaction of atoms with intense XUV and IR fields. All the problems that were studied involved the dynamics of the bound states in some way, either through Rabi oscillations, papers I-IV, or through frustrated tunneling ionization, paper V. In papers I and II comparisons were made between model and experiment, while the models and simulations of papers III-V provide predictions for future experiments.

In paper I the AT doublet in resonant photoionization of helium atoms was studied, and an interference effect between ionization from ground and excited state was suggested. Interference between ground and excited state ionization processes can also be achieved by probing a Rabi oscillating atom with an attosecond pulse train, which was studied in paper IV, or by adding a second field that couples the ground state to the continuum, as recently suggested in Refs. [115–117].

Paper II studied the formation of the GE doublet in the XUV regime, and showed how the underlying process generates entanglement between photoelectron and ion. Although the generated entanglement might not be of much practical use for quantum information processing tasks, it still serves as a nice demonstration of the capabilities of seeded FELs.

The stabilization effect that was studied in paper III relies on the fact that the selection rules for circularly polarized light restricts quite heavily the allowed final states when starting from a ground state that only contains orbitals of $s$ character, like hydrogen and helium. So it remains to see if the effect is present to the same extent in other systems, where more ionization channels are available. The difference between linear and circular polarization for helium suggests that the restriction to one channel is quite important, in order to maximize the relative stabilization of one of the dressed states. Experiments at FERMI using circularly polarized light can reach the intensity regime where stabilization is predicted for helium ($\approx 10^{14}$ W/cm$^2$), as demonstrated recently in Ref. [10], and the effect should be interesting to study with techniques that can selectively populate dressed states [10, 15, 59].

Another area where modern FEL capabilities could play a part is the exploration of exceptional points in autoionization. Although FELs operating in the XUV range were not

available at the time Latinne et al. predicted the existence of exceptional points for the $3s^{-1}4p$ autoionizing resonance in Ar at intensities on the order of $10^{13}$ W/cm$^2$ [118], the required photon energy and intensity is now available at seeded FELs. This was pointed out recently by Mouloudakis and Lambropoulos in Ref. [62], who instead considered the $2s2p$ doubly excited state of He. They also provide an observable that could be used to study exceptional points. It will therefore be interesting to see if exceptional points in autoionization can be observed with FEL sources.

As was discussed in paper v and explored further in Sec. 8, not including the Coulomb interaction in the propagation after the tunneling step is a major drawback of the SFA-FTI model. Therefore, models that also include the Coulomb interaction, such as the ones proposed by Hu et al. and Bengs et al. in Refs. [95] and [98] seem more promising in this regard. Understanding the FTI process is interesting for instance due to its relation to the acceleration of neutral excited atoms [88].

# Appendices

# 1 Reducing Beers and Armstrongs two-level + continuum model to an effective two-level system

Beers and Armstrong start with an effective three-level system consisting of the resonant bound states $|a\rangle = |\phi_a, N\rangle, |b\rangle = |\phi_b, N-1\rangle$ and a continuum $|\epsilon\rangle = |\phi_\epsilon, N-2\rangle$ where continuum–continuum transitions are neglected [11]. Yet their final expressions for the resolvent matrix elements for $a, b$ (and hence the resulting state amplitudes and probabilities) are equivalent to those of an effective two-level system. This appendix shows the connection between the two physical pictures.

## 1.1 Resolvent equations

The resolvent equations become (neglecting c-c transitions):

$$(z - E_a)G_{aa}(z) - \frac{\Omega}{2}G_{ba}(z) - \int \mathrm{d}\epsilon V_{a\epsilon}G_{\epsilon a}(z) = 1, \tag{140a}$$

$$(z - E_b)G_{ba}(z) - \frac{\Omega}{2}G_{aa}(z) - \int \mathrm{d}\epsilon V_{b\epsilon}G_{\epsilon a}(z) = 0, \tag{140b}$$

$$(z - E_\epsilon)G_{\epsilon a}(z) - V_{a\epsilon}G_{aa}(z) - V_{b\epsilon}G_{ba}(z) = 0, \tag{140c}$$

where $V_{b\epsilon} = \frac{E_0}{2}\langle\epsilon|\, z\, |b\rangle$ and $V_{a\epsilon} = \frac{E_0^2}{2^2}\sum_{c\neq b}\frac{\langle\epsilon|z|c\rangle\langle c|z|a\rangle}{E_a - E_c}$ are the couplings between the bound states and the continuum to second order.

## 1.2 Removing the continuum

In the last equation we can solve for $G_{\epsilon a}(z)$ to get

$$G_{\epsilon a}(z) = \frac{V_{a\epsilon}G_{aa}(z) + V_{b\epsilon}G_{ba}(z)}{z - E_\epsilon}, \tag{141}$$

which can be plugged into the other two equations so that we end up with

$$(z - E_a)G_{aa}(z) - \frac{\Omega}{2}G_{ba}(z) - \int \mathrm{d}\epsilon \frac{|V_{a\epsilon}|^2 G_{aa}(z) + V_{a\epsilon}V_{b\epsilon}G_{ba}(z)}{z - E_\epsilon} = 1, \tag{142a}$$

$$(z - E_b)G_{ba}(z) - \frac{\Omega}{2}G_{aa}(z) - \int \mathrm{d}\epsilon \frac{V_{b\epsilon}V_{a\epsilon}G_{aa}(z) + |V_{b\epsilon}|^2 G_{ba}(z)}{z - E_\epsilon} = 0. \tag{142b}$$

The integrals are evaluated using the resonance condition giving us

$$\lim_{\eta\to 0^+}\int \mathrm{d}\epsilon \frac{|V_{a\epsilon}|^2 G_{aa}(z)+V_{a\epsilon}V_{b\epsilon}G_{ba}(z)}{E+i\eta-E_\epsilon} = \\ \mathrm{p.v.}\int \mathrm{d}\epsilon \frac{|V_{a\epsilon}|^2 G_{aa}(z)+V_{a\epsilon}V_{b\epsilon}G_{ba}(z)}{E-E_\epsilon} - i\pi\left\{|V_{a\epsilon}|^2 G_{aa}(z)+V_{a\epsilon}V_{b\epsilon}G_{ba}(z)\right\} \tag{143}$$

and

$$\lim_{\eta\to 0^+}\int \mathrm{d}\epsilon \frac{|V_{b\epsilon}|^2 G_{ba}(z)+V_{b\epsilon}V_{a\epsilon}G_{aa}(z)}{E+i\eta-E_\epsilon} = \\ \mathrm{p.v.}\int \mathrm{d}\epsilon \frac{|V_{b\epsilon}|^2 G_{ba}(z)+V_{b\epsilon}V_{a\epsilon}G_{aa}(z)}{E-E_\epsilon} - i\pi\left\{|V_{b\epsilon}|^2 G_{ba}(z)+V_{b\epsilon}V_{a\epsilon}G_{aa}(z)\right\}. \tag{144}$$

The first term in the PV integral gives us an energy shift $\Delta E_{a,b}$ and the second one gives a correction to the Rabi frequency $\Omega \to \Omega'$. The first term in the imaginary part gives $\gamma_{a,b}/2$ and the second one gives $\sqrt{\gamma_a\gamma_b}/2 = -\beta/2$ (modulo a sign which is neglected here, but it will determine which dressed state can be stabilized, see Appendix B of paper III).

### 1.3 Putting things together

If we plug the result of evaluating the integrals back into our resolvent equations and group $G_{aa}$ and $G_{ba}$ terms we end up with

$$(z-E_a-\Delta E_a+i\frac{\gamma_a}{2})G_{aa}(z)-\frac{1}{2}\left[\Omega'+i\beta\right]G_{ba}(z)=1, \tag{145a}$$

$$(z-E_b-\Delta E_b+i\frac{\gamma_b}{2})G_{ba}(z)-\frac{1}{2}\left[\Omega'+i\beta\right]G_{aa}(z)=0, \tag{145b}$$

which can be straight forwardly solved to give Eqs. (3) and (11) of Ref. [11]. These equations are precisely what one would get by starting with the effective Hamiltonian

$$H_{\text{eff}} = \begin{bmatrix} E_a+\Delta E_a-i\frac{\gamma_a}{2} & \frac{1}{2}\left[\Omega'+i\beta\right] \\ \frac{1}{2}\left[\Omega'+i\beta\right] & E_b+\Delta E_b-i\frac{\gamma_b}{2}\end{bmatrix} \tag{146}$$

which means that in the end their state amplitudes will be those of an effective two-level system for the $a, b$ levels. This shows that Eq. (19) of paper III will indeed correspond to Eq. (13) of Ref. [11].

With the expression for $G_{\epsilon a}(z)$

$$G_{\epsilon a}(z)=\frac{V_{\epsilon a}G_{aa}(z)+V_{\epsilon b}G_{ba}(z)}{z-E_\epsilon}, \tag{147}$$

with $G_{aa}$ and $G_{ba}$ from the above equations corresponds to the second order version of (118) when selection rules have been used to eliminate $a(b)$ from the first (second) term in that equation.

# References


[1] W. Ackermann et al., "Operation of a free-electron laser from the extreme ultraviolet to the water window", Nature Photon **1**, 336 (2007).

[2] E. Allaria et al., "Highly coherent and stable pulses from the FERMI seeded free-electron laser in the extreme ultraviolet", Nature Photon **6**, 699 (2012).

[3] T. Ishikawa et al., "A compact x-ray free-electron laser emitting in the sub-ångström region", Nature Photon **6**, 540 (2012).

[4] Z. Zhao et al., "SXFEL: a Soft x-ray Free Electron Laser in China", Synchrotron Radiation News **30**, 29 (2017).

[5] N. Huang et al., "Features and futures of x-ray free-electron lasers", The Innovation **2**, 100097 (2021).

[6] P. K. Maroju et al., "Attosecond pulse shaping using a seeded free-electron laser", Nature **578**, 386 (2020).

[7] P. K. Maroju et al., "Attosecond coherent control of electronic wave packets in two-colour photoionization using a novel timing tool for seeded free-electron laser", Nat. Photon. **17**, 200 (2023).

[8] J. Duris et al., "Tunable isolated attosecond x-ray pulses with gigawatt peak power from a free-electron laser", Nat. Photonics **14**, 30 (2020).

[9] S. Li et al., "Attosecond coherent electron motion in Auger-Meitner decay", Science **375**, 285 (2022).

[10] F. Richter et al., "Strong-field quantum control by pulse shaping in the extreme ultraviolet domain", (2024) arXiv:2403.01835 [physics.atom-ph].

[11] B. L. Beers and L. Armstrong, "Exact solution of a realistic model for two-photon ionization", Phys. Rev. A **12**, 2447 (1975).

[12] P. L. Knight, "Saturation and Rabi oscillations in resonant multiphoton ionization", Optics Communications **22**, 173 (1977).

[13] C. R. Holt, M. G. Raymer, and W. P. Reinhardt, "Time dependences of two-, three-, and four-photon ionization of atomic hydrogen in the ground $1^2S$ and metastable $2^2S$ states", Phys. Rev. A **27**, 2971 (1983).

[14] D. Roguś and M. Lewenstein, "Resonant ionisation by smooth laser pulses", J. Phys. B: Atom. Mol. Phys. **19**, 3051 (1986).

[15] U. Saalmann, S. K. Giri, and J. M. Rost, "Adiabatic Passage to the Continuum: Controlling Ionization with Chirped Laser Pulses", Phys. Rev. Lett. **121**, 153203 (2018).

[16] X. Zhang et al., "Effect of nonresonant states in near-resonant two-photon ionization of hydrogen", Phys. Rev. A **106**, 063114 (2022).

[17] A. Bunjac, D. B. Popović, and N. S. Simonović, "Analysis of the asymmetry of Autler–Townes doublets in the energy spectra of photoelectrons produced at two-photon ionization of atoms by strong laser pulses", Eur. Phys. J. D **76**, 249 (2022).

[18] N. S. Simonović, D. B. Popović, and A. Bunjac, "Manifestations of Rabi Dynamics in the Photoelectron Energy Spectra at Resonant Two-Photon Ionization of Atom by Intense Short Laser Pulses", Atoms **11**, 20 (2023).

[19] M. Ferray et al., "Multiple-harmonic conversion of 1064 nm radiation in rare gases", J. Phys. B: At. Mol. Opt. Phys. **21**, L31 (1988).

[20] The Royal Swedish Academy of Sciences, "Press release", (2023) `https://www.nobelprize.org/prizes/physics/2023/press-release/`.

[21] J. L. Krause, K. J. Schafer, and K. C. Kulander, "High-order harmonic generation from atoms and ions in the high intensity regime", Phys. Rev. Lett. **68**, 3535 (1992).

[22] P. Agostini et al., "Free-Free Transitions Following Six-Photon Ionization of Xenon Atoms", Phys. Rev. Lett. **42**, 1127 (1979).

[23] G. G. Paulus et al., "Plateau in above threshold ionization spectra", Phys. Rev. Lett. **72**, 2851 (1994).

[24] M. Lewenstein et al., "Rings in above-threshold ionization: a quasiclassical analysis", Phys. Rev. A **51**, 1495 (1995).

[25] A. L'Huillier et al., "High-order Harmonic-generation cutoff", Phys. Rev. A **48**, R3433 (1993).

[26] M. Lewenstein et al., "Theory of high-harmonic generation by low-frequency laser fields", Phys. Rev. A **49**, 2117 (1994).

[27] S. V. Popruzhenko, "Quantum theory of strong-field frustrated tunneling", J. Phys. B: At. Mol. Opt. Phys. **51**, 014002 (2017).

[28] T. Nubbemeyer et al., "Strong-Field Tunneling without Ionization", Phys. Rev. Lett. **101**, 233001 (2008).

[29] V. Véniard, R. Taïeb, and A. Maquet, "Phase dependence of (n+1)-color (n>1) ir-uv photoionization of atoms with higher harmonics", Phys. Rev. A **54**, 721 (1996).

[30] P. M. Paul et al., "Observation of a Train of Attosecond Pulses from High Harmonic Generation", Science **292**, 1689 (2001).

[31] H. Muller, "Reconstruction of attosecond harmonic beating by interference of two-photon transitions", Appl Phys B **74**, s17 (2002).

[32] J. M. Dahlström et al., "Theory of attosecond delays in laser-assisted photoionization", Chemical Physics, Attosecond spectroscopy **414**, 53 (2013).

[33] J. J. Sakurai and J. Napolitano, *Modern Quantum Mechanics*, 2nd ed. (Cambridge University Press, 2017).

[34] D. H. Kobe and A. L. Smirl, "Gauge invariant formulation of the interaction of electromagnetic radiation and matter", American Journal of Physics **46**, 624 (1978).

[35] D. H. Kobe, "Gauge-invariant resolution of the controversy over length versus velocity forms of the interaction with electric dipole radiation", Phys. Rev. A **19**, Publisher: American Physical Society, 205 (1979).

[36] M. Bertolino et al., "Thomas–Reiche–Kuhn correction for truncated configuration-interaction spaces: Case of laser-assisted dynamical interference", Phys. Rev. A **106**, 043108 (2022).

[37] I. Lindgren and J. Morrison, *Atomic Many-Body Theory*, Second edition, Springer Series on Atomic, Optical, and Plasma Physics (Springer Berlin, Heidelberg, 1986).

[38] N. Rohringer, A. Gordon, and R. Santra, "Configuration-interaction-based time-dependent orbital approach for ab initio treatment of electronic dynamics in a strong optical laser field", Phys. Rev. A **74**, 043420 (2006).

[39] L. Greenman et al., "Implementation of the time-dependent configuration-interaction singles method for atomic strong-field processes", Phys. Rev. A **82**, 023406 (2010).

[40] S. Carlström, M. Spanner, and S. Patchkovskii, "General time-dependent configuration-interaction singles. i. Molecular case", Phys. Rev. A **106**, 043104 (2022).

[41] S. Carlström et al., "General time-dependent configuration-interaction singles. II. Atomic case", Phys. Rev. A **106**, 042806 (2022).

[42] A. Maquet, S.-I. Chu, and W. P. Reinhardt, "Stark ionization in dc and ac fields: An $L^2$ complex-coordinate approach", Phys. Rev. A **27**, 2946 (1983).

[43] S.-I. Chu and D. A. Telnov, "Beyond the Floquet theorem: generalized Floquet formalisms and quasienergy methods for atomic and molecular multiphoton processes in intense laser fields", Physics Reports **390**, 1 (2004).

[44] F. H. M. Faisal, *Theory of Multiphoton Processes* (Springer New York, NY, 1987).

[45] C. Cohen-Tannoudji, J. Dupont-Roc, and G. Grynberg, "The dressed atom approach", in *Atom—photon interactions* (John Wiley & Sons, Ltd, 1998) Chap. 6, pp. 407–514.

[46] K. J. LaGattuta, "Above-threshold ionization of atomic hydrogen via resonant intermediate states", Phys. Rev. A **47**, 1560 (1993).

[47] M. G. Girju et al., "Nonperturbative resonant strong field ionization of atomic hydrogen", Journal of Physics B: Atomic, Molecular and Optical Physics **40**, 4165 (2007).

[48] Z. Sun and N. Lou, "Autler-Townes Splitting in the Multiphoton Resonance Ionization Spectrum of Molecules Produced by Ultrashort Laser Pulses", Phys. Rev. Lett. **91**, 023002 (2003).

[49] A. Palacios, H. Bachau, and F. Martín, "Step-ladder Rabi oscillations in molecules exposed to intense ultrashort vuv pulses", Phys. Rev. A **74**, 031402 (2006).

[50] S.-I. Chu, "Quasienergy formalism for intense field multiphoton ionization of atoms induced by circularly polarized radiation", Chemical Physics Letters **54**, 367 (1978).

[51] I. I. Rabi, "Space quantization in a gyrating magnetic field", Phys. Rev. **51**, 652 (1937).

[52] S. H. Autler and C. H. Townes, "Stark effect in rapidly varying fields", Phys. Rev. **100**, 703 (1955).

[53] C. J. Foot, *Atomic physics* (Oxford University Press, Oxford, 2005).

[54] K. A. Fischer et al., "Pulsed Rabi oscillations in quantum two-level systems: beyond the area theorem", Quantum Sci. Technol. **3**, 014006 (2017).

[55] Y. Liao et al., "Reconstruction of attosecond beating by interference of two-photon transitions on the lithium atom with Rabi oscillations", Phys. Rev. A **105**, 063110 (2022).

[56] R. Grobe and J. H. Eberly, "Observation of coherence transfer by electron-electron correlation", Phys. Rev. A **48**, 623 (1993).

[57] B. Walker et al., "Observation of Continuum-Continuum Autler-Townes Splitting", Phys. Rev. Lett. **75**, 633 (1995).

[58] D. Younis and J. H. Eberly, "Benchmark of few-level quantum theory vs ab initio numerical solutions for the strong-field Autler–Townes effect in photoionization of hydrogen", J. Phys. B: At. Mol. Opt. Phys. **55**, 164001 (2022).

[59] M. Wollenhaupt et al., "Control of interferences in an Autler-Townes doublet: Symmetry of control parameters", Phys. Rev. A **68**, 015401 (2003).

[60] C. Cohen-Tannoudji, J. Dupont-Roc, and G. Grynberg, "Nonperturbative calculation of transition amplitudes", in *Atom—photon interactions* (John Wiley & Sons, Ltd, 1998) Chap. 3, pp. 165–255.

[61] D. Finkelstein-Shapiro and A. Keller, "Ubiquity of Beutler-Fano profiles: From scattering to dissipative processes", Phys. Rev. A **97**, 023411 (2018).

[62] G. Mouloudakis and P. Lambropoulos, "Non-Hermitian landscape of autoionization", Phys. Rev. A **108**, 063104 (2023).

[63] P. Lambropoulos and P. Zoller, "Autoionizing states in strong laser fields", Phys. Rev. A **24**, 379 (1981).

[64] E. Brion, L. H. Pedersen, and K. Mølmer, "Adiabatic elimination in a lambda system", J. Phys. A: Math. Theor. **40**, 1033 (2007).

[65] M. L. Goldberger and K. M. Watson, *Collision theory*, Structure of matter series (Wiley, New York, 1964).

[66] B. Simon, "The definition of molecular resonance curves by the method of exterior complex scaling", Physics Letters A **71**, 211 (1979).

[67] N. Moiseyev, "Quantum theory of resonances: calculating energies, widths and cross-sections by complex scaling", Physics Reports **302**, 212 (1998).

[68] R. M. Potvliege, "STRFLO: a program for time-independent calculations of multiphoton processes in one-electron atomic systems I. Quasienergy spectra and angular distributions", Computer Physics Communications **114**, 42 (1998).

[69] C. W. McCurdy, C. K. Stroud, and M. K. Wisinski, "Solving the time-dependent Schrödinger equation using complex-coordinate contours", Phys. Rev. A **43**, 5980 (1991).

[70] A. Scrinzi, "Infinite-range exterior complex scaling as a perfect absorber in time-dependent problems", Phys. Rev. A **81**, 053845 (2010).

[71] C. W. McCurdy and F. Martín, "Implementation of exterior complex scaling in b-splines to solve atomic and molecular collision problems", J. Phys. B: At. Mol. Opt. Phys. **37**, 917 (2004).

[72] R. Kosloff and D. Kosloff, "Absorbing boundaries for wave propagation problems", Journal of Computational Physics **63**, 363 (1986).

[73] U. V. Riss and H.-D. Meyer, "Calculation of resonance energies and widths using the complex absorbing potential method", J. Phys. B: At. Mol. Opt. Phys. **26**, 4503 (1993).

[74] R. Lefebvre, M. Sindelka, and N. Moiseyev, "Resonance positions and lifetimes for flexible complex absorbing potentials", Phys. Rev. A **72**, 052704 (2005).

[75] R. Santra, "Why complex absorbing potentials work: a discrete-variable-representation perspective", Phys. Rev. A **74**, 034701 (2006).

[76] E. Cormier and P. Lambropoulos, "Extrapolation method for the evaluation of above threshold ionization cross sections for one- and two-electron systems", J. Phys. B: At. Mol. Opt. Phys. **28**, 5043 (1995).

[77] Y. Nakatsukasa, O. Sète, and L. N. Trefethen, "The AAA Algorithm for Rational Approximation", SIAM J. Sci. Comput. **40**, A1494 (2018).

[78] G. A. Baker and P. Graves-Morris, *Padé Approximants*, 2nd ed., Encyclopedia of Mathematics and its Applications (Cambridge University Press, 1996).

[79] J. Benda and Z. Mašín, "Multi-photon above threshold ionization of multi-electron atoms and molecules using the r-matrix approach", Sci Rep **11**, 11686 (2021).

[80] Y. Saad and M. H. Schultz, "GMRES: a Generalized Minimal Residual Algorithm for Solving Nonsymmetric Linear Systems", SIAM Journal on Scientific and Statistical Computing **7**, 856 (1986).

[81] P. N. Brown and H. F. Walker, "GMRES On (Nearly) Singular Systems", SIAM J. Matrix Anal. Appl. **18**, 37 (1997).

[82] A. Ben-Israel and T. N. E. Greville, *Generalized Inverses*, 2nd ed. (Springer New York, NY, 2003).

[83] P. B. Corkum, "Plasma perspective on strong field multiphoton ionization", Phys. Rev. Lett. **71**, 1994 (1993).

[84] N. Bleistein and R. A. Handelsman, *Asymptotic expansions of integrals* (Dover, New York, 1986).

[85] H. Zimmermann et al., "Strong-Field Excitation of Helium: Bound State Distribution and Spin Effects", Phys. Rev. Lett. **114**, 123003 (2015).

[86] G. L. Yudin and M. Y. Ivanov, "Physics of correlated double ionization of atoms in intense laser fields: Quasistatic tunneling limit", Phys. Rev. A **63**, 033404 (2001).

[87] N. I. Shvetsov-Shilovski et al., "Capture into rydberg states and momentum distributions of ionized electrons", Laser Phys. **19**, 1550 (2009).

[88] S. Eilzer and U. Eichmann, "Steering neutral atoms in strong laser fields", J. Phys. B: At. Mol. Opt. Phys. **47**, 204014 (2014).

[89] U. Eichmann, in *Ultrafast Dynamics Driven by Intense Light Pulses: From Atoms to Solids, from Lasers to Intense x-rays*, edited by M. Kitzler and S. Gräfe, Springer Series on Atomic, Optical, and Plasma Physics (Springer International Publishing, Cham, 2016), pp. 3–25.

[90] J. Dubois et al., "Capturing Photoelectron Motion with Guiding Centers", Phys. Rev. Lett. **121**, 113202 (2018).

[91] J. Dubois et al., "Guiding-center motion for electrons in strong laser fields", Phys. Rev. E **98**, 052219 (2018).

[92] J. Dubois et al., "Inclusion of Coulomb effects in laser-atom interactions", Phys. Rev. A **99**, 053405 (2019).

[93] B. Piraux et al., "Excitation of Rydberg wave packets in the tunneling regime", Phys. Rev. A **96**, 043403 (2017).

[94] H. Zimmermann et al., "Unified Time and Frequency Picture of Ultrafast Atomic Excitation in Strong Laser Fields", Phys. Rev. Lett. **118**, 013003 (2017).

[95] S. Hu et al., "Quantum dynamics of atomic Rydberg excitation in strong laser fields", Opt. Express, OE **27**, 31629 (2019).

[96] B. Piraux et al., "Iterative treatment of the Coulomb potential in laser–atom interactions", Eur. Phys. J. D **75**, 196 (2021).

[97] F. H. M. Faisal, "Gauge-invariant intense-field approximations to all orders", J. Phys. B: At. Mol. Opt. Phys. **40**, F145 (2007).

[98] U. Bengs et al., "All-optical Stückelberg spectroscopy of strongly driven Rydberg states", Phys. Rev. Res. **4**, 023135 (2022).

[99] M. Gavrila, "Atomic stabilization in superintense laser fields", en, J. Phys. B: At. Mol. Opt. Phys. **35**, R147 (2002).

[100] U. Eichmann and S. Patchkovskii, in *Advances In Atomic, Molecular, and Optical Physics*, Vol. 72, edited by L. F. DiMauro, H. Perrin, and S. F. Yelin, Advances in Atomic, Molecular, and Optical Physics (Academic Press, Jan. 2023), pp. 1–88.

[101] L. Tao and A. Scrinzi, "Photo-electron momentum spectra from minimal volumes: the time-dependent surface flux method", New J. Phys. **14**, 013021 (2012).

[102] F. Morales, T. Bredtmann, and S. Patchkovskii, "iSURF: a family of infinite-time surface flux methods", J. Phys. B: At. Mol. Opt. Phys. **49**, 245001 (2016).

[103] M. Bertolino, "Applications of time-dependent configuration-interaction singles for photoelectrons in attosecond and free-electron laser sciences", Doctoral Thesis (2023).

[104] E. Kyrölä, "N levels and the continuum", J. Phys. B: Atom. Mol. Phys. **19**, 1437 (1986).

[105] T. Kato, "Pertrubation theory in a finite-dimensional space", in *Perturbation theory for linear operators* (Springer Berlin, Heidelberg, 1995) Chap. 2, pp. 62–126.

[106] W. D. Heiss, "The physics of exceptional points", J. Phys. A: Math. Theor. **45**, 444016 (2012).

[107] N. Mayer, N. Moiseyev, and O. Smirnova, "Enantiosensitive exceptional points", (2023) arXiv:2306.12293 [quant-ph].

[108] M. Pont and R. Shakeshaft, "Analytic structure of the ac quasienergy in the complex-field plane", Phys. Rev. A **43**, 3764 (1991).

[109] E. S. Toma and H. G. Muller, "Calculation of matrix elements for mixed extreme-ultraviolet–infrared two-photon above-threshold ionization of argon", J. Phys. B: At. Mol. Opt. Phys. **35**, 3435 (2002).

[110] A. S. Kheifets, "Strongly resonant reconstruction of attosecond beating by interference of two-photon transitions on lithium", Phys. Rev. A **104**, L021103 (2021).

[111] A. Sarsa, F. J. Gálvez, and E. Buendía, "Parameterized optimized effective potential for the ground state of the atoms He through Xe", Atomic Data and Nuclear Data Tables **88**, 163 (2004).

[112] B. Gao and A. F. Starace, "Numerical methods for free-free radiative transition matrix elements", Computers in Physics **1**, 70 (1987).

[113] E. Pisanty, M. F. Ciappina, and M. Lewenstein, "The imaginary part of the high-harmonic cutoff", J. Phys. Photonics **2**, 034013 (2020).

[114] Y. Zhao et al., "Frustrated tunneling ionization in the elliptically polarized strong laser fields", Opt. Express **27**, 21689 (2019).

[115] Y.-J. Mao et al., "Unveiling Rabi dynamics through angle-resolved photoelectron momentum distributions using an $\omega - 2\omega$ pulse pair", Phys. Rev. A **108**, 053117 (2023).

[116] X. Zhang et al., "Characterization of the two-photon transition phase in the buildup process of Rabi oscillations", Phys. Rev. A **109**, 033101 (2024).

[117] T. Bayer et al., "Bichromatic phase control of interfering Autler-Townes spectra", Phys. Rev. A **109**, 033111 (2024).

[118] O. Latinne et al., "Laser-Induced Degeneracies Involving Autoionizing States in Complex Atoms", Phys. Rev. Lett. **74**, 46 (1995).

# Scientific publications

## Author contributions

Co-authors are indicated by their initials

### Paper I: Observation of Rabi dynamics with a short-wavelength free-electron laser

I developed the theoretical model, following suggestions from JMD, and I contributed to the interpretation of the experiment. I calculated the atomic parameters that are required for the model and generated the model data for Figs. 1 (b,c), 2 (c,d), 3 (b,c,d), and 4 (d) of the main text, as well as Extended Data Fig. 6 and Extended Data Table 1. I wrote the Supplementary Information with comments from JMD. I contributed with comments and proofreading of the main manuscript. I actively participated in the process of replying to the referee comments, and I did the ionization probability estimates and produced Fig. R1 that were included in the reply.

### Paper II: Generation of entanglement using a short-wavelength seeded free-electron laser

I generated the data for Fig. 1 (b), which displays the available parameter space for generation of entanglement. I estimated the ac Stark shifts and ionization lifetimes of neutral He and $He^+$. I contributed with comments and proofreading of the main manuscript and supplemental information.

### Paper III: Photoelectron signature of dressed atom stabilization in an intense XUV-field

I performed a literature review on the topic of resonant photoionization in strong fields, and I used the effective Hamiltonian method to predict stabilization for He interacting with circularly polarized FEL pulses. I generated the data for all plots and tables, and made all the figures. I wrote the manuscript together with JMD, and I handled the communication with the editors.

### Paper IV: Circularly polarized RABBIT applied to a Rabi-cycling atom

I calculated matrix elements for ATI and resonant ionization processes, with a complementary method (based on extrapolation), that were used to benchmark the perturbative calculations of YL. I contributed with comments and proofreading of the manuscript.

### Paper V: Frustrated tunneling dynamics in ultra-short laser pulses

I implemented the model of Popruzhenko, and extended it to include the laser envelope and the factor from projection onto Rydberg states. I performed extensive model calculations, that were compared quantitatively with TDSE simulations. I produced all figures included in the manuscript, and I wrote the manuscript with input from SC and JMD.

Printed by Media-Tryck, Lund 2024 NORDIC SWAN ECOLABEL 3041 0903

LUND UNIVERSITY

Faculty of Engineering
Department of Physics

ISBN 978-91-8104-058-6